Characterization and validation of postnatal murine precision cut lung slices using different approaches of stereology

Inaugural Dissertation submitted to the Faculty of Medicine

in partial fulfillment of the requirements

for the PhD-Degree

of the Faculties of Veterinary Medicine and Medicine of the Justus Liebig University

Giessen

By

Pérez Bravo, David,

Giessen (2022)

From the Max Planck Institute for Heart and Lung Research

Director: Prof. Dr. Werner Seeger

of the Faculty of Medicine of the Justus Liebig University Giessen

First Supervisor and Committee Member: Prof. Dr. Werner Seeger

Second Supervisor: Prof. Dr. Reinhard Dammann

Committee member (Chairman): Prof. Dr. Klaus-Dieter Schlüter

Committee member (Vice-Chairman): Prof. Dr. Peter König

Date of doctoral defense: 07.09.2022

Table of content

1. Introduction 5
   - *1.1. Gross anatomy of murine and human lung 5*
   - *1.2. Fetal and postnatal lung development 7*
   - *1.3. Alveolarization 8*
   - *1.4. Cellular basis of murine lung development 9*
   - *1.5. Using Stereology to quantify structural changes in lung development 13*
   - *1.6. Studing in vitro alveolarization 15*
   - *1.7. Precision-cut Lung Slices as model of alveolarization 15*
2. Hypothesis 17
3. Materials 18
   - *3.1. Equipment 18*
   - *3.2. Reagents and drugs 20*
   - *3.3. Primers for genotyping and qPCR 22*
   - *3.4. Consumables 23*
   - *3.5. Software 24*
4. Methods 25
   - *4.1. Experimental mice 25*
   - *4.2. Wild-type mice 25*
   - *4.3. Transgenic mice 25*
   - *4.4. Tissue processing 27*
   - *4.5. Staining of lung tissue for stereological analysis 30*
   - *4.6. Gene expression analysis 32*
   - *4.7. Imunostaining in histological sections 33*
   - *4.8. Image processing, analysis and figure preparation 33*
   - *4.9. Statistics 34*
5. Results 35
   - *5.1. Establishment of two different in vitro tissue system: entire lung versus PCLS 35*
   - *5.2. Assessment of short-term cultivated murine PCLS 37*
   - *5.3. In vitro PCLS stereological quantification 39*
   - *5.4. Quantification of gene expression in postnatal PCLS 48*
   - *5.5. Visualization of overexpressed marker by confocal imaging 50*
6. Discussion 52
7. Conclusion 59
8. References 60
9. List of abbreviations 76
10. List of figures 77

11. List of tables....78
12. Summary....79
13. Zusammenfassung....80
14. Appendix....81
15. Declaration....88
16. Acknowledgement....89
17. Curriculum vitae....90

1. Introduction

1.1. Gross anatomy of murine and human lung

Lungs are the principal organs composing the respiratory system in mammals. Their main function is to extract atmospheric oxygen and transfer it into the bloodstream. Simultaneously, a release of carbon dioxide also occurs. The respiratory process is driven by the thoracic musculature in mammals (Richard L. Drake et al., 2014). The mammalian lung can be divided into two structural components: the conducting tract or airway, which transports air from outside of the body to the gas-exchange side; and the respiratory zone, where the exchange of oxygen and carbon dioxide occurs (Kotton & Morrisey, 2014).

The airway consists of a principal tube which splits into smaller branches that then divide into several ramifications. Each division point where one airway branches into smaller airways is known as a generation. Despite the many similarities, there are some important differences in gross lung anatomy among mammals (Suarez et al., 2012) which need to be taken into account for comparative studies. Mice, the most common model to study lung development (Rydell-Törmänen & Johnson, 2018), also differ somewhat from humans in this regard. For instance, the human respiratory tree consists on average of 23 generations, while the mouse respiratory tree only has up to 13 generations (Irvin & Bates, 2003; Suarez et al., 2012). The main tube, the trachea, is a cartilaginous conduct that connects the larynx to the bronchi. This structure is composed is made up of a number of vertically arranged and continuously open horseshoe-shaped rings. The trachea bifurcates into two primary bronchi at the carina, each one of which carries air into a lung (Amador et al., 2021; Suarez et al., 2012). Further subsequent splitting first leads to secondary bronchi and then into bronchioles. The bronchioles or bronchioli are smaller branches of the bronchial airways in the respiratory tract, which includes the terminal bronchioles. In human lungs, the left primary bronchus bifurcates into a secondary bronchus and separates into two lobes (upper and lower) at the interlobar fissures, while mice lack a physical separation through fissures, although the bronchus still separates into two secondary bronchi (Suarez et al., 2012). The human right primary bronchus also splits into three right lobes (upper, middle and lower) while the murine homologue bears a fourth bifurcation, the cranial lobe, separated by the interlobal fissure (Suarez et al., 2012).

Bronchioles, unlike bronchi, contain neither cartilage or glands in their submucosa. Cartilage exists only in the trachea and in the proximal segment of the main bronchi. In mice, the bronchiole is the initial anatomic segment of the rodent acinus, making discrimination of small bronchi and bronchioli especially challenging in mouse lung sections (Suarez et al., 2012). In humans, terminal bronchioles end in respiratory bronchioles that give rise to 2–11 alveolar ducts, from which roughly six alveolar sacs

develop. Alveoli line the wall of alveolar sacs and represent the terminal end of the respiratory zone (Figure 1).

The respiratory zone is organized in a tubular-like network that maximizes surface area. Gas exchange takes place across the alveolo-capillary barrier composed of several types of cells interacting with each other, located inside the alveolar unit (Kotton & Morrisey, 2014). This zone of the airways includes the respiratory bronchioles and alveoli (Horsfield et al., 1987). The distal lung parenchyma of the terminal bronchiole is known as the acinus, and it constitutes the functional unit of the lung where gas exchange occurs (Figure 1). The acinus is morphologically composed by the terminal bronchiole, alveolar duct, alveolar sac, and lastly by the alveolus, the terminal portion of the respiratory zone.

Alveoli are hollow cup-shaped cavities, which inflate and retract when breathing and are found in the lung parenchyma where gas exchange takes place. According to Ochs et al, ~480 Million alveoli are present in a human lung, compared to the 2.30 Millions of an adult mouse (Knust et al., 2009; Ochs et al., 2004). Alveoli are characteristically thin-walled, round structures which are surrounded by capillaries, allowing gas exchange. The alveolar surface comprises 82.2 cm^2 in an adult mouse lung (Knust et al., 2009), and 126 m^2 in humans according to (Tomashefski & Farver, 2008).

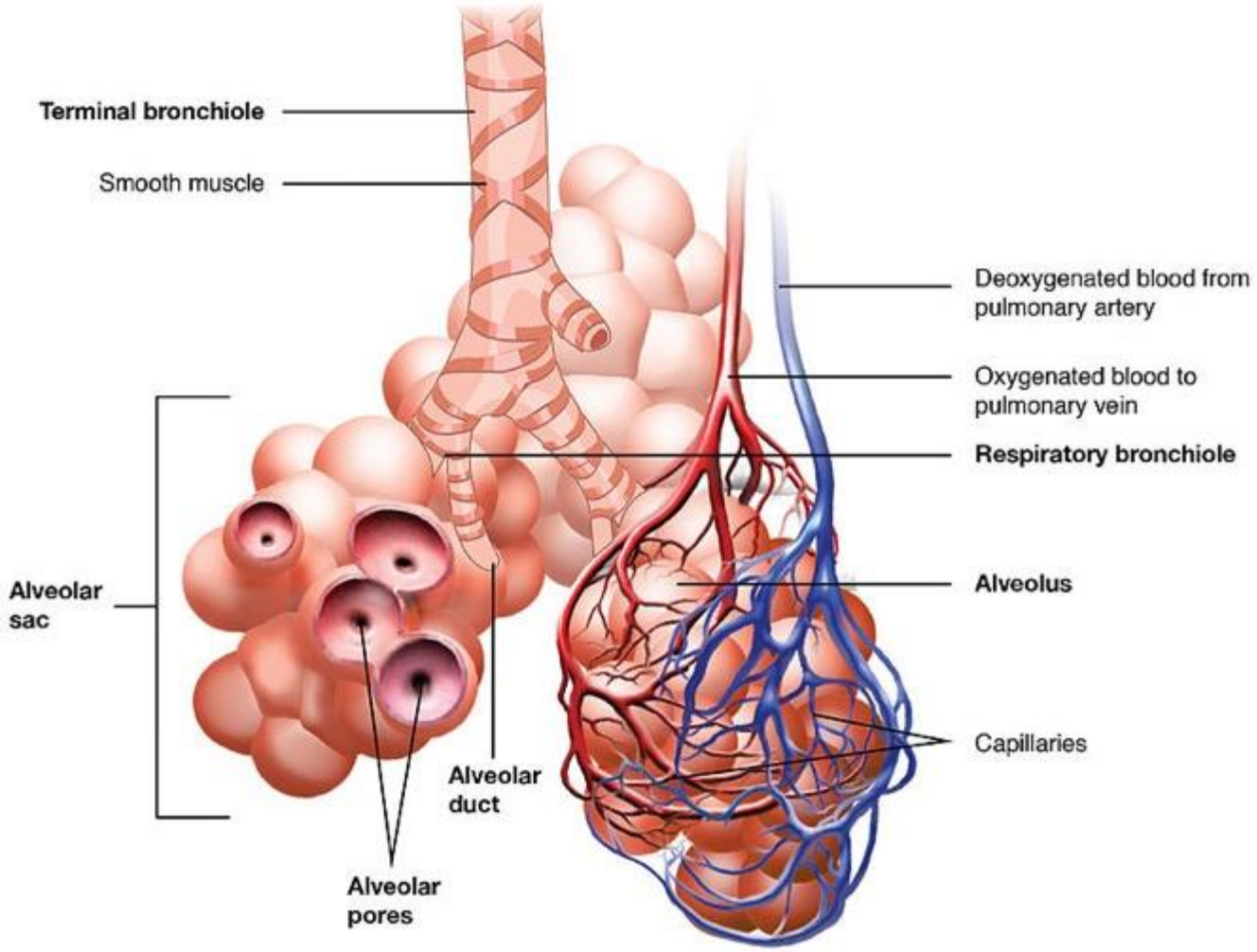

Figure 1. Lower respiratory tract. The lower respiratory tract includes the trachea, bronchi, bronchioles and alveoli. In the lung, each bronchus divides into bronchi and continues to branch into smaller airways (bronchioles). The bronchioles end in the alveoli which form alveolar sacs. Image reproduced from Illustration from Anatomy & Physiology (https://openstax.org/books/anatomy-and-physiology).

Gas exchange occurs within the alveolar walls, where gases diffuse following concentration gradients. The end result of the exchange is oxygen entering the bloodstream and carbon dioxide being released into the alveolar airspace. These gases need to cross the alveolar-capillary membrane, a thin layer of alveolar surfactant (which prevents the alveoli from collapsing) followed by a monolayer of epithelial cells, extracellular matrix and endothelial cells that compose the capillaries. In total, this membrane is ~0.6 μm thick (Hachenberg & Rettig, 1998). In order to increase passive gas-exchange efficiency, bloodstream oxygen concentration should be lower than atmospheric values while the opposite is true for carbon dioxide.

In mammals, the respiratory system is connected to the circulatory system, lending to a division of the latter into systemic and, pulmonary, and connecting the respiratory system to the four-chambered heart. The bloodstream carrying poorly-oxygenated blood enters the right ventricle via the right atrium, where it is pumped into the lungs via the pulmonary artery. This latter artery is divided into small-diameter vessels, reaching up to a capillary surface area of 124 cm^2, and length of 1.13 km in mice (Knust et al., 2009), and 130 cm^2 and 2746 km in humans, respectively (Mühlfeld et al., 2010). The interconnected segments of these capillaries create loops around the connective tissue within the alveolar walls, building up a net that surrounds the alveolar airspaces (Willführ et al., 2015). Once the gas-exchange is performed by passive diffusion at the alveolar-capillary membrane, cardiac beat returns richly oxygenated blood from the pulmonary veins into the left atrium. This blood then passes through the left ventricle and is pumped out into systemic circulation via the aorta−where oxygen is used and metabolized to carbon dioxide (Hall & Hall, 2021).

1.2. Fetal and postnatal lung development

As a highly complex organ, lung development in mammals is a complicated process usually divided into two time-frames: (*i*) early lung development, during the embryonic stage; and (*ii*) late lung development, which occurs postnatally until full lung maturity is reached. The latter is species-dependent as illustrated in Figure 2 (S. Wu & Savani, 2019). In general, lung development can be sequentially described in stages as follows:

- *Embryonic*: Lung buds form from the ventral wall of the foregut resulting in lung lobar division.
- *Pseudoglandular*: Major airway branching and epithelial tubes are formed.
- *Canalicular*: Preparation for alveolarization through formation of bronchioles and increasing the number of capillaries surrounding the cuboidal epithelium.

- *Saccular*: Origination of the alveolar ducts and air sacs.
- *Alveolar*: Alveoli are formed by secondary septation followed by further increase in capillary density. The secondary septum consists of cells growing in crest-like structures from one side of the alveolar primary walls (primary septum) to another, hence closing the alveolar space to form alveolar units. Secondary septation continues even after birth until the lung reaches its full maturity (Burri, 1984; Zeltner & Burri, 1987).

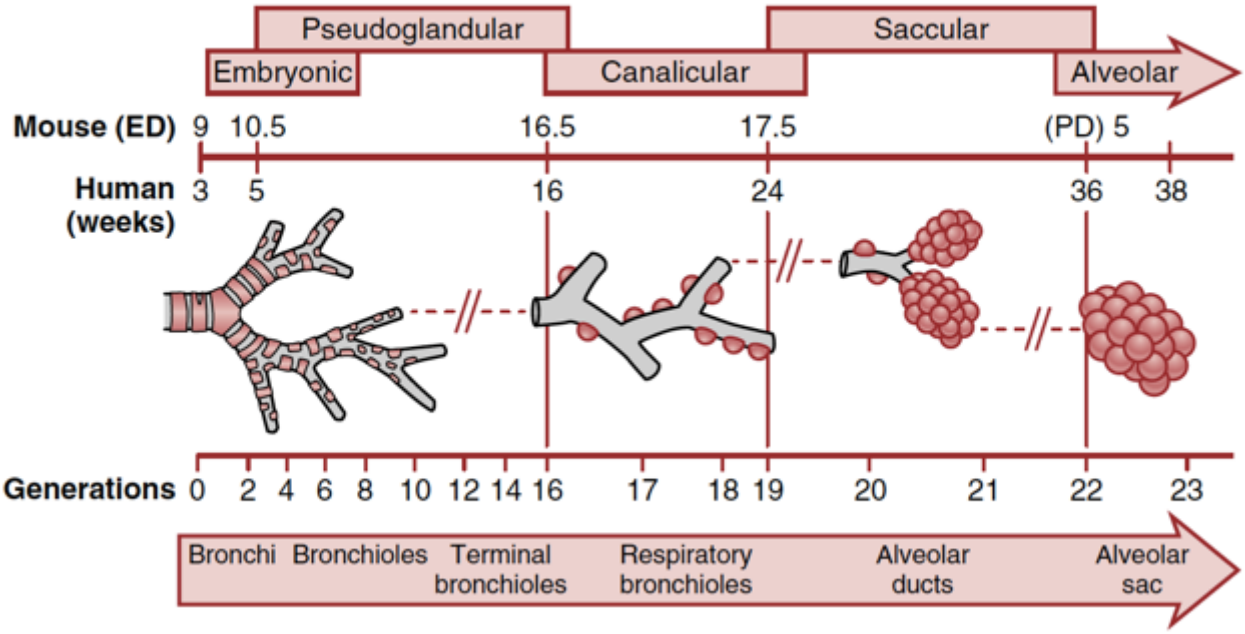

Figure 2. Phases of human and mouse lung development. Human and mouse lung development follow the same phases — namely, embryonic, pseudoglandular, canalicular, saccular, and alveolar. Formation of the human lung bud occurs at 4 weeks of gestation, whereas mouse lung development begins at embryonic day (ED) 9. Trachea and major bronchi are formed by the end of the embryonic stage. The conducting airways are formed during the pseudoglandular stage up to the level of terminal bronchioles. Respiratory bronchioles are formed during the canalicular stage, whereas alveolar ducts are formed during the saccular stage. Alveolarization in humans begins at around 34 weeks and continues at least through the first few years of childhood. Alveolarization in mice begins at postnatal day (PD) 3 and continues for about 4 weeks (S. Wu & Savani, 2019).

1.3. Alveolarization

Alveolization is the process by which alveoli are formed and capillary number increases after the process of secondary septation. Alveolarization starts at the end of the saccular stage, when the lung parenchyma possesses thick, immature septa that contain a double-layered capillary network (Schittny, 2017). During this process, new septa are lifted off from already existing immature septa and divide the existing airspaces. Secondary septa are formed a string of elastic fibers and collagen fibrils laid down by smooth muscle (Burri 1974; Lindahl et al. 1997). The additional surface area of the capillary network is most

likely formed by intussusceptive angiogenesis (Caduff et al. 1986). After the formation of a new septum is initiated, the septum rises up to its full height and the first alveoli are formed. In humans (Herring et al. 2014), rats (Schittny et al. 2008; Tschanz et al. 2014) and mice (Mund et al. 2008), alveolarization is biphasic. Classical alveolarization starts as a quick burst and reduces its speed during the switch to continued alveolarization.

However, as pointed out previously, there are important differences between murine and human lungs, which also pertain development. Mouse models have been used to study he underlying molecular and cellular mechanisms of lung homeostasis and development. However, the use of mice to study lung development assumes the researcher's understanding of explicit functional and physiological differences between the two species (Suarez et al., 2012).

In particular, the process of alveolization in murine lungs begins postnatally from Postnatal day (P) 5 whereas in humans, is happens during gestation, at embryonic week 36, Figure 2 (S. Wu & Savani, 2019). As previously described, alveolarization is the process during lung development that leads to the formation and maturation of the distal parts of the lung: the alveoli. Because of limited and scarce availability of human tissue, mouse models are extensively used to study alveolarization. On birth, the murine lung is still at the saccular stage (Figure 2) (Morrisey & Hogan, 2010), so postnatal mice are often used to model the "equivalent" lung stage in pre-term born infants. These lungs are perfectly competent for effective gas exchange at birth, contrasting with the situation in pre-term born human infants (Rodríguez-Castillo et al., 2018).

On P7, all the septa have adopted a serrated appearance, with a large number of low ridges projecting into the airspaces. These ridges rise from the primary septa and define the so-called 'secondary septa', the contours of the future alveoli. Elastic fibers are typically located at the tip of the crests. The best accepted hypothesis behind this morphology is that the appearance of elastin and of alveolar crests are closely linked, an idea supported by the finding that alveolarization fails to occur in PDGF-A-deficient mice, where elastic fibers are not deposited properly (Lindahl et al., 1997). The sudden and massive appearance of alveoli in the lung parenchyma has been called 'bulk alveolarization'. The alveolarization phase ends at P14 in rodents and at about 12–24 months in humans (Thurlbeck, 1982; Zeltner & Burri, 1987).

1.4. Cellular basis of murine lung development

Up to 41 cell types have been identified in the murine lung (Travaglini et al., 2020). These cells develop during the various embryonic stages, when the endoderm progressively differentiates into specialized cell types, with the ultimate rise of epithelial cells and further differentiated cell lines composing lung tissue. The timing of differentiation of each cell progenitor into a more derived cell is highly dependent

on the cell type. This process is orchestrated by the transcription factor Nkx2-1 gene, which encodes the protein NK2 homeobox 1 (NKX2-1), also known as thyroid transcription factor 1 (TTF-1). This gene is key to fetal development of lung structures, mainly defining the timepoint when trachea and primary lung buds appear (Minoo et al., 1999; Morrisey & Hogan, 2010; Que et al., 2006).

During the pseudoglandular stage, epithelial cells undergo proximal-to-distal differentiation. For example, ciliated and pulmonary neuroendocrine cells are first found in proximal conducting airways and progressively develop in distal airway regions (Rawlins et al., 2007; Sorokin et al., 1997). Initial air-blood barriers are formed during the canalicular phase, when capillaries begin to assemble around airspaces. This process will culminate with the development of the acinar epithelium into the alveolar epithelial type I cells (AECI), and surfactant-producing type II cells (AECII) (Desai et al., 2014; Wongtrakool et al., 2003). Finally, basal and mucous cells emerge during further developmental stages (Rackley & Stripp, 2012).

Lungs are composed of a wide diversity of cells which possess very diverse functions, such as host-pathogen defense, establishment of the air-blood interface and regulation of alveolar surface tension (Li et al., 2018; Travaglini et al., 2020). Cell composition varies among different structural components of the lung. Airways are lined by pseudostratified columnar epithelium comprised of club, ciliated, pulmonary neuroendocrine cells and basal cells, interspersed by submucosal glands underneath the airway epithelium surface (X. Liu & Engelhardt, 2008; Van Lommel, 2001) (Figure 3). Cell composition at the airways mainly serves a protective role: goblet cells, a set of columnar goblet-shaped epithelial cells, secrete mucins in order to protect the mucous membranes; club cells are cells with short microvilli that secrete glycosaminoglycans to protect the bronchiole lining and are responsible for detoxifying harmful substances by cytochrome P450 enzymes located in their smooth endoplasmic reticulum. Club cells also act as stem cells, multiplying and differentiating into ciliated cells to regenerate the bronchiolar epithelium. Following these cell types are airway basal cells, the stem cells of the airway epithelium, which can differentiate to replenish all epithelial cells including ciliated cells, and secretory goblet cells (Atkinson et al., 2008; Rubin, 2014). Again, cell type composition varies between humans and mice. For instance, goblet cells are scare in mice while basal cells numbers are lower at the distal parts of the bronchiolar tree (Hogan et al., 2014; Rackley & Stripp, 2012; Van Lommel et al., 1998).

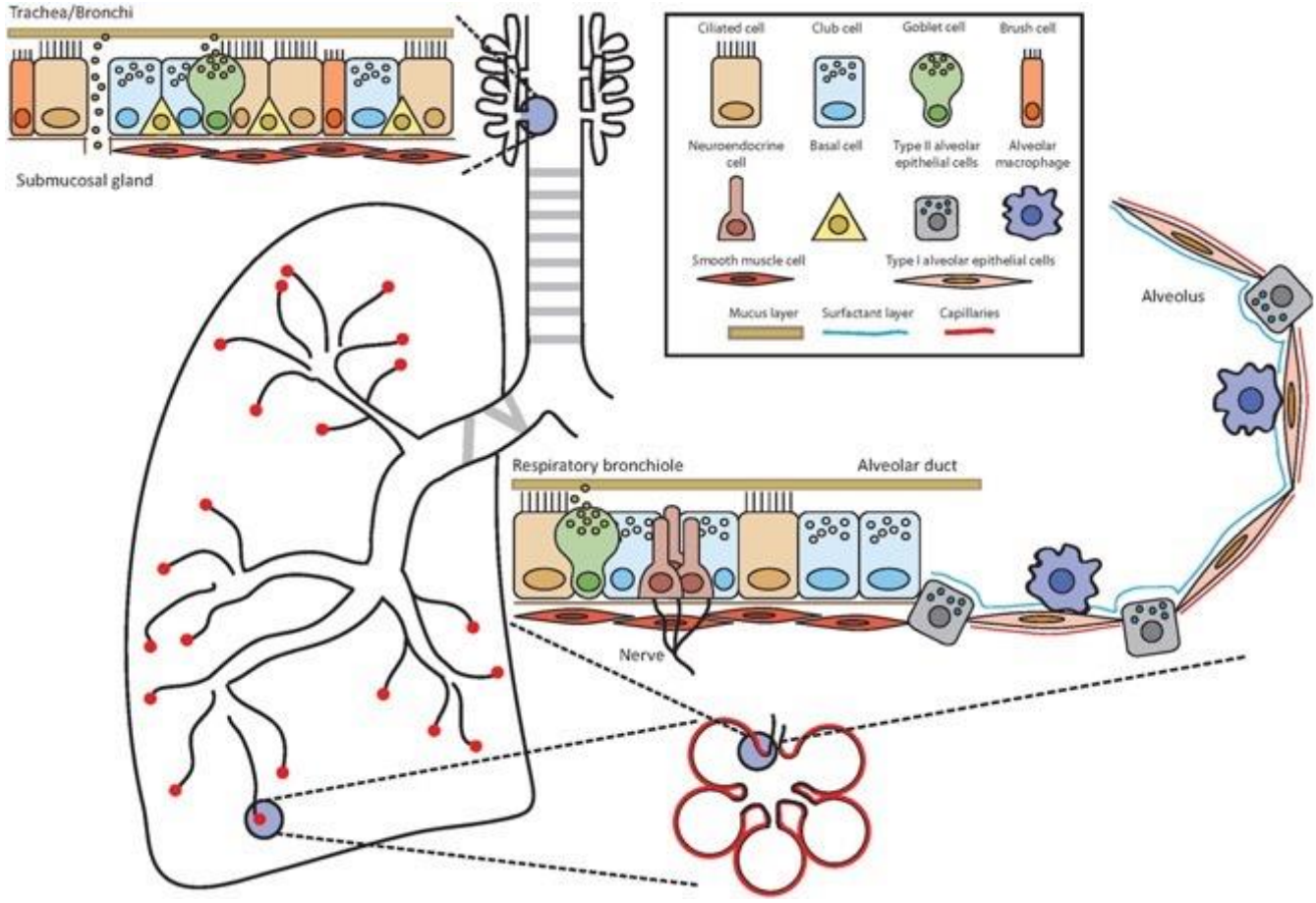

Figure 3. Anatomy of the airways. Throughout the airways, cell composition of the epithelium changes to ensure optimal and efficient gas exchange as well as maintenance of lung integrity and defense against potential pathogens and allergens. Depending on the location, the epithelium is composed of several different cell types such as ciliated cells, club cells, brush cells, goblet cells, airway smooth muscle cells, neuroendocrine cells, type I and type II alveolar epithelial cells, and alveolar macrophages. Basal cells have the potential to differentiate into several lineages and serve as stem cells (Mindt et al., 2018).

As the trachea bifurcates and smaller bronchioles form, so does cell composition progressively result in a simple columnar epithelium, which presents higher amounts of ciliated and secretory cells. This allows for an efficient removal of inhaled microorganisms (Rawlins et al., 2009; Rock & Hogan, 2011). Additionally, pulmonary neuroendocrine cells are now present (Figure 3). These cells are in close contact with sensory nerve fibers reacting to stimuli and releasing bioactive substances, such as serotonin, calcitonin, and bombesin (Van Lommel, 2001; Van Lommel et al., 1998).

In lung parenchyma, AECI and AECII cells comprise up to ~8 % of cells covering ~95–98 % of the surface area (Stone et al., 1992). These cells are found at the terminal bronchioles and alveoli. As illustrated in Figure 3, these are large squamous cells (~50–100 μm), whose thin (50–100 nm) cytoplasmic extensions form the epithelial wall of the air–blood barrier, performing gas exchange and ion and fluid transport (Dobbs & Johnson, 2007). Podoplanin is expressed in many cells, especially in alveolar epithelial cells I. In contrast, AECII are smaller (ø~10 μm), cuboidal cells which synthesize, secrete and recycle pulmonary surfactant, preventing alveolar collapse at low pressures and providing

host defense. Binding of surfactant to the surface of microbes causes microbe aggregation, thereby enhancing pathogen uptake and killing by alveolar macrophages (Pérez-Gil, 2008; Whitsett et al., 2010). Alveolar macrophages are professional phagocytes found in the pulmonary alveoli, near the pneumocytes, but separated from the wall. They are responsible for removing particles such as dust or microorganisms from the respiratory surfaces (Rubins, 2003). The alveolar macrophages are the third cell type in the alveolus.

During the saccular stage, AECI and AECII are derived from a common bipotent progenitor cell (Desai et al., 2014) (Figure 4). Amongst all mesenchymal cells, AECI and AECII play an especially important role during the saccular stage (Mižíková & Morty, 2015; Morrisey & Hogan, 2010). Mechanical forces and fibroblast growth factor (FGF) 10 are amongst recently-identified regulators of this differentiation process (Hogan, 2018; Li et al., 2018; Tang et al., 2018). After alveolarization, and in the adult lung, AECII acquire stem cell properties and are capable of self-renewal to replace AECI after injury (Barkauskas et al., 2013; Desai et al., 2014). As mentioned above, endothelial cells originate from the lung endoderm (Hogan, 2018; Tschanz et al., 2014; Yamamoto et al., 2007). Nonetheless, fibroblasts originate from the lung mesoderm (Chao et al., 2015; Hogan et al., 2014; Rinkevich et al., 2012; Ruiz-Camp & Morty, 2015). Murine fibroblasts have been proven to be influenced by retinoic acid and to have an impact secondary septation (McGowan et al., 1995). In rodents, by P5, so-called secondary septa appear in the primary septa at sites of elastin deposition (Morrisey & Hogan, 2010; Tschanz et al., 2014). At the secondary crest of these still-immature secondary septa, α-smooth muscle actin (αSMA) positive (+) myofibroblasts appear, and the expression of the extracellular matrix (ECM) components such as elastin further increases.

This secondary septation has been demonstrated to be dependent on platelet-derived growth factor (PDGF)-A signaling. Epithelial cells produce the ligand PDGF-A and signal via the affined receptor PDGF receptor (PDGFR)α, expressed by mesenchymal cells (Andrae et al., 2014; Boström et al., 1996, 2002) and responses such as cellular growth and differentiation, critical during the embryonic development (Lei & Kazlauskas, 2009).

In vivo studies have demonstrated that pulmonary PDGFRα^{+} cells serve as progenitor cells for lung myofibroblasts and a proportion of the pulmonary lipofibroblasts, present in the primary and secondary septa (Boström et al., 1996; Lindahl et al., 1997; McGowan et al., 2008; Ntokou et al., 2015). Expression of the ligands was detected in epithelial and smooth muscle cells, whereas the expression of PDGFRα was located to different mesenchymal cell populations (Gouveia et al., 2017), which is consistent with the prevailing view that epithelial-mesenchymal interactions are key mediators of lung development.

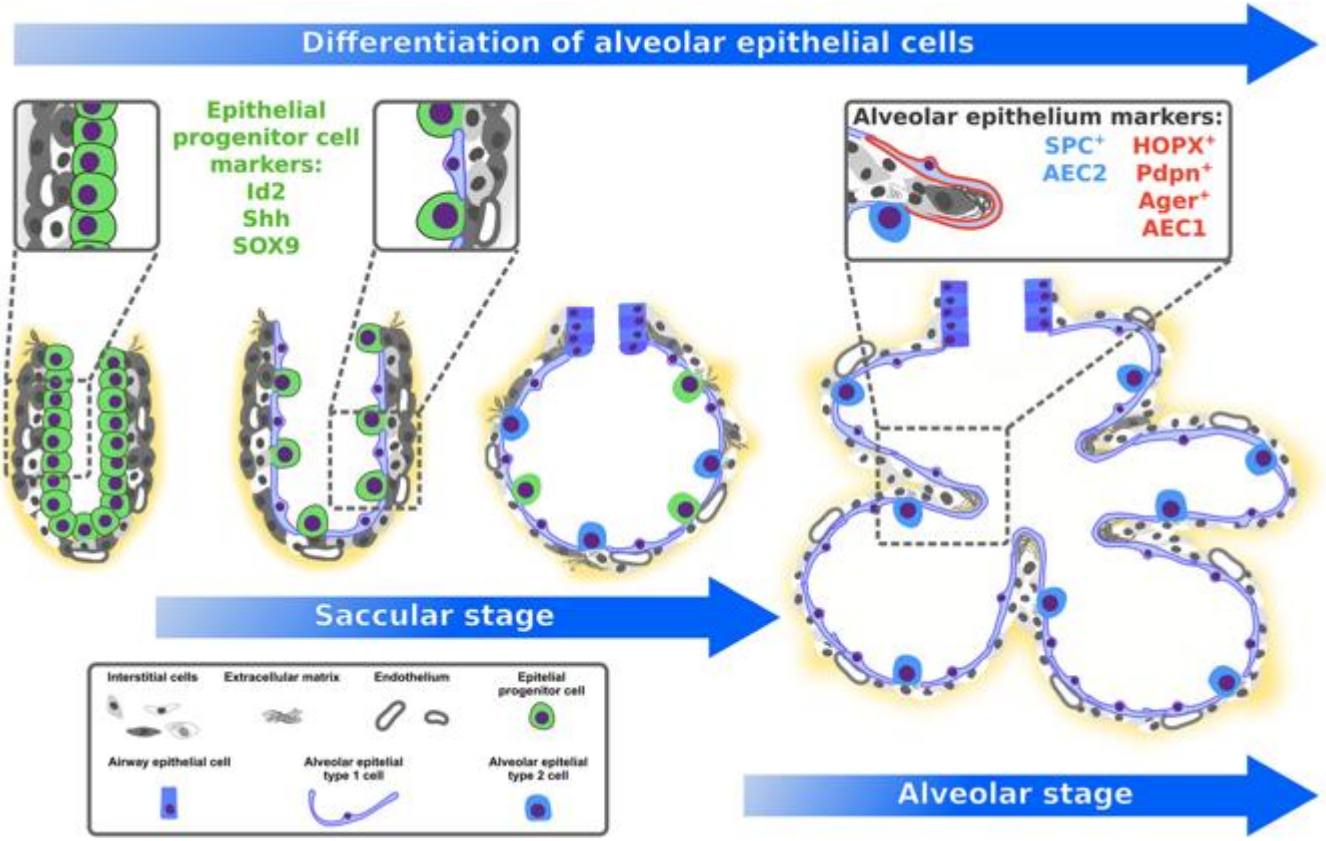

Figure 4. Alveolar epithelial cells during alveolarization. During the saccular stage, alveolar epithelial type I cells (AECI) and alveolar epithelial type II cells (AECII) are derived from a common bipotent progenitor cell. After differentiation single AECI can cover multiple alveoli during alveolarization and in the adult lung (Rodríguez-Castillo et al., 2018).

1.5. Using Stereology to quantify structural changes in lung development

Stereology is the method of choice for quantitative assessment of biological objects in microscopy (Knudsen et al., 2021) in order to estimate geometrical parameters that characterize the composition of a structure using a few samples from the entire organ. Light microscopy has to rely on measurements on nearly two-dimensional sections from embedded tissue samples, which results in qualitative and quantitative changes in the appearance of the sectioned structures. As result of the sectioning process, one dimension is lost along with important quantitative information (Mühlfeld et al., 2015). Typical global parameters are 3D (volume or size), 2D (surface area), 1D (length or thickness), or 0D (number). These parameters can be used to characterize any lung component (Hsia et al., 2010).

Notably, tissue embedding might alter the addressed quantification, so it is important to select the embedding method accordingly. Paraffin wax embedding is a widely used technique to infiltrate tissue samples with paraffin, which also presents great advantages when staining and solubility studies are expected for light microscopy. It is also the traditional standard in the field of pathology. However, it causes unpredictable tissue shrinkage, a significant disadvantage for proper quantification of structural changes (Hsia et al., 2010). Novel and updated approaches for more accurate embedding have arisen in

order to perform stereology. High quality results can be obtained with embedding using epoxy resins or glycol methacrylate (GMA). The latter has proved to be useful to support the generation of high-resolution images, to cause less tissue shrinkage as well as involving a more convenient and time saving handling process (Van de Velde, 1980). According to Schneider & Ochs, shrinkage due to paraffin embedding may directly influence the stereological measurements on a section, since a shrunken and therefore smaller cell, for example, occupies a smaller area on a section leading to fewer points hitting the cell profile during point counting (Schneider & Ochs, 2014). This publication demonstrated that paraffin embedding caused shrinkage of lung tissue up to 40 % of the relative area compared with GMA embedding where shrinkage was reduced to roughly 3 % of the relative area (Schneider & Ochs, 2014).
Quantitative data on lung structure are essential to stablish structure-function models for assessing the functional performance of the lung or to make statistically valid comparisons in experimental morphology, physiology or pathology (Weibel et al., 2007). The major problem in relating lung function measurements to morphological data is the need to assemble information on a three-dimensional structure from two-dimensional observations. Although data from 2D images have been widely used to describe pathological changes in lung structure, their relevance to physiological events occurring in 3D structures is limited (Brusasco & Dinh-Xuan, 2010). However, this problem can be solved by stereology, where it is possible to obtain valuable 3D morphometric data from 2D measurements. This method had its foundations laid by Buffon in 1777, who discovered the relationships between geometry and probability (Buffon, 1777). This opened the way for classical model-based stereology, which required an assumption of homogeneity of 3D structure. From a practical perspective, stereology is an assumption-free set of methods of unbiased sampling with geometric probes, based on a solid mathematical foundation (Weibel et al., 2007).
In order to understand the structure of lung parenchyma, three parameters, amongst others, are commonly used in lung stereology. Surface density (SV), is used to estimate the surface of the gas exchange of the lung parenchyma within the containing volume in cm^2/cm^3. This parameter can be multiplied by the volume of the lung to calculate the total surface area (Hsia et al., 2010). Mean linear intercept (MLI) is an estimator of volume-to-surface ratio of acinar airspaces $(V/S)_{airspace}$, alveoli and alveolar ducts taken together. It may be used as an indirect measure of air space enlargement as it measures a mean diffusion distance “from wall to wall” in the acinar air spaces but should at least be combined with a measure of total alveolar surface area. However, one has to be aware that the MLI strongly depends on inflation status (Pérez-Bravo et al., 2021) and the elastic properties of the lung (Mühlfeld et al., 2015). Also, septal thickness or arithmetic mean thickness measures alveolar tissue volume per surface area by ratio of tissue volume density to alveolar surface density. More specifically, it is a measure of the diffusion resistance

of air–blood barrier, where the thin barrier parts are weighed more heavily in the morphometric estimation of lung diffusing capacity (Hsia et al., 2010).

To this end the tool of stereology can be used to measure changes in structure during the development of the lung, which can be studied in different model organisms. Tschanz et al. investigated the number of alveoli during the process of alveolarization in rat lungs through a prolonged postnatal period, showing that alveolar development takes place with the major part of alveoli developing between days 4 and 21 of rat lung development and a second phase of alveolarization between 21 and 60 days of postnatal life (Tschanz et al., 2014). A similar study was carried out by Pozarska et al., who also investigated alveolarization between postnatal day 5 until 22 after birth (Pozarska et al., 2017). In this case, the parameters previously described were assessed and revealed noticeable morphological change during the considered timespan. Finally, postnatal human alveolarization was studied for the first time by Herring et al. using design-based stereology (Herring et al., 2014).

1.6. Studying in vitro alveolarization

The mouse model represents a valuable tool to analyze the process of alveolarization, since this process is largely postnatal in mice. Some of the advantages of *in vivo* alveolarization studies in mice are the possibility to perform cell type specific and inducible lineage tracing, cell and gene modulation, as well as cell ablation based on the CreERT2/loxP system (Rawlins & Perl, 2012). Differentiation processes, stem cell features, and morphological appearance can be analyzed in combination with high quality imaging approaches. However, *in vivo* modulation often results in early lethal phenotypes, which largely precludes a direct study of lung alveolarization. I*n vitro* approaches thus represent a potentially useful alternative to model important pulmonary newborn and infant diseases that carry significant human morbidity and mortality due to impaired alveolar development (Lignelli et al., 2019; Nogee, 2017). Some of the most studied diseases include bronchopulmonary dysplasia (BPD), congenital pulmonary airway malformations, and lung hypoplasia associated with congenital diaphragmatic hernia (Bohn et al., 1987; Bourbon et al., 2005; Kreiger et al., 2006). So far, there is a lack of model systems that can be used to understand underlying mechanisms of alveolarization involved in these and other diseases.

1.7. Precision-cut Lung Slices as model of alveolarization

Precision-cut lung slices (PCLS) are *ex-vivo* lung explants; three-dimensional lung tissue slices that contain nearly all cells that are usually found in the lung (G. Liu et al., 2019). *Ex-vivo* explants of many organs have been used for decades. Automated slicers can be used to cut thin sections (Parrish et al., 1995). Additionally, PCLS have been obtained from a wide range of species: mice, chicken, sheep, pigs

and humans (Meng et al., 2015; Rosales Gerpe et al., 2018; Siminski et al., 1992; W. Wu et al., 2010). The PCLS technology is currently still under development. The idea of using *ex vivo* tissue to study organ metabolism and toxicology was initiated in the 1920s with studies of the liver. Nonetheless, the need to cut each section manually resulted in high variability and had a strong effect on organ viability (G. Liu et al., 2019). During the 80s, infusion of hamster and rat lung airways with heated liquid agarose was used in an effort to maintain organ structure. When the agarose solidified, the inflated state of the lung prevented the collapse of the airways and protected the alveoli during slicing (Placke & Fisher, 1987). Although the main aim for tissue *ex-vivo* cultures was to toxicological assessment, newer applications soon arose. As the lung PCLS maintain the 3-dimensional (3D) architecture, this model was popularized to study the microenvironment of the respiratory tract (Akram et al., 2019a, 2019b; Bryson et al., 2020; Klouda et al., 2020). Additionally, as a large number of slices can be obtained from a single animal and remain stable in culture for weeks, large-scale screening of physiological and pathological responses can be performed (Bryson et al., 2020; Rosales Gerpe et al., 2018).

Furthermore, *ex-vivo* explants have shown to be a useful tool to study organogenesis at preliminary stages of lung development (Pederiva et al., 2012; van Tuyl et al., 2007). Many challenges have to be overcome in order to achieve a fully functional *in vitro* alveolarization model, since PCLS are highly limited by oxygen and nutrient diffusion. However, branching morphogenesis can still be evaluated using fetal murine lung tissue. Previous studies demonstrated that minced late-gestation fetal rat lungs can be grown semi-submerged in culture media, providing valuable results about the mechanisms of regulating surfactant production in response to hormonal stimulation. Nonetheless, the observation of alveolar septation was hindered by distal airspace collapse during the first 72 hours (h) in culture, and is yet to be demonstrated *in vitro* (Gross et al., 1978).

Different approaches have been used in this context. Pieretti et al. used lungs of postnatal mice inflated with agarose before the generation of the PCLS in order to preserve distal airway structure (Pieretti et al., 2014). There is evidence suggesting that this system can support secondary septation, cell proliferation and also allow for the identification of cell population components when postnatal mice lungs are used (Pieretti et al., 2014). This achievement unlocks a novel tool to identify the pathways involved in alveolar septation. Further new potential targets to model alveolarization could be evaluated to develop new therapeutic concepts for pulmonary diseases in children (Pieretti et al., 2014).

2. Hypothesis

Understanding the process of alveolarization is necessary, since it is key to develop new therapeutic strategies for pulmonary structural diseases. Unfortunately, *in vivo* approaches in mice often lead to lethal phenotypes and there are strong ethical concerns in the way of *in vivo* human studies of alveolarization. Therefore, the development of a suitable *in vitro* model to study alveolarization emerges as an attractive and indeed necessary alternative. The present study is aimed to characterize and validate current models of precision cut lung slices (PCLS) in postnatal mice to identify the best possible conditions to objectively validate structural changes upon in vitro alveolarization using stereology.

3. Materials

3.1. Equipment

Product	Manufacturer	Catalogue number
Analytical balance	VWR International	VWR-F1-100G
Biosafety cabinet, class II	NuAire	1500 Series B2
Centrifuge MiniSpin®	Eppendorf	5452000018
Centrifuge, Multifuge 3 S-R	Heraeus	75004371
Chemical fume hood	Norddeutsche Laborbau	ZH 1300
Confocal Laser Scanning Microscope	Carl Zeiss	LSM 710
Cooling ThermoMixer, HLC – MKR 13	Digital Biomedical Imaging Systems AG	MKR 13
Cryotome	Leica	CM3050 S
Digital Slide Scanner	Hamamatsu Photonics	NanoZoomer-XR C12000
Heating plate	Medax	12801
Hotplate/Stirrer	VWR	5052000000
Histobloc	Kulzer GmbH	64708995
Histoform Q Embedding Mould	Kulzer GmbH	12025
Incubator, Heracell vios 160i	Thermo Fisher Scientific	160i
Laminar flow hood	Thermo Fisher Scientific	Safe 2020
Magnetic stirrer	Heidolph Instruments	505-20000-00
Microcentrifuge	VWR	16NK / 823
Microscope Slides	Thermo Fisher Scientific	J3800AMNZ
Microtome	Leica	RM2255
Microtome Blades	Thermo Fisher Scientific	MX35 ULTRA
Microtome reusable Knife	Leica	14021604813
Paraffin embedding station	Leica	EG 1160
PCR System, ProFlex	Thermo Fisher Scientific	4484073
pH benchtop meter, SevenCompact Duo S213- meter.	Mettler Toledo	MT30130863

Precellys 24-Dual	VWR	432-3750
Precision Balance	Merck	Z676152-1EA
Pipetboy	Eppendorf	4430000018
Pipettes, automatic: 10 µl, 300 µl and 1000 µl	Eppendorf	4861000015 4861000031 4861000040
Pipettes, manual: 2,5 µl, 10 µl, 100 µl and 1 ml	Eppendorf	3123000012 3123000020 3123000047 3123000063
Real-Time PCR System, QuantStudio 3	Thermo Fisher Scientific	4376357
NanoDrop® ND-1000	Thermo Fisher Scientific	ND-ONE-W
StepOne™ Real-Time PCR System	Thermo Fisher Scientific	A26337
Stereomicroscope	Leica Biosystems	M50
Surgical instruments (various)	F.S.T	15006-09 14058-09 15370-26 11063-07 11052-10 11651-10
Ultra Microtome	Thermo Fisher Scientific	MX35
Ultraviolet transiluminator/Gel imager	Intas	GP-07LED
Vacuum Tissue Processor	Leica	ASP200 S
Vibratome	Leica	VT1200S
Vortex mixer	VWR	97043-562
Water bath	Carl Roth	HAC3.1

3.2. Reagents and drugs

Product	Manufacturer	Catalogue number
4',6-Diamidino-2-Phenylindole (DAPI)	Thermo Fisher Scientific	D3571
Acetone	Carl Roth	CP40.2
AccuStartTM II Mouse Genotyping Kit	Quantabio	733-2587
Agar	Sigma-Aldrich	05039
Agarose Ultra-Quality	Carl Roth	2267
Agarose Low Gelling Temperatur	Merck	A9414
Alexa fluor 488 secondary antibody	Thermo Fisher Scientific	A21121
Anti-Goat IgG	Sigma-Aldrich	MFCD00162340
Bovine Serum Albumin	Merck	A3059
Cacodylic acid·Na-salt·3H2O	Serv	15540.03
Click-iT EdU Cell Proliferation	Thermo Fisher Scientific	C10337
Cell Proliferation Kit I (MTT)	Merck	11465007001
Ceramic beads	Bertin GmbH	CK14
Citric acid monohydrate	Sigma	5949-29-1
DMEM/F12	Thermo fisher Scientific	11320033
dNTP Mix (10 mM)	Promega	U1511
Distilled water (dH_2O)	Thermo Fisher Scientific	10977023
Elastica staining	Morphisto	18553
Ethanol ≥99.8 %	Carl Roth	K928.3
Ethidium bromide solution 1 % (10 mg/ml)	Promega	H5041
Fluoromount W	Serva	21634
Glutaraldehyde 50 % solution in water 10 x 5 ml	Serva	23116.02
Goat serum	Sigma	G9023
Hardener II	Kulzer	66040437
Hematoxylin & Eosin staining	Morphisto	12156
HEPES solution1 M, pH 7.0-7.6	Merck	H0887

Hydrochloric acid (HCl)	Merck	100317
Hydrocortisone	Merck	H4001
Isopropanol	Carl Roth	T910.1
Insulin-Transferrin-Selenium (100x)	GIBCO	41400045
L-Ascorbic acid	Merck	A4403
M199, Earle's Salts	GIBCO	11150059
Magnesium chloride (25 nM)	Promega	A351H
Magnesium chloride (50 nM)	Bio-Rad	1708872
miRNeasy Mini kit	Qiagen, Germany	217004
M-MLV Reverse Transcriptase	Thermo Fisher Scientific	28025-021
Nuclease-free water	Thermo Fisher Scientific	AM9930
Osmium tetroxide	Carl Roth	8371.3
Paraffin, Paraplast	Leica	39601095
Paraformaldehyde	Merck	P6148
Penicillin - Streptomycin for cell culture (10.000 U/mL)	Thermo Fisher Scientific	15140122
Pertex mounting medium	WVR	LEIC811
Phosphate buffered saline (1x and 10x)	Merck	D8537 D1408
Platinum SYBR Green qPCR SuperMix-UDG	Thermo Fisher Scientific, USA	11733046
Podoplanin antibody	R&D Systems	AF3244
Random Hexamers (50 µM)	Thermo Fisher Scientific, USA	N8080127
REDTaqReadyMix	Sigma	R2523
Retinoic acid	Merck	R2625
Silica Gel	Carl Roth, Germany	P077.1
Sodium hydroxide (NaOH)	Carl Roth	H290-H314i
Technovit 7100	Kulzer	64709003
Technovit Universal Liquid	Kulzer	66022678
Technovit 3040	Kulzer	64708806
Tris(hydroxymethyl)aminomethane (TRIS)-EDTA	Carl Roth	4855.2

Triton x 100	Merck	T8787
TWEEN 20	Merck	655204
Type 1 rat tail collagen	BD Biosciences	354236
Uranyl Acetate	Serva	77870.02
Water for injection	Thermo Fisher Scientific	A12873-01
Xylol	Carl Roth	3791.1

3.3. Primers for genotyping and qPCR

Gene	Forward (5'- 3')	Reverse (5'- 3')
R26 mTmG mice	CTCTGCTGCCTCCTGGCTTCT	CGAGGCGGATCACAAGCAATA
CAGP mTmG mice	CTCTGCTGCCTCCTGGCTTCT	TCAATGGGCGGGGGTCGTT
oIMR7801-WT	CCCTTGTGGTCATGCCAAAC	GCTTTTGCCTCCATTACACTGG
oIMR7919-Mut_PDGFRα-GFP mice	CCCTTGTGGTCATGCCAAAC	ACGAAGTTATTAGGTCCCTCGAC
ACTA2	CTGACAGAGGCACCACTGAA	CATCTCCAGAGTCCAGCACA
COL1A1	AGACATGTTCAGCTTTGTGGAC	GCAGCTGACTTCAGGGATG
MKI67	ACCGTGGAGTAGTTTATCTGGG	TGTTTCCAGTCCGCTTACTTCT
PDPN	CACCTCAGCAACCTCAGAC	ACAGGGCAAGTTGGAAGC
PDGFRα	GTCGTTGACCTGCAGTGGA	CCAGCATGGTGATACCTTTGT
SFTPC	ACCCTGTGTGGAGAGCTACCA	TTGCGGAGGGTCTTTCC
VIM	CCAACCTTTTCTTCCCTGAA	TGAGTGGGTGTCAACCAGAG

Abbreviations: *mTmG*: Gt(ROSA)26Sortm4(ACTB-tdTomato,-EGFP)Luo/J; PDGFRα-GFP: B6.129S4-PDGFRαtm1.1(EGFP)Sor/J; R26: Rosa26; *WT*: wildtype.

3.4. Consumables

Product	Manufacturer	Catalogue Number
Cover slides	Carl Roth	H878.2
Embedding cassetes	Rotilabo, Carl Roth	K113.1
Filter pipette tips: 10 µl, 100 µl, 200 µl, 300 µl, 1 ml	Greiner bio-one	771261 737261 737258 738261 738255 750255
Histobloc for Histoform S & Q	Morphisto	11282
iSpacer one well, 0.25 mm deep	SunJin Lab	IS213
Microcentrifuge tubes: 0.5, 1.5 and 2 ml	Eppendorf	0030121023 0030120086 0030120094
Pasteur pipette, 3.5 ml	Sarstedt	86.1171.001
Petri dishes	Carl Roth	N221.2
Safety Cannula, 26G, 24G and 22 G, Vasofix	B. Braun Melsungen	260091 4269071S-01 4268091S-01
Suture Thread	SMI, Belgium	4015X
SuperFrost Ultra Plus Adhesion slides	Thermofisher Scientific	11976299
Syringes 1 ml	B. Brtaun Melsungen	9166017V
Technovit Histoform Q	Morphisto	15068
Test tubes: 15 ml and 50 ml	Thermo Fisher Scientific	339650 339652

3.5. Software

Name	Company
Fiji	NIH, USA
GraphPad Prism v8.3	GraphPad Software, USA
Microsoft Office	Microsoft, USA
NDP	Hamamatsu Photonics, Japan
StepOne Plus software v2.3	Thermo Fisher Scientific, USA
Visiopharm’s newCAST	Visiopharm A/S, Denmark
ZEN 3.1	Zeiss, Germany

4. Methods

4.1. Experimental mice

Mice were maintained on a 12:12 h dark-light photoperiod cycle and provided with food and water *ad libitum*. Pups of post-natal days (P) 3, 4, 7, 8, 12 and 14 from different lines (4.1.1. and 4.1.2) were euthanized by pentobarbital overdose (500 mg/kg) administered by intraperitoneal injection.

4.2. Wild-type mice

Unless noted otherwise, wildtype-C57BL/6J mice were employed for organ harvesting. Mice were regularly ordered from the company Charles River Laboratories, USA, and Janvier Labs, France.

4.3. Transgenic mice

Lung tissue of dead Gt(ROSA)26$^{Sortm4(ACTB-tdTomato,-EGFP)Luo/}$J (mTmG) mice was harvested and analyzed by confocal laser scanning microscopy (CLSM) in order to quantify lung structure. This mouse line expresses red fluorochome membrane tandemTomato (mtdTomato) in all cell membranes from the Rosa26 gene locus. A second reporter gene for green fluorescent protein (GFP) is separated by a stop codon in line with the mtdTomato and loxP sequences are flanked by part of the dTomato sequence and the stop codon. After crossing this line with Cre-mediated recombination, the stop codon was removed, resulting in GFP expression in lieu of mtdTomato. This fluorescent protein, expressed in all lung cellular membranes at the parenchyma, allowed fora morphometric visualization by confocal microscopy. The mouse line we have just described was purchased at The Jackson Laboratory company with the stock ID: 007576 (Muzumdar et al., 2007).

Additionally, B6.129S4-PDGFRα$^{tm1.1(EGFP)Sor/}$J (PDGFRαGFP) mice were used to analyze the presence of PDGFRα positive cells in PCLS. These mice express the h2B-eGFP fusion protein (knock-in) under the endogenous PDGFRα promoter. This allows the precise expression pattern of the gene to be visualized at the respective development time-point. This mouse line was obtained from The Jackson Laboratory stock ID: 007669 (Hamilton et al., 2003).

4.3.1. Genotyping transgenic mice

Standard PCR and subsequent DNA electrophoresis were performed to verify the genotype of the loci of interest in transgenic mice. DNA was extracted from a piece of tail tissue from P3–P14 mice using the AccuStartTM II Mouse Genotyping Kit following the manufacturer's protocol. The specific PCR master mix and cycling parameters are listed in Tables 1 and 2, respectively. The PCR products were subsequently loaded in agarose gels (1–1.5 % [*w*/*v*]), containing ethidium bromide (0.2 μg/ml) and run in an electrophoresis chamber to resolve the amplified DNA fragments. DNA bands were visualized and documented with a transilluminator.

Table 1. Master mix for genotyping of transgenic mice.

Components	Volume per well (μl)
mTmG	
ddH_2O	5.5
2X KAPA2G Mix	12.5
Forward primer (10 μM)	1.25
Reverse primer (10 μM)	1.25
DMSO	2
DNA	2
Total	25
PDGFRα-GFP	
ddH_2O	9.25
REDTaqReadyMix	9.25
Forward primer (10 μM)	0.25
Reverse primer (10 μM)	0.25
DNA	1
Total	20.25

Abbreviations: *mTmG*: Gt(ROSA)26Sortm4(ACTB-tdTomato,-EGFP)Luo/J; PDGFRα-GFP: B6.129S4-PDGFRαtm1.1(EGFP)Sor/J;

Table 2. Cycling parameters used for genotyping of transgenic mice.

Mouse line	Reaction		Temperature	Time
mTmG	Denaturation		95 °C	3 min
	Denaturation	36 ×	95 °C	20 s
	Annealing		62 °C	60 s
	Extension		72 °C	50 s
	Final Extension		72 °C	5 s
	Storage		4 °C	∞
Mouse line	**Reaction**		**Temperature**	**Time**
PDGFRα-GFP	Denaturation	30 ×	94 °C	15 s
	Annealing		55 °C	15 s
	Extension		72 °C	30 s
	Denaturation	36 ×	94 °C	30 s
	Annealing		65 °C	60 s

Extension	72 °C	60 s
Final Extension	72 °C	2 m
Storage	4 °C	∞

Abbreviations: *m*, minutues: *mTmG*: Gt(ROSA)26Sortm4(ACTB-tdTomato,-EGFP)Luo/J; PDGFRα-GFP: B6.129S4-PDGFRαtm1.1(EGFP)Sor/J; *s*, seconds.

4.4. Tissue processing

4.4.1. Preparation of lung organ culture

Animals for organ harvest were first euthanized as previously described (P3) and the chest was opened via sternotomy, whereby the left atrium and right ventricle were incised. Pulmonary vessels were perfused with phosphate-buffered saline (PBS) maintaining a cannula (26G) through the right ventricle to flush erythrocytes out of the lung to the left atrium. Then, the lungs were inflated intratracheally with the 26G-cannula using DMEM cell culture medium supplemented with 1 % penicillin–streptomycin (PS). Finally, the cannula was fixed and knotted to the trachea and closed with a cap. Lungs were then removed from the thorax, and heart and thymus were discarded. Lungs were inflated to increase the pressure up to 5 times per day and were incubated in a Petri dish with the above culture medium, which was changed daily.

4.4.2. Preparation of the Precision Cut Lung Slices

Mice were euthanized according to 4.1. The chest was opened via sternotomy and left atrium and right ventricle were incised. For comparison purposes, three different PCLS Protocols (PCLS_P) were followed.

4.4.3. Preparation of 200-µm-thick P3 and P7 PCLS (PCLS_P 1)

The first protocol was kindly provided by Prof. Dr. Saverio Bellusci's laboratory for Lung Matrix Remodeling in Giessen (Germany). For this protocol P3, P7 and P14 animals were used. Pulmonary vessels were perfused with PBS through the right ventricle to flush erythrocytes out of the lung to the left atrium (maintaining a 26G cannula for P3, a 24G cannula for P7 and, a 22G cannula for P14). Lungs were next inflated intratracheally using the appropriated age-specific cannula at 20 cm H_2O pressure with 1 % low-melting-point agarose prepared with DMEM/F12 for 10 minutes. Finally, the trachea was ligated to prevent leakage, lungs were harvested and were incubated in ice-cold medium until vibratome slicing could be performed.

4.4.4. Preparation of 300-µm-thick P3 PCLS (PCLS_P 2)

The second protocol followed Akram et al. with minor modifications (Akram et al., 2019a). Also, P3, P7 and P14 animals were used without perfusion. Lungs were harvested and filled via trachea with 1.5 % low-melting-point agarose prepared with 1× HBSS/HEPES Buffer for 10 minutes using an age-dependent quantity: 0.2 ml for P3, 0.27 ml for P7 and, 0.35 for P14.

4.4.5. Preparation of 1,000-µm-thick P4 PCLS (PCLS_P 3)

The third protocol followed Pieretti et al. (Pieretti et al., 2014).This protocol included P4, P8 and P12 animals and pulmonary vessels were perfused with 0.1M Sodium citrate at 15 cm H_2O pressure for 15 min. Lungs were harvested and filled via trachea using 20 cm H_2O pressure for 10 minutes with 0.4 % low-melting-point agarose prepared with culture medium M199 using an age-dependent quantity.

4.4.6. PCLS culture

Once lungs were harvested and prepared for slicing, separated lobes were embedded into agarose (5 %) blocks for vibratome sectioning. All procedures followed the same culture proceeding, with exception of the medium used in each case: for the method described in the PCLS_P 1 supplemented (1 % PS and 0.1 % amphotericin B) DMEM/F12 medium was used; while the methods described in the PCLS_P 2 and PCLS_P 3 used a collagen matrix with supplement (1x Insulin/Transferrin/Selenium; 2 mg/ml of ascorbic acid; 1 mg/ml of retinoic acid; and, 0.1 mg/ml of hydrocortisone) serum-free M199 media with 1 mg/ml Tail Rat Collagen I to attached PCLS to the well. Supplemented (1x Insulin/Transferrin/Selenium; 2 mg/ml of ascorbic acid; 1 mg/ml of retinoic acid; and, 0.1 mg/ml of hydrocortisone) M199 media without Tail Rat Collagen I was used for incubation.

In all scenarios, PCLS were incubated at 37ºC for 2 h and washed twice with the warm medium described in each protocol in order to remove the agarose from the tissue. Then, slices were cultured at 37ºC in presence of 5 % CO_2 for different time points depending on the protocol: 24h and 72h for the 200-µm-thick P3 and P7 PCLS; 72h for 300-µm-thick P3 and, 96h for the 1,000-µm-thick P4 PCLS.

Once the expected culture time was reached, PCLS were fixed with paraformaldehyde (PFA) at 4 % and glutaraldehyde at 0.1 % during 24h previous embedding them in paraffin (4.4.9) or glycol-methacrylate (GMA) (4.4.10).

4.4.7. Proliferation assay

Cell proliferation was measured with 5-Ethinyl-2′-deoxyuridin (EdU) for organ and PCLS cultures. This compound is a thymidine analogue which is incorporated into the DNA of dividing cells. EdU is used to assay DNA synthesis in cell culture and labels cells in embryonic, postnatal and adult animals which

have undergone DNA synthesis (Chehrehasa et al., 2009). The assay was carried out following the manufacturers' protocol with a few modifications. From a 10 mM EdU/ DMSO (*w*/*v*) stock solution, a final concentration of 20 μl EdU per ml of cell culture medium was prepared. This master solution was always prewarmed before adding 1ml of this solution to 1 ml of culture medium, keeping a final concentration of 10 μl of EdU per ml of medium. Lungs or PCLS in EdU-medium solution were cultured for 24h. Subsequently, the EdU-medium was removed and 1 % PFA (*w*/*v*) was added in order to fix the tissue, which was incubated overnight at 4ºC. The fixative solution was then removed by washing the PCLS twice with 3 % BSA in 1x PBS (*w*/*v*). Visualization of the EdU in tissue was preceded by a permeabilization step performed with 1 % Triton X-100 in PBS (*v*/*v*) at room temperature (RT) for 30 minutes (min). Once the permeabilization solution had been removed by washing the tissue twice with 3 % BSA in PBS 1X (*w*/*v*) a cocktail solution was added (listed in Table 3) and incubation for 2h at RT was carried out. Finally, PCLS were washed with 1x PBS and mounted on slides with Fluoromount W using properly-sized spacers. Every section was analyzed using a confocal laser scanning microscope.

Table 3. Cocktail solution for EdU detection

Component	**Concentration stock solution**	**Final concentration**
Tris-HCl (10 mM, pH 8.5)	143 mM	100 mM
Alexa Fluor 488 Azide	20 μM	10 μM
Copper II sulfate pentahydrate	20 mM	1 mM
Sodium ascorbate	500 mM	100 mM
DAPI	14.3 mM	2 μM

4.4.8. MTT assay

In 1980, MTT dye was first reported as an indirect measure of cell number (Mosmann, 1983). The basis of the assay is to expose cells in the exponential phase of growth to a cytotoxic drug or condition. Living cells are able to metabolize MTT dye. Surviving cell numbers are then determined indirectly by MTT dye reduction. The MTT dye is a yellow water-soluble tetrazolium dye that is reduced to a purple formazan product that is insoluble in aqueous solutions (Y. Liu et al., 1997). The amount of MTT-formazan produced can be determined by absorbance measurement. For this assay, 200-μm-thick P3 and P7 PCLS were plated in 12-well plates and cultured during 24h and 72h. Our procedure followed the manufacturer's protocol. MTT labelling reagent was added to PCLS culture medium and PCLS were incubated in a humidified atmosphere at 37ºC, 5 % CO^2 for 4h. Next, a solubilization solution was added

to disrupt the tissue, after which the plates were cultured overnight at the above mentioned humidified atmosphere. Absorbance was measured at 550 nm.

4.4.9. Paraffin tissue processing

Samples were sliced into thin sections in order to be prepared for examination by light microscope. Lung tissue PCLS were first dehydrated using a Leica ASP200S tissue processor, and next embedded with Leica EG1160 and Leica EG1150C in paraffin blocks. Then, lung tissues were sectioned into 4-µm-to 5-µm sections using a Leica RM2255 microtome and allowed to dry at RT. Deparaffinization of the slides step was carried out by heating at 59 °C for 60 min.

4.4.10. Glycol-methacrylate tissue processing

Samples were prepared for embedding in Glycol methacrylate by performing four washing steps of 5 min each with 0.1 M sodium cacodylate buffer prior 2 h treatment with 1 % (*w*/*v*) osmium tetroxide (OsO4) dissolved in 0.1 M sodium cacodylate buffer. Subsequently, lung tissues were once again washed four times (5 min each) with 0.1 M sodium cacodylate buffer followed by a 4-times distilled water (ddH_2O) washing step. Lung tissues were then treated overnight with half-saturated uranyl acetate buffer. Four washing steps with ddH2O were applied, followed by a series of washings with increasingly concentrated acetone [70 % (*v*/*v*) twice for 1 hour; 90 % (*v*/*v*) twice for 1 hour; 100 % (*v*/*v*) once for one hour]. After dehydration, samples were maintained overnight in a 1:1 mixture of 100 % (*v*/*v*) acetone and Technovit 7100-Hardener I. Then, samples were transferred to Technovit-Hardener I solution for 24h followed by 5 min incubation with Technovit 7100-Hardener I-Hardener II under continuous rotation. Lung tissues were subsequently transferred to Histoform Q molds while still submerged on Technovit 7100-Hardener I-Hardener II mixture, which was allowed to polymerize for at least 48h. A final step using Technovit 3040 mixed with Technovit universal liquid (3:1) was used to fix the Histoblock adapters to the GMA tissue blocks. Blocks were then removed from the molds and stored at RT before sectioning. Finally, GMA blocks were sectioned in 2-µm sections with a reusable d-profile steel microtome knife. Single sections were obtained every 20 µm for a total of 4 sections per lung (i.e.: sections 1, 11, 21 and 31). Upon collection of the tissue, slides were left to dry at 65 °C.

4.5. Staining of lung tissue for stereological analysis

4.5.1. Elastica staining

Elastica staining was performed according to previous publication (Pieretti et al., 2014). Slides were washed twice 5 min in Xylol, followed by a 2 min step of series of progressively reduced ethanol concentration [96 % (*v*/*v*), 80 % (*v*/*v*), and 70 % (*v*/*v*)], subsequently submerged for 15 min in Resorsin-

Fuchsin solution. Lung tissues were next washed for 1 min in tap water before counter-stained with Weigert hematoxylin for 5 min. Tissue was subsequently washed for 15 min in tap water, followed by 5 sec in 1 % hydrochloric acid/70 % alcohol (*v*/*v*), and 5 sec in ddH_2O. Next, Van Gieson solution was used in order to stain collagen and the cellular cytoplasm. Once staining was carried out, tissue was once again progressively dehydrated [twice submerged for 2 min in 96 % (*v*/*v*) ethanol, once for 2 min in 2-propanol 99.8 % (*v*/*v*) ethanol and twice for 5 min in Xylol] and mounted with Pertex. Images were generated by using the Nanozoomer at bright field.

4.5.2. Hematoxylin and Eosin staining

Slides were twice washed in Xylol for 5 min, followed by 4 min steps of reduced ethanol concentration [96 % (*v*/*v*), 80 % (*v*/*v*), 70 % (*v*/*v*), and 60 % (*v*/*v*) ethanol] followed by a 2 min ddH_2O washing step. Lung tissues were next stained with Mayer Hematoxylin solution during 5 min followed by a 5-min tap water washing step. Following, 5 min submersion step in aqueous Eosin 1 % (*v*/*v*) and 5 min washing step in tap water were performed. Finally, tissues were dehydrated [twice submerged for 2 min in 96 % (*v*/*v*) ethanol, once submerged for 2 min in 2-propanol 99.8 % (*v*/*v*) ethanol and twice submerged for 5 min in Xylol] and mounted with Pertex. Images were generated by using the Nanozoomer at bright field.

4.5.3. Richardson´s staining

Sections were incubated with Richardson's stain for 30 sec at 65 °C and were serially washed in cold, hot, and double-ddH_2O water. Finally, sections were fixed in Roti®-Histol and allowed to dry before imaging.

4.5.4. Morphometrical measurements in stereology

Stereological analysis was performed using the Visiopharm® NewCast computer-assisted stereology system. SV was measured by counting line intersections within the parenchyma of the lungs (Madurga et al., 2014). To this end, SV was calculated using the following formula: $SV = 2 \times (\Sigma I) / (lp \times \Sigma P)$, where "*I*" indicate number of counted intersection; "*lp*" is the length (μm) of the line between two points; and, "*P*" refers to counted reference points inside parenchyma. Then, MLI was calculated according to the next formulae (Hsia et al., 2010). From surface density, the MLI can be calculated using the formula $MLI = 4V(alv/lung) / S$, where *V*(alv/lung) refers to volume of alveolar air space. Also, septal wall thickness (τ) can be estimated: $\tau(sep)[\mu m] = 2V(sep/lung) / S$, where V(sep/lung) is the volume of septa in the parenchyma. Finally, to ensure precision of measurements, the coefficient of error (CE), the coefficient of variation (CV) and the ratio between squared (CE2/CV2) were measured for each parameter.

4.6. Gene expression analysis

4.6.1. Total RNA isolation and cDNA preparation

Total RNA was isolated from P3, P7 and P14 mouse lungs and PCLS using the miRNeasy Mini kit following manufacturers protocol. Tissue was placed into a 2 ml tube containing ceramic beads and homogenized using a Precellys 24-Dual. Total RNA was then resuspended in 30 µl nuclease-free water and concentration was determined using a NanoDrop One Microvolume UV-Vis Spectrophotometer. Subsequently, cDNA was prepared using 800 ng/µl RNA. Master mix using the reagents listed in Table 5 were used in order to prepare a final volume of 40 µl. Real time polymerase chain reaction (qPCR) was carried out using Platinum SYBR Green qPCR SuperMix-UDG to analyze changes in gene expression for mRNA. The qPCR was assessed in the StepOne Real-Time PCR System and cycling conditions are reported in Table 5 for the genes listed (3.3). For qPCR analysis, ΔCt were assessed as mean Ct $_{(\text{reference gene})}$ − Ct $_{(\text{gene of interest})}$, where the *Polr2a* gene was used as reference genes for mRNA. Primer pairs were designed intron-spanning and were validated prior experimental design.

Table 4. Master mix used to prepare cDNA for gene expression analysis.

Component	1 sample (µl)	
Nuclease-free H_2O	1	
GeneAmp 10× PCR Buffer	4	
Magnesium chloride solution (25 mM)	8	
dNTP Mix (10 mM)	2	
Random Hexamers (50 µM)	2	
RNase Inhibitor (20 U/µl)	1	
M-MLV Reverse Transcriptase (50 U)	2	
RNA (1000 ng/µl)	20	
	Total	40

dNTP, Deoxynucleotide Triphosphates; M-MLV, Moloney Murine Leukemia Virus.

Table 5. Cycling conditions used for qPCR gene expression.

Step	Reaction		Temperature	Time
1	Denaturation		95 °C	5 min
2	Denaturation	40×	95 °C	5 s
3	Annealing		59 °C	5 s
4	Extension		72 °C	30 s
5	Final Extension		72 °C	5 min
6	Melting Curve Analysis			30 min
7	Storage		4 °C	∞

4.7. Imunostaining in histological sections

4.7.1. Podoplanin immunostaining

Slides were heated at 60 °C for 1 h to melt paraffin. Once dewaxed, rehydration was started by 3-times immersion in Xylol, 10 min each. Slides underwent reduced ethanol concentration series [twice in 100 % (*v*/*v*) ethanol 5 min; one in 96 % (*v*/*v*) ethanol 5 min; once in 70 % (*v*/*v*) ethanol 5 min]. Then, sections were washed for 5 min in PBS in light and boiled citrate buffer for 20 min [0.21 % (*m*/*v*) citric acid monohydrate, 0.05 % Tween 20 (*v*/*v*) pH 6]. After cooling down, slides were washed for 5 min in PBS and sections were blocked with 5 % (*m*/*v*) BSA for 1 h. Following, an additional PBS-washing step for 5 min was carried out prior overnight incubation with Podoplanin primary antibody (1:100; goat serum). Subsequently, a PBS washing step for 5 min was carried out prior slides were incubated with Alexa-488 secondary antibody (1 h at RT). A final washing step (5 min in PBS) was carried out prior staining using DAPI (1:5,000 in PBS, 5 min). Slides were mounted with Fluormount and covered with a cover glass. Images were taken using a confocal laser scanning microscope and analyzed using the ZEN 3.1 software.

4.8. Image processing, analysis and figure preparation

4.8.1. Generation of digital images

Images from brightfield whole-slide scans were captured with the NDPIview2 software (Hammatsu Photonics K.K., Hamamatsu City, Japan). FIJI/ImageJ and Zen software were used to perform adjustments of brightness and contrast to epifluorescent and confocal images as well as for generating 3D renderings and projections of Z-stacks. Graphs were prepared with the software GraphPad Prism.

4.8.2. Automated proliferation counting from tissue sections

Z-stack sections files from PCLS imaging were analyzed using FIJI/imageJ software and following the automated cell counting protocol stablished (Shihan et al., 2021). The Z-stack of 50 to 100 μm range files were obtained by confocal laser scanning microscop with a 25X objective, pinhole of 1 UA and an internal of 1μm. Then, area of the total and proliferating cells was obtained from FIJI and calculated as percentage of cell in proliferation using the next formula:

$$\boldsymbol{Percentaje\ of\ proliferating\ cells} = \frac{\boldsymbol{Percenaje\ of\ EdU\ positive\ cells}}{\boldsymbol{Percentaje\ of\ DAPI\ positive\ cells}} * \mathbf{100}$$

4.8.3. Analysis of lung structure and estimation of structural parameters of the lung

Quantitative assessment of lung structure was performed using design-based stereology, following the recommendations emitted by the American Thoracic Society and the European Respiratory Society on the matter Hsia et al., 2010. The Visiopharm newCAST software was used for stereological analyses of scans.

4.9. Statistics

Statistical analyses were performed using Prism v8.3. software. Unless noted otherwise, data are presented as mean ± SD. Differences were evaluated with t-test (unpaired, unless noted otherwise) for comparisons between two groups. Differences between more than two groups were evaluated by one-way ANOVA with Tukey's post hoc test. *P* values lower than 0.05 were considered to be statistically significant.

5. Results

The present study aims to characterize murine PCLS during the postnatal period of alveolarization. Cell type specific marker expression, viability and proliferation were assessed together with a characterization of lung architecture using different types of stereological approaches.

5.1. Establishment of two different in vitro tissue systems: entire lung versus PCLS

As a first step, two different *in vitro* culture systems were compared: entire lung vs. PCLS culture. The first approach, involving a complete organ in culture, was carried out in order to avoid tissue disruption, thus allowing the lung to undergo normal development (Figure 5). The second approach using PCLS was included because of easier handling and because PCLS were already established.

Agarose solution was used to maintain structure in both scenarios, and a liquid medium was used to culture the tissues. Complete lungs and 200-µm thick PCLS were obtained from mice and subsequently cultured for 24h or 72h. In both cases, cell proliferation addressed after the first 24h. 2.2 % proliferation was observed in the entire lung culture, whereas 2.3 % proliferation was observed in PCLS. After 72h in culture, 0.21 % cell proliferation was observed in the entire lung while cell proliferation in PCLS remained stable (2.5 %) when compared to the same culture at the 24h mark (Figure 5).

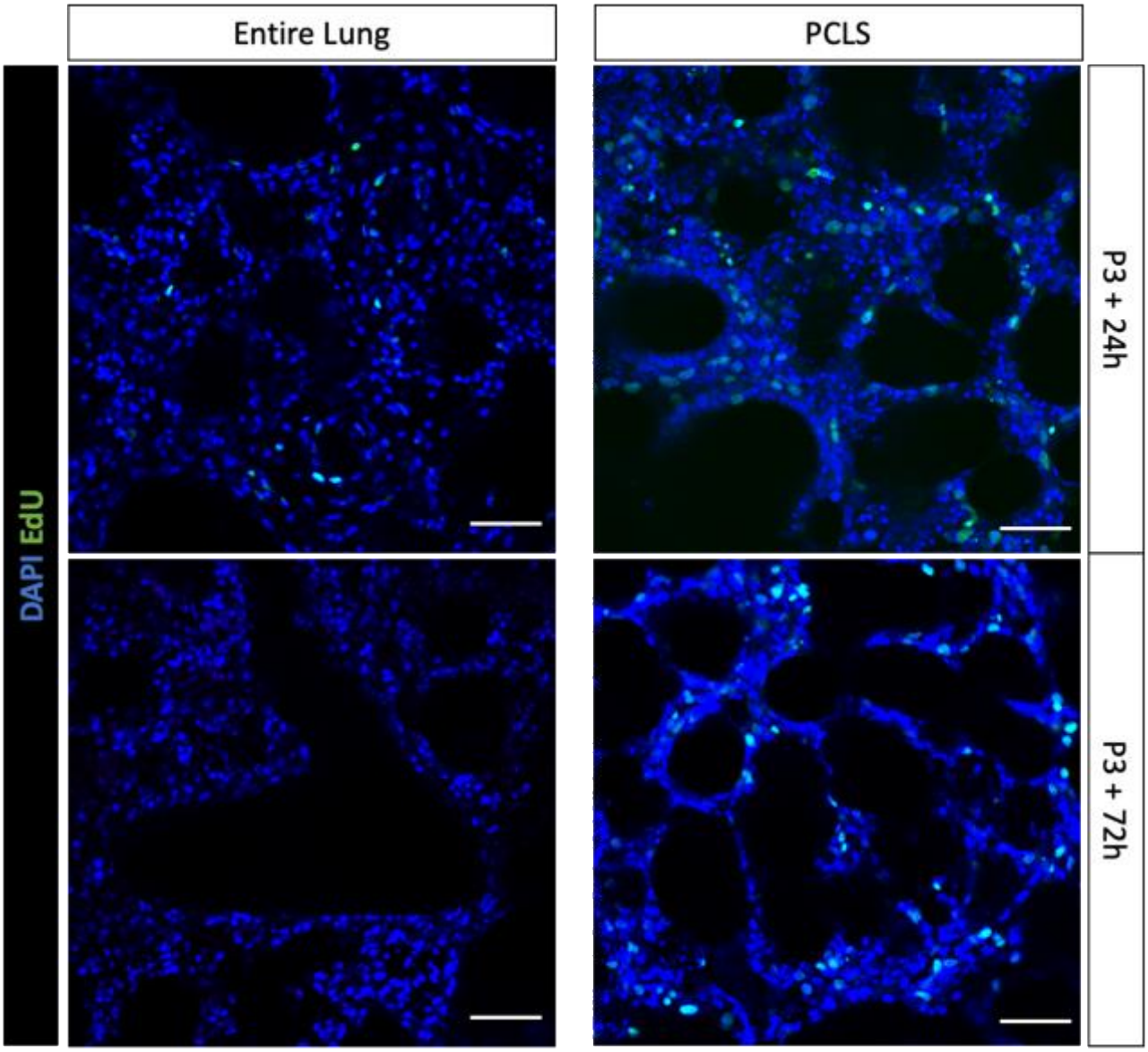

Figure 5. Cell proliferation of entire lung culture vs PCLS culture. Cell proliferation in P3 murine entire lungs and 200-µm thick P3 PCLS was determined after 24 and 72h in culture (*n* = 3 per time point). EdU: Alexa Fluor 488 (green). Nucleus: DAPI (blue). Scale bar: 50 µm.

To study alveolarization *in vitro*, a system stable enough to be evaluated for at least 72h is necessary in order to recognize structural changes, a requisite that is generally not met by the entire lung culture. In contrast, the PCLS approach offered promising results, so that this approach was selected to continue analyzing alveolarization *in vitro*.

5.2. Assessment of short-term cultivated murine PCLS

5.2.1. PCLS proliferation and viability

Following previous results, PCLS were chosen as the optimal tool for this project. Evaluation of proliferation as a feature of maintenance of cellular integrity after short-term (up to 72h) cultivation of murine lung PCLS was the next step. PCLS were obtained from P3 and P7 mice and cultured for 24h or 72h. Proliferating EdU-stained cells were notably visible in both 200-µm thick P3 and P7 PCLS after 24h and 72h in culture (Figure 6). In order to address differences between different conditions, cells were counted and analyzed for each of the above-mentioned conditions (Figure 6 B–E). Notably, significant differences were obtained between the different time-points for both P3 and P7 PCLS (Figure 6 B–D). However, when *in vitro* PCLS from P3 and P7 after 24h were compared, no significant changes were found (Figure 6 C). In contrast, a significantly higher cell count was obtained in P3 after 72h when compared with P7 after 72h (Figure 6 D). P values are listed in Supplementary Tables S1.

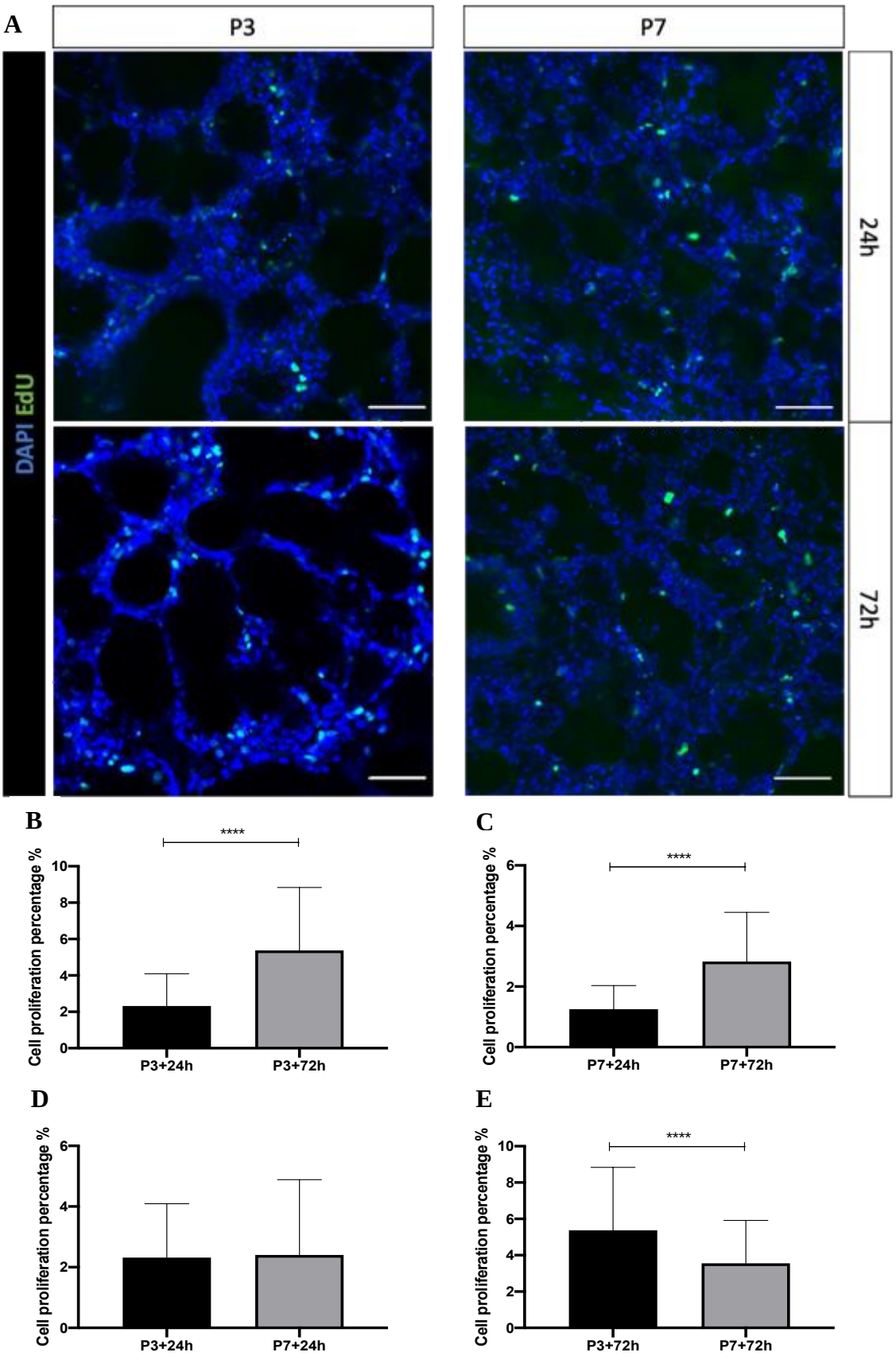

Figure 6. Quantification of cell proliferation in PCLS. Cell proliferation assay was carried out in PCLS from P3 and P7 mice after 24 and 72h in culture (*n* = 9 per time point). (**A)** EdU was labeled with Alexa Fluor 488 (green), nucleus with DAPI (blue). **(B-E)** Quantification of cell proliferation was automatedly counted by FIJI using a cell counting protocol stablished by Shihan et al. 2021. Comparations were performed between PCLS

from P3 (**B)** and P7 **(C)** mice after 24h and 72h in culture, as well as between P3 and P7 PCLS at 24h **(D)** and 72h **(E)** in culture. Student's t-test was performed for each condition and $P < 0.05$ was considered statistically significant. Different letters indicate significant effect. Scale bar: 50 µm

Next, cell viability was analyzed using the same experimental design as for proliferation. Optical density (OD) was significantly lower in P3 PCLS after 24h than after 72h in culture. Lung cells remained viable for up to 72h in culture (Figure 7 A). A similar pattern was observed for PCLS obtained from P7 mice; PCLS remained viable for up to 72h (Figure 7 B). In both scenarios, a slight nonsignificant decrease in cell viability was detected after 72h. P values are listed in Supplementary Tables S2.

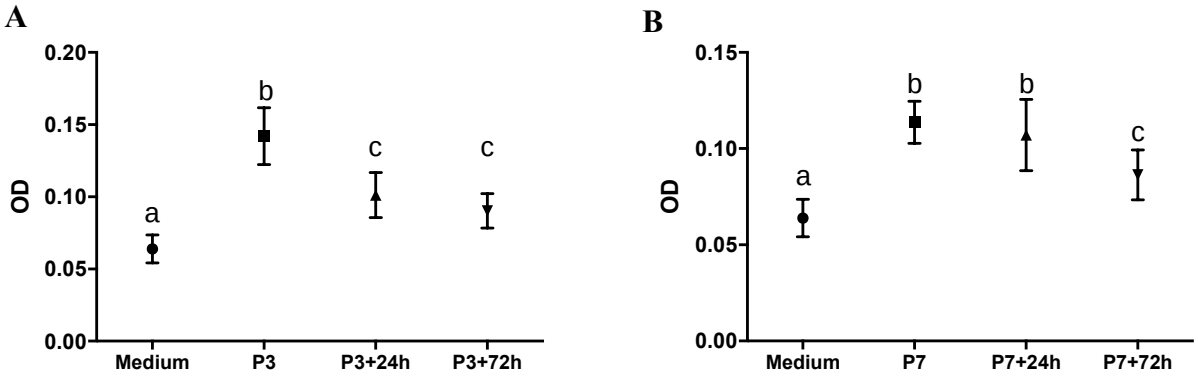

Figure 7. Viability assay performed in PCLS. Viability of PCLS from P3 **(A)** and P7 **(B)** mice was determined by MTT assay at 4, 24, and 72h in culture. Optical density (OD) was measured at a wavelength of 550 nm ($n = 12$ per experiment). One-way ANOVA with post hoc Tukey test was used and $P < 0.05$ was considered statistically significant. Different letters indicate significant effect.

5.3. In vitro PCLS stereological quantification

Subsequently, visualization and quantification of possible lung remodeling was addressed. Previous results indicated that cells within PCLS are actively proliferating and growing. Whether these processes were resulting in noticeable changes in lung structure was the subject of our next analysis. To optimize a quantification of change in lung structure, three approaches were considered: PCLS_P 1, 2 and 3.

5.3.1. Stereology of PCLS using confocal laser scanning images.

The first approach included confocal laser scanning imaging of mTmG mice following the experimental design of sections 5.2, with a slight modification: the addition of an end control at P14. Apparently PCLS from P3 and P7 mice did not morphologically develop when cultured for 24h (Figure 8 A). In contrast, after 72h in culture, morphological similarities to end controls were observed between *in vitro* P7 PCLS

after 72h and P14 control, and, *in vitro* P3 PCLS after 72h and P7 control. However, in order to confirm and quantify this outcome, PCLS were next analyzed by stereology.

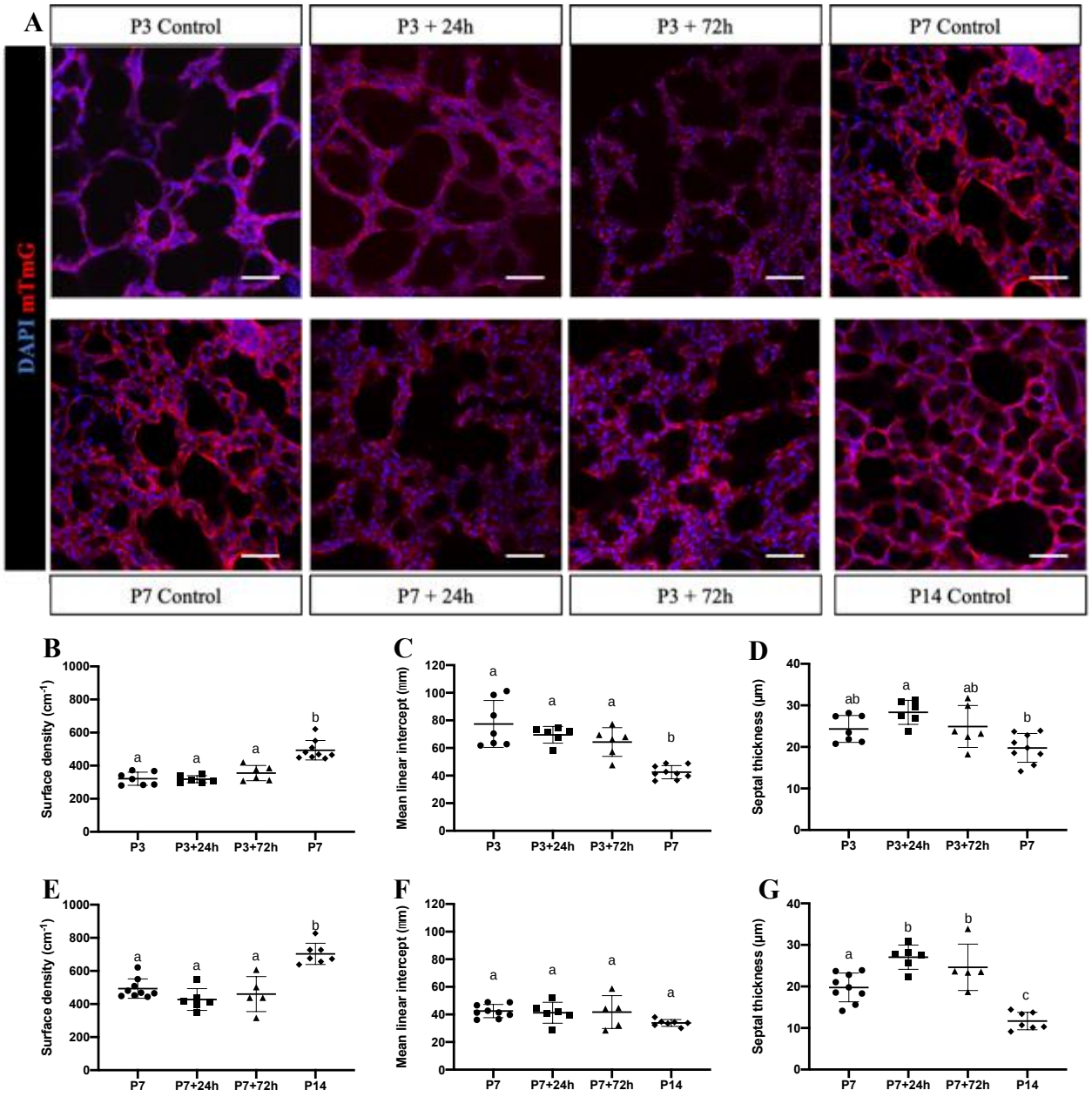

Figure 8. Confocal laser scanning imaging and stereological analysis of mTmG PCLS. (A) Representative images of *in vivo* P3, P7 and P14 PCLS as morphology control and PCLS from P3 and P7 mice after 24 and 72h in culture. Cells from mTmG mice expressed tdTomato fluorescent protein (red) and nuclei were labeled by DAPI (blue). Scale bar: 50 µm. **(B-G)** Stereological quantification of obtained images were analyzed using Visioparhm software. Surface density **(B, E)**, mean linear intercept **(C, F)** and septal thickness **(D, G)**. A comparation between P3 and P7 (**B-D)** *in vivo* with P3 PCLS *in vitro* after 24h and 72h in culture. Comparison between P7 and P14 **(E-G)** *in vivo* with P7 PCLS *in vitro* 24h and 72h (n = 3 per experiment). One-way ANOVA with post hoc Tukey test was used and $P < 0.05$ was considered statistically significant. Different letters indicate significant effect.

Following, stereology counting was performed as illustrated in Figure 8 B–G. In this latter scenario, surface density showed results for P3 control and P7 control, being P7 the highest value. P3 PCLS after 24h and 72h showed similar result to P3 control (Figure 8 B). Similarly, P7 control and P14 control showed significantly differences, being P14 the highest value. I*n vitro* P7 PCLS presented similar values as P7 control for surface density as illustrated in Figure 8 E. On the one hand, MLI showed significant values between both *in vivo* PCLS, but *in vitro* PCLS showing similar values when compared with P3 PCLS controls. On other and, P7 and P14 PCLS controls, as well as *in vitro* P7 PCLS presented similar MLI as illustrated in Figure 8 C, F. Finally, Septal thickness was analyzed and showed P3 PCLS controls not significantly higher than P7 PCLS control but *in vitro* P3 PCLS after 24h showed a significant increased septal thickness compared with P7 PCLS controls, and as illustrated in Figure 8 D. Septal thickness *in vivo* PCLS from P7 mice was significantly increased compared with the end P14 control, but both controls presented smaller values compared with *in vitro* PCLS (Figure 8 G). All measured values are listed in Supplementary Tables S3 and S4.

Nonetheless, due to the background and noise produced at the deepest images when using the Z-stack method obtained by confocal imaging, combined with lack of alveolarization observed after these previous experiments, next steps were carried out in order to develop a different quantification approach. This was addressed in order to study any possible change in structure in PCLS.

5.3.2. Stereology of PCLS using paraffin sections

A second approach to analyze structural changes in PCLS was based on stereology using paraffin embedded sections respectively (Akram et al., 2019a; Pieretti et al., 2014). *In vitro* 300-µm-thick PCLS of P3 mice were evaluated after 72h in culture and 1,000-µm-thick PCLS from P4 mice were cultured for 96h.

Representative images of *in vivo* control lungs for both experimental designs, showed that alveolar size was negatively correlated with the age of the animal for both experiments (Figure 9 A and 10 A). For the first experiment, P3, P7 and P14 controls presented a positively-correlated increased surface density according age of the animal (Figures 9 B). However, *in vitro* PCLS showed significantly lesser values than controls. The second measured parameter MLI, presented significantly decreasing values for older animals, but *in vitro* PCLS presented a different pattern, P3 PCLS cultured for 72h presented similar values than P7 control (Figure 9 C). Next, septal thickness presented a notably increased septal thickness in PCLS *in vitro* compared with all *in vivo* controls.

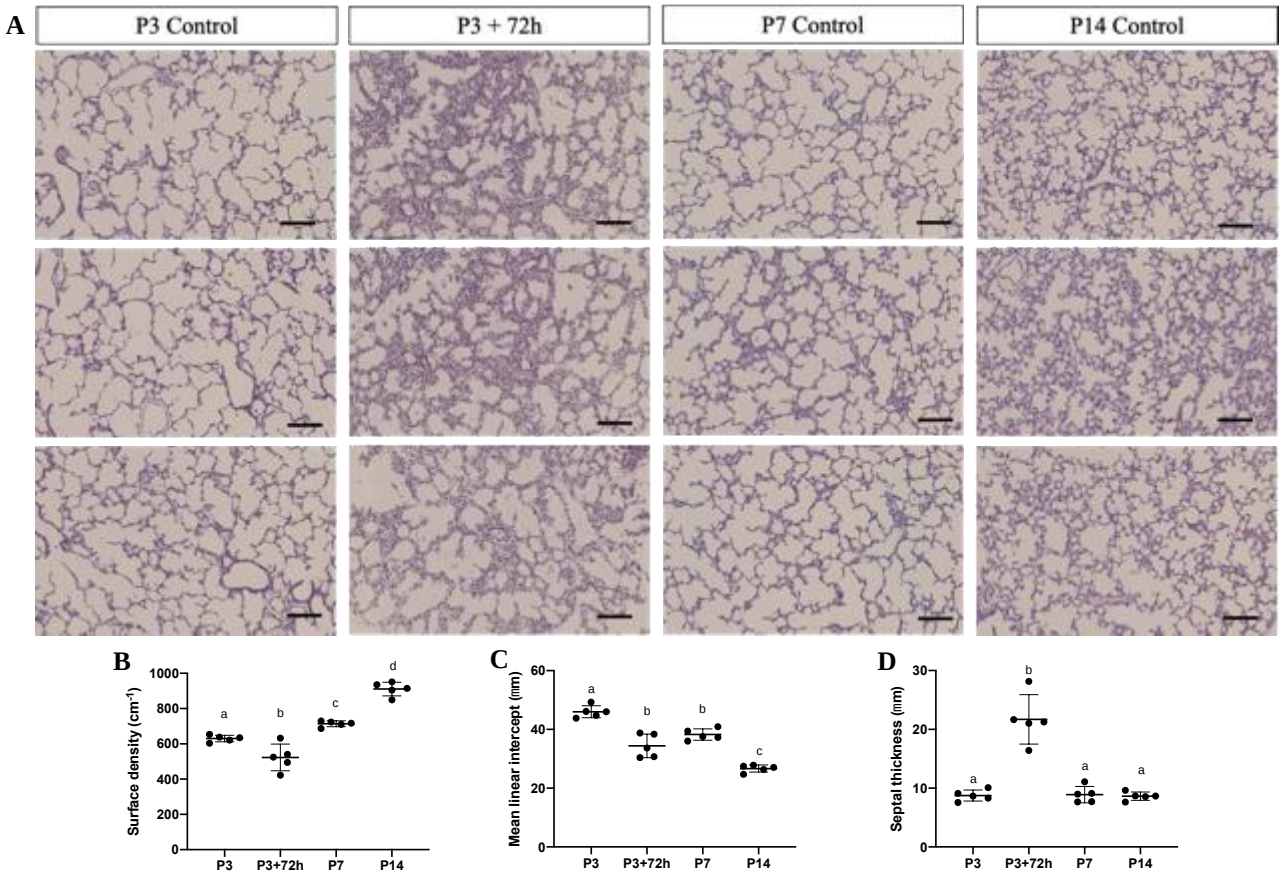

Figure 9. Stereological analysis of 300-µm-thick PCLS in paraffin. (A) Light microscopic imaging from P3, P7 and P14 *in vivo* control PCLS were compared with 300-µm- thick P3 PCLS after 72h in culture. **(B –D)** Four 4-µm slices with 20-µm space between them were stained with H&E. Three representative images were obtained from each group and quantification was performed using Visioparhm software. **(B)** Surface density, **(C)** mean linear intercept and **(D)** septal thickness were analyzed *in vitro* P3 PCLS cultured for 72h and compared with P3, P7 and P14 *in* vivo controls PCLS (n = 5 per experiment). One-way ANOVA with post hoc Tukey test was used and $P < 0.05$ was considered statistically significant. Scale bar: 100 µm. Different letters indicate significant effect.

Next, second protocol mentioned in section 4.2.5 (PCLS_P3) was carry out. Similar tendency was found for surface density *in vivo* controls P4, P8 and P12 showed positively-correlated increased surface density with the age of the animal but significantly lesser value for *in vitro* PCLS (Figure 10 B). Completely different MLI results were obtained. *In vivo* controls presented similar tendency as the MLI of previous results, but P4 *in vitro* PCLS after 96h in culture showed the highest value (Figure 10 C). Finally, septal thickness showed increased value in PCLS *in vitro* compared with all *in vivo* controls (Figure 10 C). All measured values are listed in Supplementary Tables S5 and S6.

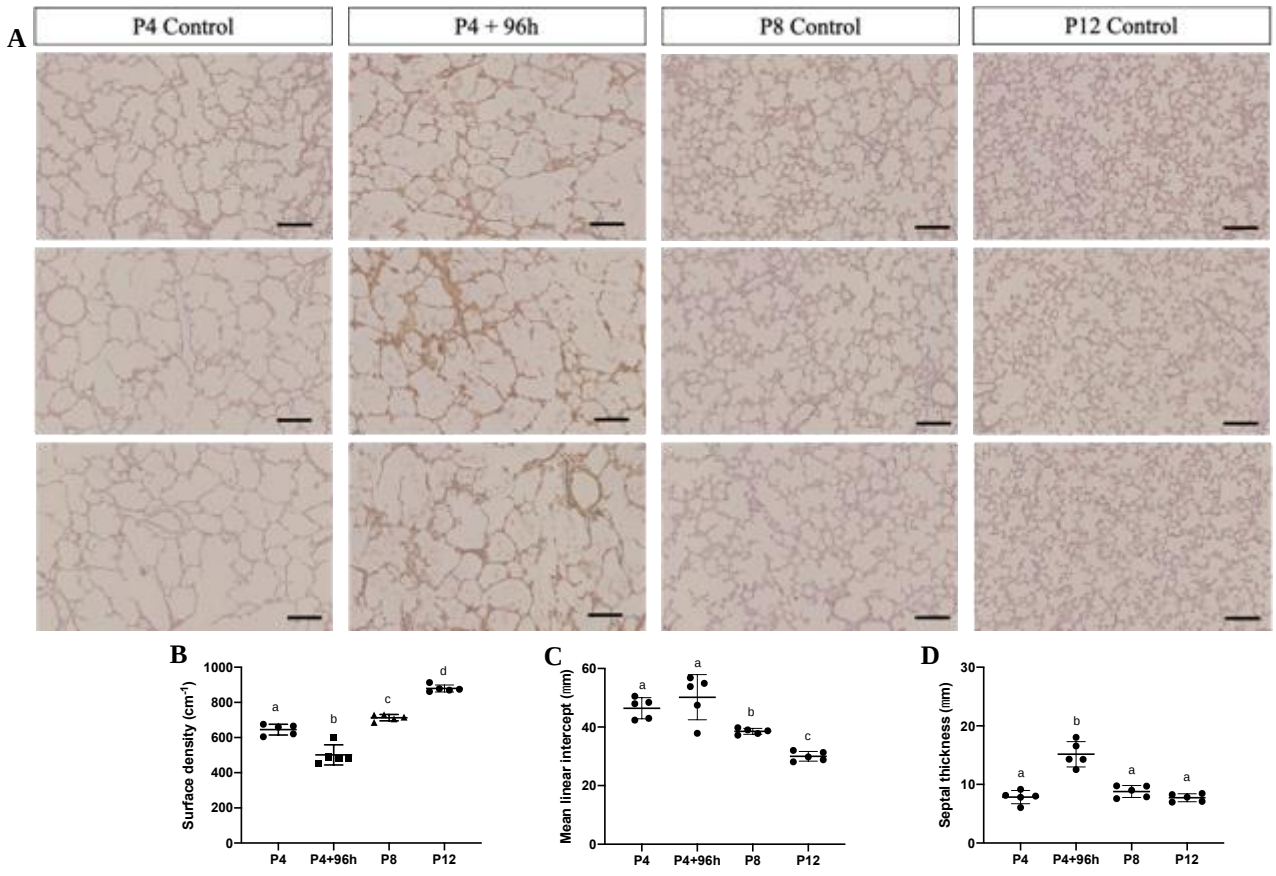

Figure 10. Stereological analysis of 1,000-µm thick PCLS in paraffin. Light microscopic imaging from P4, P8 and P12 control PCLS were compared with 1,000-µm- thick P3 PCLS after 72h in culture. **(B –D)** Four 4-µm slices with 20-µm space between them were stained with elastica staining. Three representative images were obtained from each group and quantification was performed using Visioparhm software. **(B)** Surface density, **(C)** mean linear intercept and **(D)** septal thickness were analyzed *in vitro* P4 PCLS cultured for 96h and compared with P4, P8 and P12 in vivo controls PCLS (n = 5 per experiment). One-way ANOVA with post hoc Tukey test was used and $P < 0.05$ was considered statistically significant. Scale bar: 100 µm. Different letters indicate significant effect.

As similar approaches were carried out from both experimental settings, the outcomes were compared. This was achieved in order to evaluate whether using both experimental settings resulting the same level of accuracy. Represented in Figure 11 A, 300-µm-thick PCLS showed thicker septa than 1,000-µm-thick PLCS and both showed possible differences in the size of the alveoli. These finding were in agreement with results obtained using stereology quantification. In Figure 11 B, both differently cultured PCLS maintained the same surface density, however a higher MLI was shown in 1,000-µm-thick PCLS (Figure 11 C) whereas septa showed to be thicker at 300-µm-thick PCLS compared to 1000-µm-thick PCLS (Figure 11 D). All compared values are listed in Supplementary Tables S7 and S8.

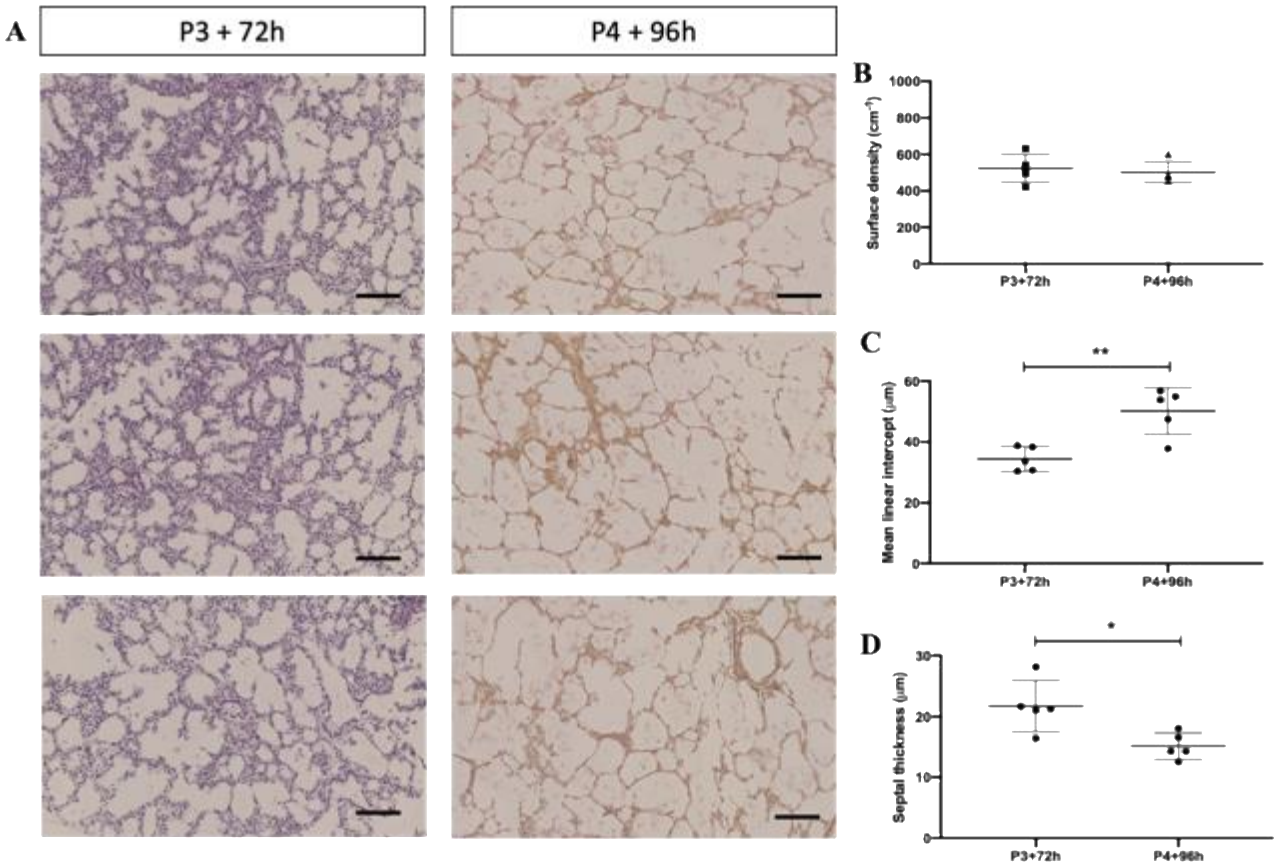

Figure 11. Comparison between *in vitro* 300-µm- and 1,000-µm-thick PCLS embedded in paraffin. **(A)** Display of three representative images of 300-µm-thick and 1,000-µm-thick PCLS. **(B – D)** Four 4-µm slices with 20-µm space between them, were stained with elastica staining. Quantification was performed using Visioparhm software. **(B)** Surface density, **(C)** mean linear intercept and **(D)** septal thickness were analyzed to compare *in vitro* PCLS (n = 5 per experiment). Student's t-test was used and $P < 0.05$ was considered statistically significant. Scale bar: 100 µm.

5.3.3. Stereology of PCLS embedded in glycol methacrylate

Stereology of 300-µm-thick PCLS from P3 mice cultured for 72h using GMA embedding was carried out using *in vivo* P3, P7 and P14 control PCLS. Representative images of *in vivo* control PCLS demonstrated a decrease in size of alveoli towards P14 (Figure 12 A). Surface density increased in *in vivo* control PCLS from P3 to P14. In contrast, surface density of 300-µm-thick P3 PCLS cultured for 72h decreased compared with *in vivo* PCLS (Figure 12 B). Values of MLI *in vivo* PCLS controls decreased from P3 to P7. However, MLI of 300-µm-thick P3 PCLS cultured for 72h decreased compared with P3 *in vivo* PCLS, showing similar value that *in vivo* P7 PCLS (Figure 12C). Septal thickness of GMA embedded *in vitro* control PCLS decreased from P3 to P14, but *in vitro* 300-µm-thick PCLS of P3 mice cultured for 72h demonstrated a strong increase in septal thickness when compared with *in vivo* PCLS controls (Figure 12 D). All measured values are listed in Supplementary Table S7.

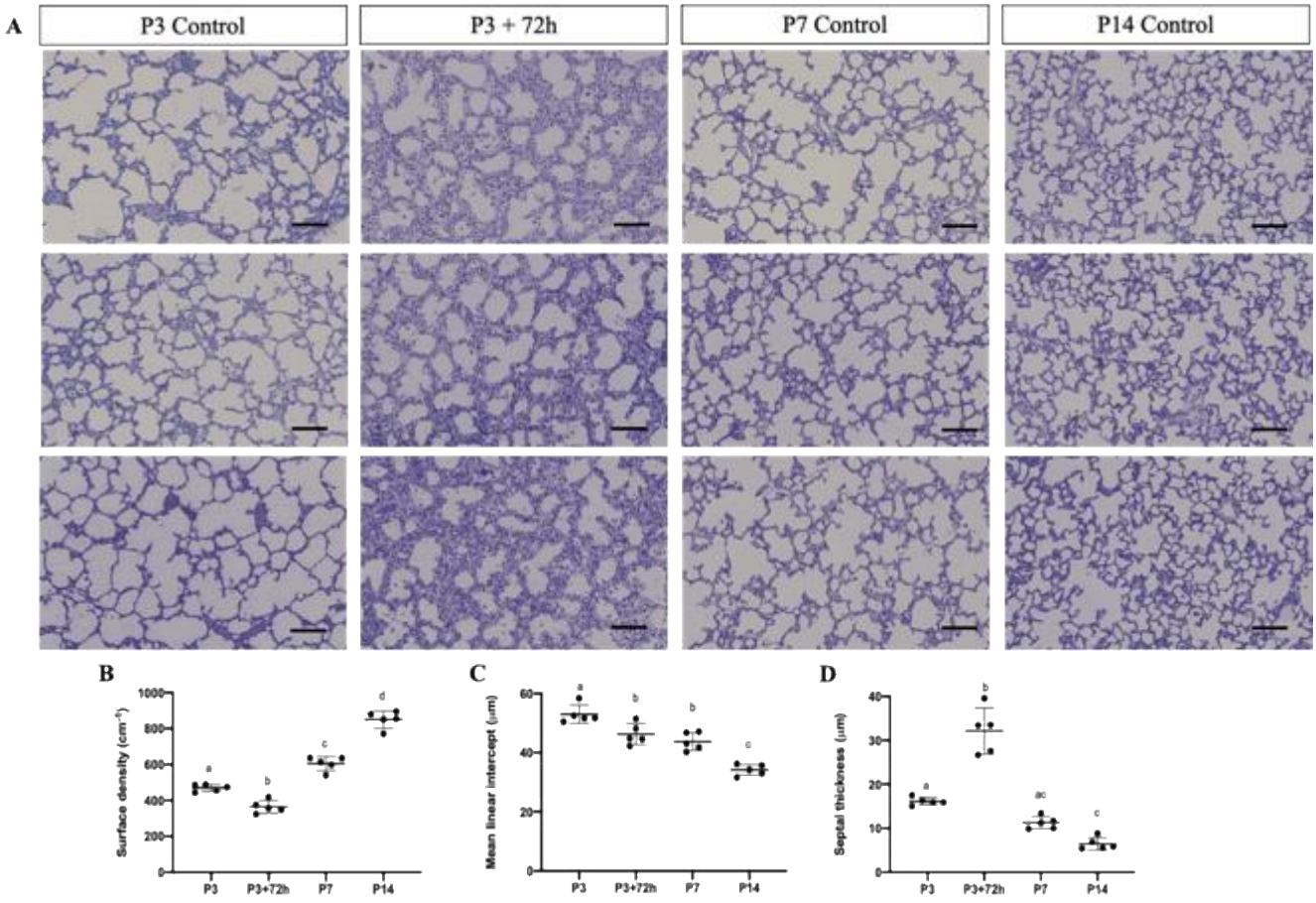

Figure 12. Stereological analysis of 300-µm-thick PCLS embedded in GMA. (A) Light microscopic imaging from P3, P7 and P14 *in vivo* control PCLS were compared with 300-µm- thick P3 PCLS after 72h in culture. **(B – D)** Four 4-µm slices with 20 µm space between them, were stained with Richardson's staining. Quantification was performed using Visioparhm software. **(B)** Surface density, **(C)** mean linear intercept and **(D)** septal thickness (n = 5 per experiment). One-way ANOVA with post hoc Tukey test was used and $P < 0.05$ was considered statistically significant. Scale bar: 100 µm. Different letters indicate significant effect.

Subsequently, the second experiment using GMA embedding included 1,000-µm-thick P4 cultured for 96h PCLS. Experimental design was carried out according to experimental setting used for paraffin embedded sections. *In vivo* grown PCLS controls were taken at P4, P8 and P12. Representative images demonstrated a decrease in size of develop from P4 to P12. *In vitro* grown 1,000-µm-thick P4 PCLS cultured for 96h demonstrated larger alveoli (Figure 13 A). Surface density values of *in vivo* control PCLS increased from P4 to P12, but surface density of *in vitro* P4 PCLS cultured for 96h showed decreased values compared with the *in vivo* controls (Figure 13 B). The second parameter, MLI, presented values of *in vivo* controls decreased from P4 to P12, but *in vitro* 1,000-µm-thick P4 PCLS cultured for 96h showed the highest value (Figure 13 C). Septal thickness of *in vivo* control PCLS showed statistically significance for control P14 when compared with P4 and P8 control. Septal wall thickness of *in vitro*

PCLS showed similar value as P4 and P8 control PCLS (Figure 13 D). All measured values are listed in Supplementary Table S8.

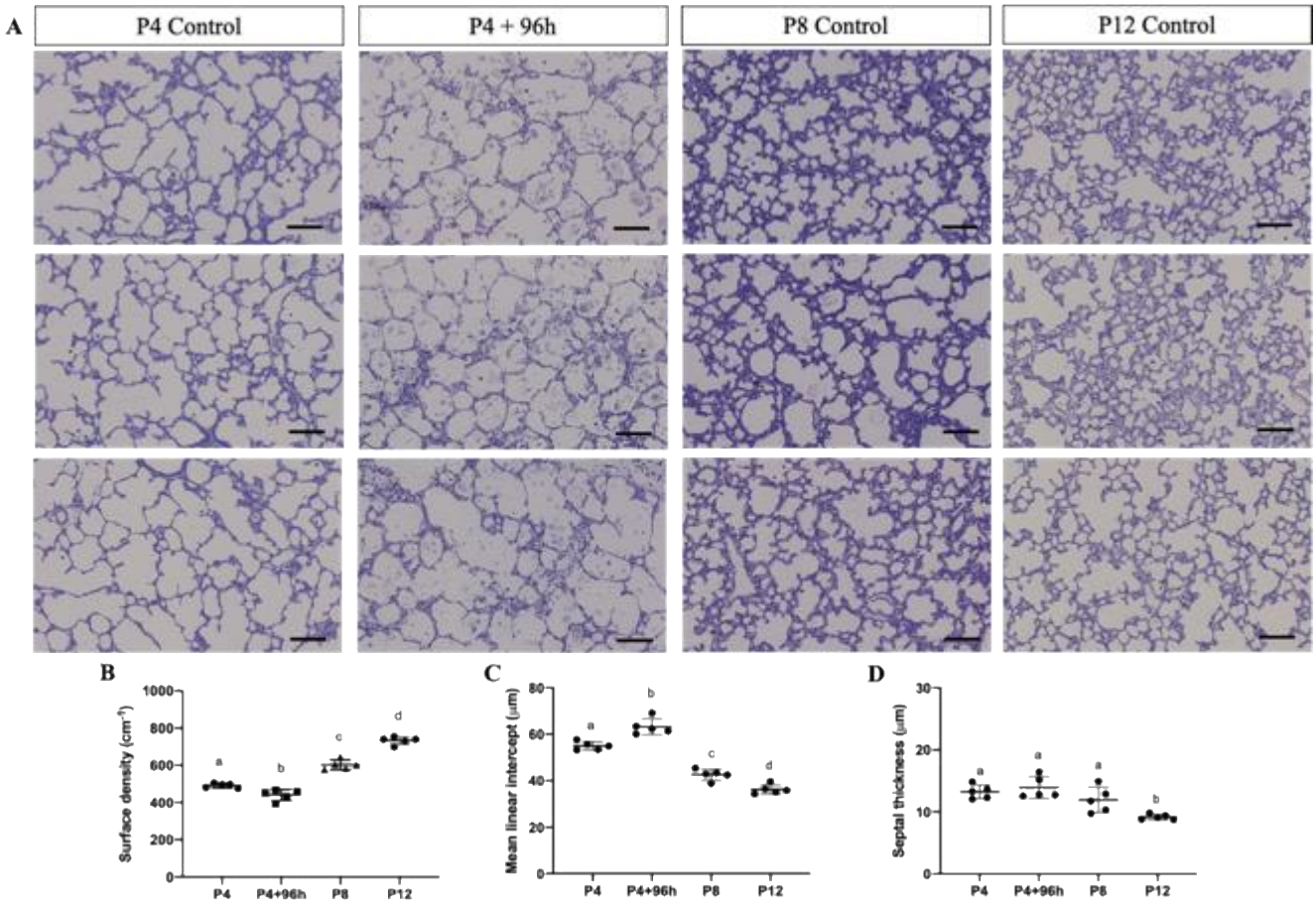

Figure 13. **Stereological analysis of 1000µm thickness PCLS embedded in GMA**. (**A**) Light microscopic imaging from P4, P8 and P12 control PCLS were compared with P4 PCLS after 96h in culture. 4 slices of 2µm and a deep space of 20 µm between them were stained with Richardson´s staining. Three representative images were obtained of each group. B-D. Quantification of stereological parameters were performed using Visioparhm software. Surface density (**B**), Mean linear intercept (**C**) and Septal thickness (**D**). (n = 5 per experiment); $P < 0.05$ determined by one-way ANOVA with post hoc Tukeytest. Scale bar: 100 µm. Different letters indicate significant effect.

In vitro 300-µm-thick P3 PCLS and 1,000-µm-thick P4 PCLS GMA-embedded were compared to analyze the differences between both approaches. As illustrated in Figure 14 A, differences in the structure were displayed at the representative images. Surface density did not differ between the two analyzed conditions (Figure 11 B). Mean linear intercept was significantly higher for 1,000-µm-thick P4 PCLS cultured for 96h compared to 300-µm-thick P3 PCLS cultured for 72h (Figure 14 C). Septal thickness decreased for P3 PCLS cultured for 72h compared with P4 PCLS cultured for 96h (Figure 14 D). All compared values are listed in Supplementary Tables S9 and S10.

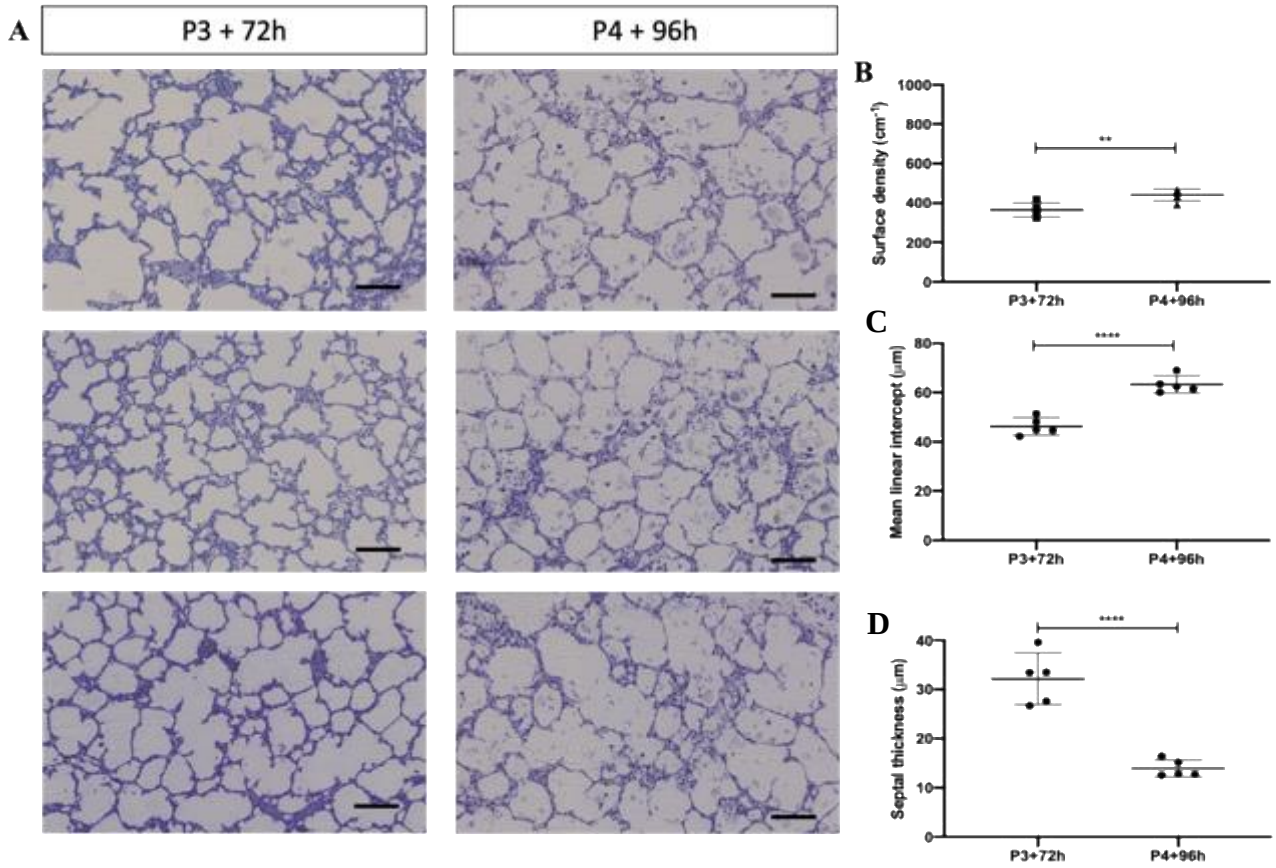

Figure 14. Comparison between *in vitro* P3 PCLS 300-µm- and 1,000-µm-thick P4 PCLS embedded in GMA. **(A)** Three representative images of 300-µm-thick P3 and 1,000-µm-thick P4 PCLS. **(B – D)** Four 4-µm slices with 20-µm space in between were stained with Richardson's staining. Quantification was performed using Visioparhm software. **(B)** Surface density, **(C)** mean linear intercept **(D)** septal thickness (n = 5 per experiment). Student's t-test was used and $P < 0.05$ was considered statistically significant. Scale bar: 100 µm.

5.3.4. Comparation of stereological quantifications using paraffin and GMA embedded tissue

In order to study variations between both techniques using paraffin or GMA respectively, stereological parameters acquired in both techniques were compared.

Surface density decreased significantly in most of the GMA embedded samples when compared to paraffin embedded samples significantly except for 1,000-µm-thick P4 PCLS after 96h in culture and control P14 (Figure 15 A). The second parameter, MLI, presented increased values of the GMA embedded samples compared to paraffin embedded samples, being significant for *in vitro* P3 PCLS after 72h in culture and P4 PCLS after 96h in culture, followed by *in vivo* P3 and P4 controls and, finally, P12 and P14 controls. Nonetheless, for this parameter control groups P7 and P8 did not differed statistically (Figure 15 B). The third and last parameter, septal thickness, showed significantly increased values in GMA embedded *in vitro* P3 PCLS after 72h and *in vivo* P3 and P4 controls. Remaining groups presented similar results for both embedding techniques (Figure 15 C).

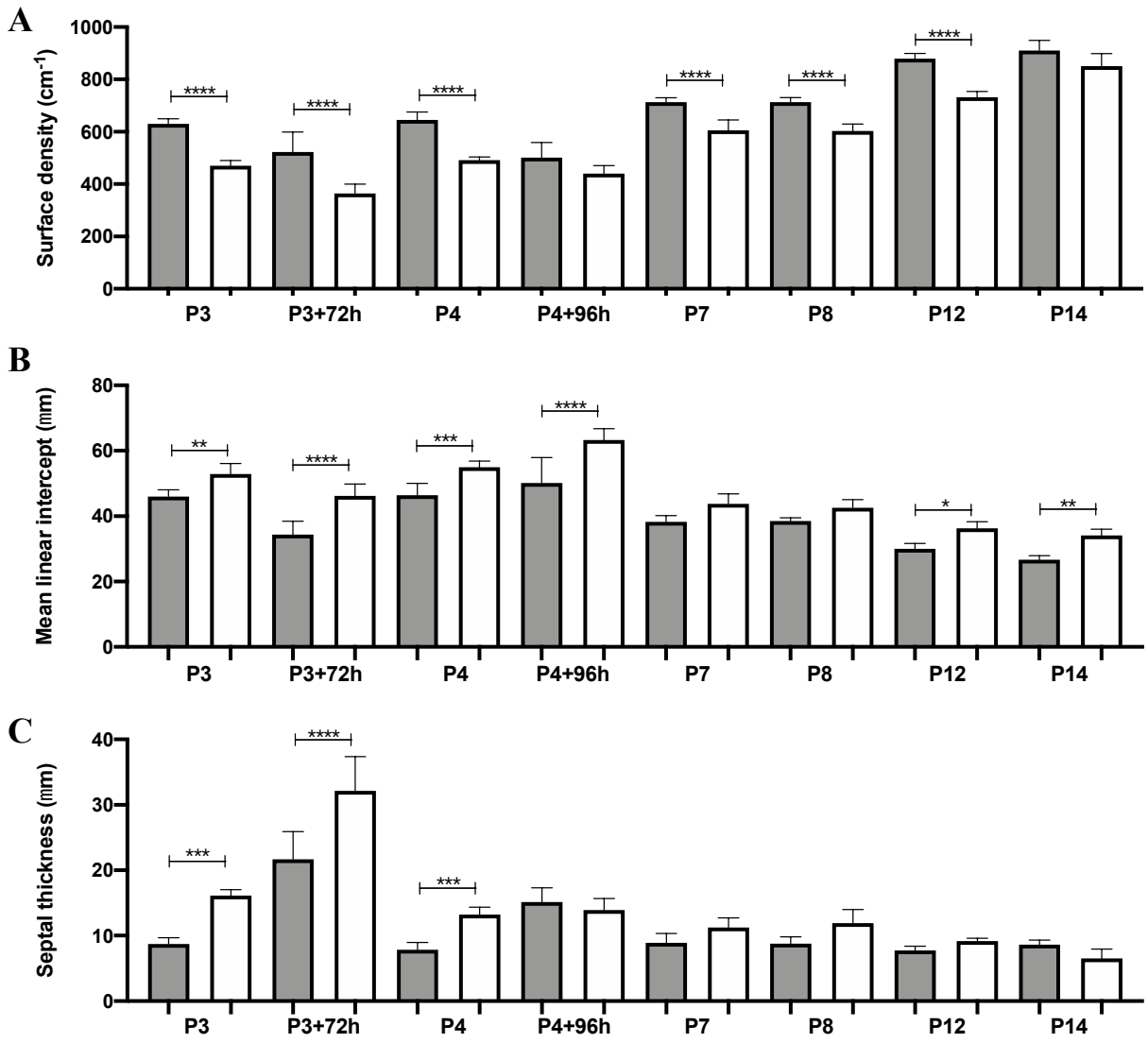

Figure 15. Comparison of stereological parameters using paraffin- and GMA-embedded PCLS from different aged mice. **(A – C)** Four 4-µm slices with 20-µm space in between, were stained and scanned. Paraffin embedded (grey bar) GMA embedded (white bar). Quantification was performed using Visioparhm software. **(A)** Surface density, **(B)** mean linear intercept and **(C)** septal thickness (n = 5 per experiment). Student's t-test was used and $P < 0.05$ was considered statistically significant.

5.4. Quantification of gene expression in postnatal PCLS

After evaluating the results obtained with the previously mentioned quantification, the performance of 300-µm-thick P3 PCLS cultured for 72h was chosen as the most suitable model to study alveolarization. Gene expression of genes impacting on alveolarization was analyzed in postnatal murine PCLS.

Markers for mesenchymal cells were first analyzed. *In vivo* P3 PCLS control showed downregulation of the platelet-derived growth factor receptor α (PDGFRα) compared with *in vivo* P7 and P14. In contrast, *in vitro* P3 PCLS after 72h in culture showed upregulation of this gene compared to *in vivo* PCLS controls (Figure 16 A). Next, the expression of Alpha-smooth muscle actin gene (ACTA2) was analyzed. For this

gene, P14 control PCLS showed downregulation compared with the remaining groups, but *in vitro* P3 PCLS after 72h in culture presented similar expression of this gene compared with P3 and P7 controls PCLS (Figure 16 B). The mesenchymal gene encoding the protein Collagen type I, alpha 1 also known as COL1A1 showed a significant upregulation in *in vivo* PCLS groups compared with *in vitro* P3 PCLS after 72h in culture (Figure 16 C). The gene VIM (encoding the protein Vimentin) showed upregulation in P3 control PCLS compared with P7 and P14 controls PCLS. For the studied *in vitro* P3 PCLS after 72h in cultured no significant differences were found to P3 nor P7 (Figure 16 D).

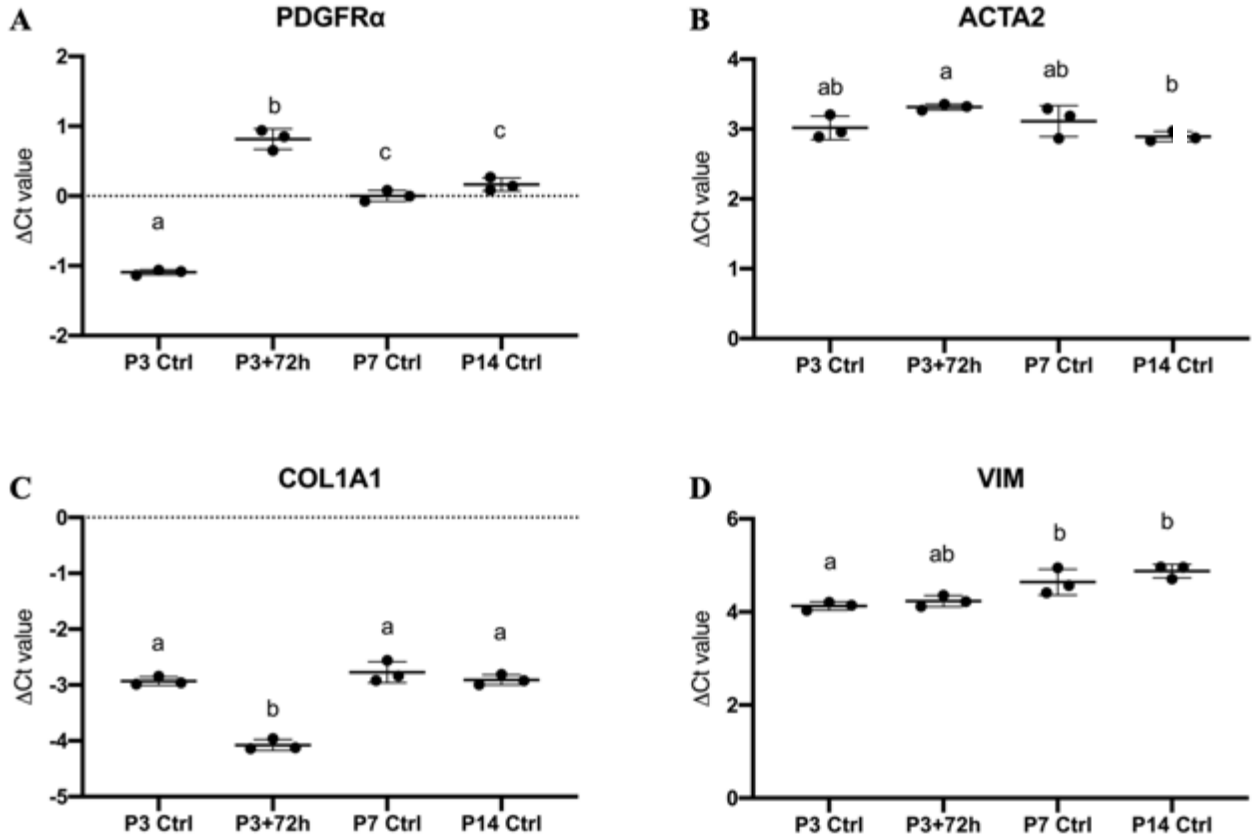

Figure 16. Mesenchymal gene marker expression in cultured P3 PCLS and *in vivo* control PCLS. Gene expression of 300-µm-thick P3 PCLS cultured for 72h and P3, P7 and P14 *in vivo* PCLS. **(A)** PDGFRα, **(B)** ACTA2, **(C)** COL1A1 **(D)** VIM by real-time qPCR. Values are expressed as mean ± Standard Deviation (SD); *n* = 3. Student's t-test was used and $P < 0.05$ was considered statistically significant. Different letters indicate significant effect.

Then, markers for epithelial cells were next analyzed. Podoplanin (PDPN gene) demonstrated a downregulation in P7 control PCLS compared with P3 and P14 controls PCLS. In contrast, *in vitro* P3 PCLS after 72h in culture showed upregulation of PDPN compared with *in vivo* controls PCLS (Figure 17 A). The marker Surfactant-associated protein C (SFTPC gene) was downregulated in P3 control PCLS compared with P7 and P14 control PCLS, but upregulated compared with *in vitro* P3 PCLS after 72h in culture (Figure 17 B). The proliferation marker protein Ki-67 (MKI67 gene) was analyzed next. Expression did not differ from values in control PCLS (Figure 17 D).

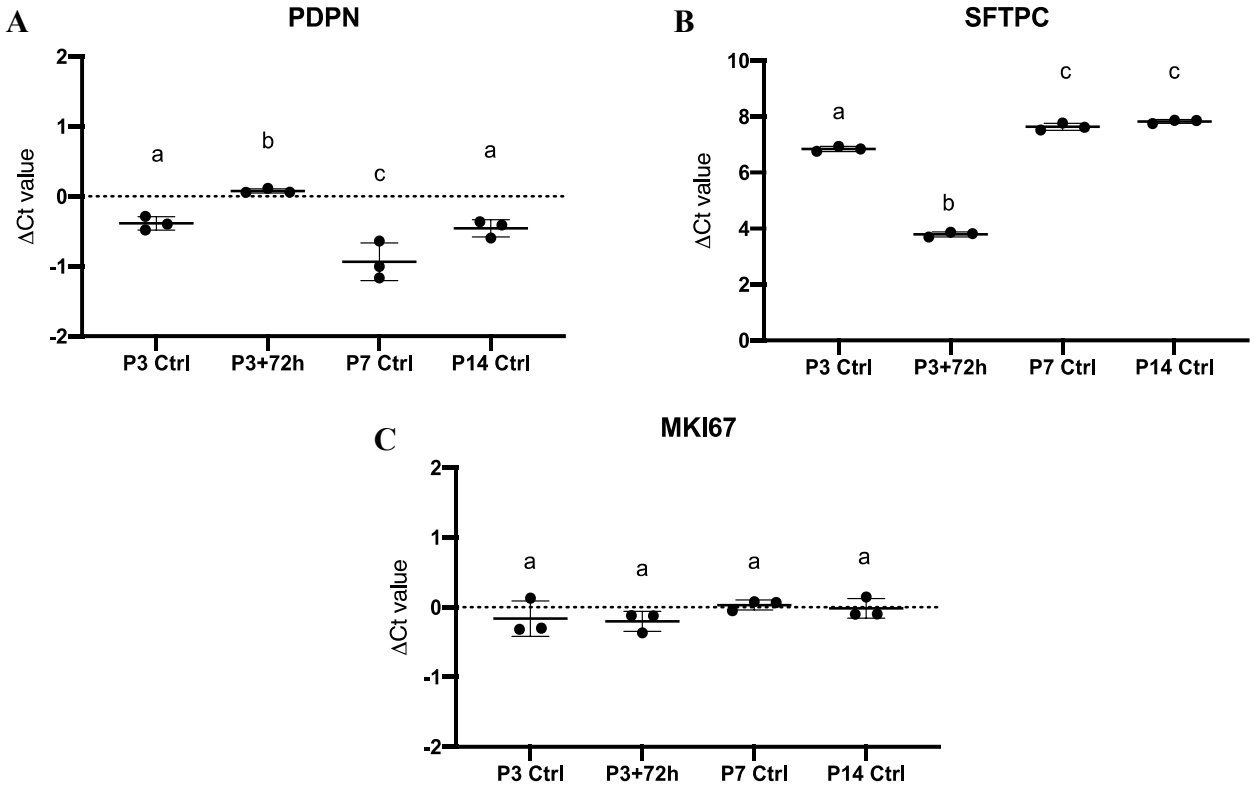

Figure 17. Expression of epithelial and one marker for proliferation in murine P3 cultured PCLS and *in vivo* control PCLS. Gene expression of 300-µm-thick P3 PCLS cultured for 72h and P3, P7 and P14 *in vivo* control PCLS. **(A)** PDPN, **(B)** SFTPC **(C)** MKI67 by real-time qPCR. Values are expressed as mean ± Standard Deviation (SD); $n = 3$. Student's t-test was used and $P < 0.05$ was considered statistically significant. Different letters indicate significant effect.

5.5. Visualization of overexpressed marker by confocal imaging

To corroborate the increment of the cell markers PDPN and PDGFRα, in the postnatal PCLS, visualization of immunostaining and a reporter mouse line were used. A staining assay with anti- PDPN antibody was performed to visualize AECI in the surface of the alveolar septum. Changes in AECI abundance in the alveolar surface of PCLS were observed (Figure 18 top). Reporter mouse line PDGFRαGFP was used to observe PDGFRα + cells in lung tissue from P3 and P7 *in vivo* PCLS and P3 *in vitro* PCLS. An increase in cellular abundance for PDGFRα positive cells was observed for *in vitro* PCLS of postnatal mice (Figure 18 bottom). A higher cellular abundance of PDGFRα positive cells was detected in cultured PCLS compared with the parenchyma of *in vivo* PCLS. Negative control for the PDPN staining is illustrated in Figure S 1.

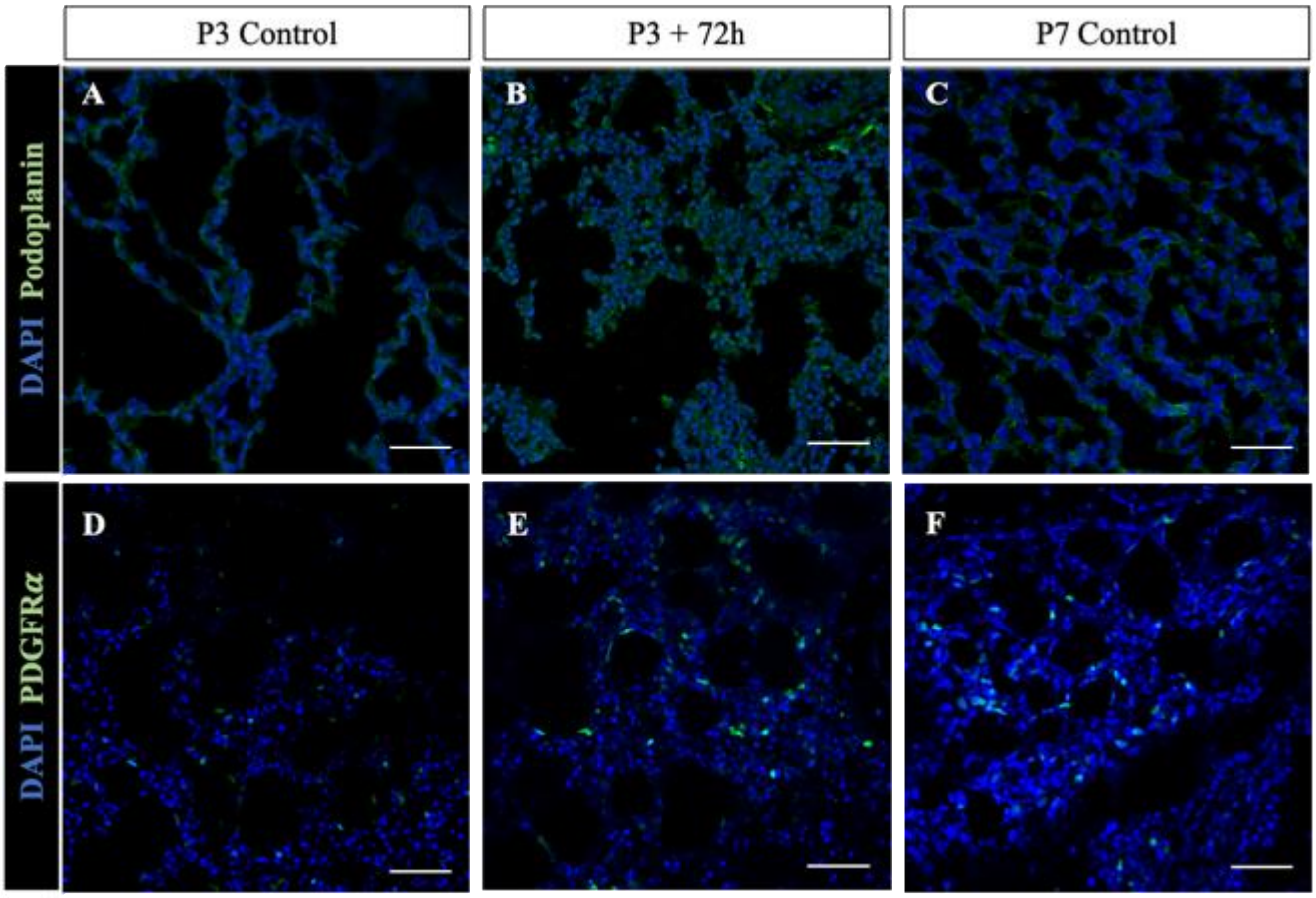

Figure 18. Visualization of Podoplanin and Platelet-derived growth factor receptor α in murine postnatal P3 PCLS cultured for 72h and *in vivo* control P3 and P7 PCLS. (**A – C)** Immunostaining for Podoplanin (green) DAPI (blue). (**D – F)** Visualization of green fluorescence protein (GFP, green) DAPI (blue) in PDGFRα-GFP transgenic mice. Scale bar: 50 µm.

6. Discussion

The present work aimed to validate *in vitro* cultured PCLS of postnatal mice as a tool to study the process of alveolarization. To achieve this aim, PCLS of postnatal wildtype and transgenic postnatal mice were cultured *in vitro.* PCLS of *in vivo* grown postnatal lungs served as a control. Cellular functions such as proliferation and viability were investigated to characterize the PCLS. *In vitro* PCLS from postnatal mice presented abundant cell proliferation compared with the culture of the complete lung. Structural changes in PCLS upon cultivation were assessed using different stereological approaches. Proliferation could be detected in PCLS upon cultivation and cells in PCLS were viable after 72h in culture (Bryson et al., 2020; Hirn et al., 2014; Neuhaus et al., 2017). These results are in line with previously published data. To the author's knowledge, only one other study exists to date that addresses postnatal lung morphological development (Pozarska et al., 2017). The use of confocal laser scanning as a source of high-resolution images is a reliable method to quantify structural changes, although the methodology is not without its difficulties, since noise produced at the deepest images when using the Z-stack method obtained by confocal imaging can sometimes obscure results and make image interpretation more difficult. Hence, modifications to the already available protocol had to be made in order to quantify relevant stereological parameters (Appuhn et al., 2021; Hoang et al., 2018; Pérez-Bravo et al., 2021). Different protocols of previous studies by Akram et al. and Pieretti et al. were followed in order to identify the most reasonable experimental setting to study alveolarization (Akram et al., 2019a; Pieretti et al., 2014). A comparison between paraffin and GMA embedded samples showed that different embedding procedures could significantly alter stereological parameters of PCLS. A significant effect was observed in the structure of *in vitro* postnatal PCLS when compared with the control, using both paraffin and GMA approaches, respectively, hence indicating a different developmental process being undergone by the cultured PCLS. Cell population addressment showed an expression of both epithelial and mesenchymal markers, suggesting that a change in lung structure might be occurring. Taken together, it seems clear that PCLS are a useful tool to study cellular function, but the use of PCLS to study structural changes of alveolarization is not recommended.

Recent studies have shown that culture systems including airway epithelial cells grown as 2D or 3D monolayers allow a differentiated air liquid interface (ALI), where it is possible to culture goblet, club and basal cells, thus allowing us to have a closer look at the *in vitro* lung remodeling process (Bérubé et al., 2010; Bhowmick & Gappa-Fahlenkamp, 2016; Hirn et al., 2014). These trans-well systems allow the development of a polarized epithelium simulating a natural environment that includes "respiratory surfaces" (Balharry et al., 2008; Huang et al., 2013). Although these systems themselves offer a step towards *in vitro* lung culture itself, the lack of air-liquid flow that would otherwise be experienced at the

epithelial and endothelial levels in an *in vivo* setting mean that a full replicate of the *in vivo* lung system is still far from achieved.

The development a more accurate approach using a simpler format was thus needed. Ideally, PCLS compromise a simple tool with a complex intact structure and cellular composition, offering the possibility to investigate multiple regions of the lung (G. Liu et al., 2019). Explants can be cultured from a wide range of donors that can also include healthy and diseased organs. These explants contain all cell types found in the tissue of interest, including any changes of the extracellular matrix associated with the disease of research interest (G. Liu et al., 2019). Therefore, the environment in which PCLS grow has been a matter of intense study. Recreating *in vivo* conditions was not an easy task and culture medium had to be optimized and supplemented with essential nutrients, such as amino acids, glucose, salts, vitamins, and other nutrients (Arora, 2013), enabling the PCLS to remain viable for up to 14 days (Temann et al., 2017). PCLS were cultured in two different media. This change in protocol was motivated by the lack of alveolarization using DMEM/F12 media to culture PCLS and confocal laser scanning microscope imaging. The implication of media composition was not studied into anymore depth, but significantly different results were obtained when supplemented M199 medium and light microscope imaging were used as highlighted in Material and Methods section 4.4.6., which might have provided a richer environment for a wider range of some of the cells present in the PCLS. Hence, culture conditions used in the present study, such as addition of vitamin C as antioxidant or hydrocortisone as a growth and proliferation modulator, might have promoted the growth of some cellular populations, such as fibroblasts (Chepda et al., 2001; Rosner & Cristofalo, 1979). Also, the implications on the variability of results of using different nutrient concentrations has not yet been studied in detail, but it might have had an impact on the slicing and further culture of PCLS, since these variations can change tissue conformation. Future approaches might in be in order to address whether a different agarose concentration might alter the outcome of our manipulations.

The present study aimed to analyze proliferation and viability of the murine postnatal PCLS. Cell proliferation assays are highly important to validate work in experimental settings such a as testing cytotoxicity and drug reagent or analyzing the effect of growth factors on cell activity. DNA synthesis assays have received more attention since they have been shown to be the most accurate method to detect cell proliferation (Romar et al., 2016; Salic & Mitchison, 2008). In the present work, a DNA synthesis assay involving EdU was chosen to analyze PCLS proliferation. Results showed an increase in cell proliferation in postnatal PCLS, after 24h and 72h in culture, showing better results for the P3 PCLS cultured for 72h (5.2.1). Previous studies demonstrated a decrease in proliferation in culture after 72h (Hirn et al., 2014). The latter work was performed in adult rats, where proliferation is expected to be lower than in postnatal mice. Another approach, based on the use of Ki67-antibody staining as a marker

for proliferation, was used by Akram et al. in postnatal mice PCLS, showing approximately 20 % of positive cells after 24h in culture. In the present work, up to 2 % of proliferating cells were measured after 24h of culture (Akram et al., 2019a). The difference in cellular proliferation when compared with Akram et al. might trace back to the fact that EdU labels cells in the S-phase (Buck et al., 2008) and Ki67-antibody is a nuclear protein associated with cellular proliferation during all active phases of the cell cycle (Bruno & Darzynkiewicz, 1992). However, we found evidence confirming clear cell proliferation of murine PCLS for up to 72h of culture.

To combine cell proliferation with viability, an MTT assay was also performed. In this study, the MTT assay was applied at two different postnatal time points, showing decreased cell viability after 24h and 72h in culture compared with the control. When these results were compared with previous studies, viability of cultured PCLS showed decreased viability with increasing length of time in culture (Akram et al., 2019a; Bryson et al., 2020; Lambermont et al., 2014). This variability is mainly due to the use of different animal models for PCLS, such as rats (Martin et al., 1996), guinea pigs (Ressmeyer et al., 2006), or humans (Wohlsen et al., 2003); as well as different techniques to measure cell viability. While some authors used the MTT assay (Akram et al., 2019;Lambermont et al., 2014), others used resazurin-based solutions, such as AlamarBlue (Bryson et al., 2020) or enzymatic reactions such as Lactase Deshydrogenase Activity (Hirn et al., 2014). However, when all results are taken into account, the emergingpattern is in agreement with the results presented in this study. We thus conclude that the results obtained show that PCLS cultured for 72h are most recommended for the purpose of observing some lung remodeling, cellular viability and proliferation (Akram et al., 2019; Lambermont et al., 2014).

The need to use an accurate morphological quantification method to understand lung remodeling has been widely highlighted (Mühlfeld et al., 2015). Because structural quantification is considered the "gold standard" in evaluating experimental intervention, it is imperative that these quantitative methods accurately allow meaningful analysis of results, remain efficient and precise within reasonable efforts, provide the basis for adequate statistical power and can be standardized to facilitate comparisons among experimental groups and even among different studies (Hsia et al., 2010). For these reasons, different stereological approaches were applied in the present study in order to meet optimal quantitative standards. So far, only few studies have used stereology in murine PCLS. As highlighted previously, Akram et al. described morphological mechanisms of alveolarization and Pieretti et al. designed and tested an *in vitro* PCLS culture model that showed PCLS with ongoing secondary septation, cell proliferation, and cell population (Akram et al., 2019a; Pieretti et al., 2014). Additionally, there are only few data demonstrating stereological analyzes in postnatal mice (Pozarska et al., 2017). The latter study also demonstrated stereology using confocal laser scanning microscopy. This imaging technique offers a high optical resolution (Jonkman & Brown, 2015). Previous studies demonstrated quantification of total cell number

in lung sections and stereological parameters using CLSM (Jansing et al., 2018). This stereology approach was applied to quantify stereological parameters in PCLS prepared based on known protocols for culturing PCLS of postnatal mice (PCLS_P 1, 2 and 3).

The first parameter studied was surface density. This parameter represents the area of gas exchange in a volume, given per cm^{-1}. In a lung undergoing natural alveolization, this parameter is expected to present age-related increase since new alveoli are forming and gas exchange area increasing (Hsia et al., 2010). Stereology using CLSM imaging technique showed similar values in *in vitro* P3 PCLS compared with P3 controls, in contrast to lesser values obtained for both paraffin- and GMA-embedded *in vitro* P3 and P4 PCLS samples (Figures 8 B, 9 B, 10B, 12 B and 13B). This outcome, is in contrast with data performed by Pieretti et al. (Pieretti et al., 2014). Increased surface density of P4 PCLS after 96h in the culture compared with control PCLS was demonstrated (Pieretti et al., 2014). Since surface density was not showed in the study of Akram et al. this data could not be compared (Akram et al., 2019a). The second parameter, MLI, gives a of volume to surface ratio of acinar air space and alveoli (Hsia et al., 2010). In contrast to surface density, a negative correlation between age and this parameter is presented in healthy animals (Hsia et al., 2010). This is due to the development and formation of new alveoli which leads to a decrease average size of alveoli and increase in surface of the lung. Also, for this parameter stereology using CLSM imaging values measured in P3 PCLS cultured for 72h were not decreasing compared to P3 *in vivo* control PCLS. However, a different scenario was presented for results obtained from 300-µm-thick PCLS. In this latter scenario, the 300-µm-thick P3 PCLS cultured for 72h showed a decreased MLI value compared with values of *in vivo* P3 control PCLS, being similar to the value obtained for P7 *in vivo* control PCLS, which might indicate a possible structural development, close to what occurs in *in vivo* mice. These results are also in agreement with Akram et al. (Akram et al., 2019). In contrast, 1,000-µm-thick P4 PCLS cultured for 96h showed increased values for MLI in comparison with *in vivo* P4 control PCLS, indicating a possible arrest of the alveolization. The third parameter, septal thickness is the aerometric mean of thickness or air-blood barrier in alveoli (Hsia et al., 2010). This parameter has been demonstrated to follow a negative correlation between age and this parameter during *in vivo* alveolarization (Pozarska et al. 2017). This pattern was clearly present among *in vivo* control PCLS while an increase in septum thickness was clearly seen in stereologies from CLSM images and GMA embedded tissue, but not from paraffin embedded tissue stereology. In contrast, Pieretti et al. demonstrated in 1,000-µm-thick P4 PCLS cultured for 96h a decreased value of septal thickness. According to these data, structural changes of alveolization can occur in postnatal cultured PCLS (Pieretti et al., 2014). Differences obtained in the present study compared to previous studies requires further and more case-specific experiments to better understand differential outcomes (Akram et al., 2019a; Pieretti et al., 2014).

Similar age-related patterns of stereological parameters were obtained in paraffin and GMA embedded samples. However, differences could also be detected using the same experimental design. GMA is a water and ethanol miscible plastic resin, which is favorable for the use of light microscopy, in contrast to paraffin embedding (Schneider & Ochs., 2014). For example, GMA improves histological, morphometrical, and immunohistochemical evaluations, mainly due to the accurate assessment of cytological details (Chiarini-Garcia et al., 2011). Additional evidences showed that paraffin embedding might produce shrink of the tissue. Shrinkage of tissue is caused by tissue dehydration (Schneider & Ochs., 2014). This phenomenon was also present during the present study. *In vivo* control PCLS, as well as cultured PCLS, analyzed at different postnatal time-points were compared using paraffin and GMA embedded samples. Stereological parameters of samples embedded in paraffin differed significantly from values obtained from GMA embedded samples. These results might suggest that GMA embedding could lead to more accurate results related to stereological parameters in cultured PCLS. Stereological parameters of *in vivo* control PCLS of the present study are in agreement with previous data (Pozarska et al., 2017).

Stereology is one of the methods elected to quantify structure changes of the lung during different conditions (Appuhn et al., 2021; Hoang et al., 2018). Also, studies on *in vivo* postnatal mouse lungs were published (Appuhn et al., 2021; Dzhuraev et al., 2019; Hoang et al., 2018; Pérez-Bravo et al., 2021), but only few covers different time points of lung development (Appuhn et al., 2021; Pozarska et al., 2017). Different parameters are established to quantify morphology of lung parenchyma. Analyses of non-volume parameters to lung volume parameters as surface area, airspace volume or septal volume (surface density, MLI or septal thickness multiply by volume of the lung) was discarded due to possible shrinkage of *in vitro* PCLS as it is published in other explant tissue (Dewyse et al., 2021), as well as, the shrinkage of paraffin embedding, or the loss of slices during the process. For this reason, only non-volume dependent parameters were measured. Alveolar density was also not analyzed because a maximum thickness of 3 μm as dissector heights is needed for mouse tissue (Ochs, 2006), being impossible following the morphometrical protocols used of 4-μm- to 5-μm-thick paraffin PCLS sections (Akram et al., 2019a; Pieretti et al., 2014).

Surface density is used to estimate the absolute surface areas of alveoli, which is also linked to the calculation of MLI and septal thickness. MLI is the mean length of line segments on random test line spanning the airspace between intersections of the line with the alveolar surface. Basically, it is an estimator of volume-to-surface ratio of alveoli (Tomkeieff, 1945). Note that MLI and surface density are nearly the same, with one exception: MLI relates to airspaces, whereas surface density includes the volume of interalveolar septal tissue (Hsia et al., 2010). In fibrotic lungs and in previous results, this difference can be significant; the correct measurement of MLI must exclude the volume occupied by the

septa. Septal thickness is the arithmetic mean thickness of air–blood barrier measures alveolar tissue volume per surface area by point and intersection counting (Hsia et al., 2010). These parameters are important to understand the following discussion and comparison between different embedding and imaging techniques used in stereology. However, stereology is perfectly suited to be combined with 3D imaging techniques, such as confocal laser scanning microscopy.

Data demonstrated in the present study have shown that a developmental process was undergoing in *in vitro* cultured PCLS, however, excluding the formation of novel alveoli. In healthy P4 mice, secondary septa appear with higher presence of elastin deposition with an increase of αSMA+ myofibroblasts, among others (Morrisey & Hogan, 2010; Tschanz et al., 2014). As an indirect measurement of this ongoing process in PCLS, RNA expression of mesenchymal cell markers was analyzed. Results demonstrated upregulation of PDGFRα expression in cultured PCLS this was confirmed by CLSM imaging of cellular abundance. Mesenchymal gene makers (ACTA2 or VIM) did not differ from P7 *in vivo* control PCLS to cultured PCLS, which might imply that fibroblast population in cultured PCLS was active like during alveolarization as previously published (Branchfield et al., 2016; Pieretti et al., 2014; Morrisey & Hogan, 2010). The downregulation of COL1A1 in cultured PCLS might indicate cellular dysfunction similar to chronically diseased lungs with bronchopulmonary dysplasia (Mižíková et al., 2015).

Epithelial cell composition during alveolization in terminal bronchioles and alveoli is mostly composed by AECI and AECII, covering up to 98 % of the surface area (Stone et al., 1992). For this reason, RNA expression of expected alveolar epithelial cells was carried out in cultured PCLS. Downregulation of SFTPC and upregulation of PDPN was demonstrated. These results suggest that lack of mechanical forces might impact on the production of surfactant proteins produced by the AECII (Torday & Rehan, 2002). Therefore, the cellular population of AECII might be decreasing. Also, the self-renewal capacity of AECII to replace AECI after injury (Desai et al., 2014), could explain upregulation of Podoplain, confirmed by CLSM imaging of cellular abundance. When these results were compared with the protein expression of Pro-Surfactant C and Aquaporin-5, markers for AECII and AECI, in previous studies (Pieretti et al., 2014), a different scenario was shown. It was demonstrated that Pro-Surfactant C protein expression and staining stayed stable in cultured PCLS while Aquaporin-5 increased. Results might suggested that protein abundance is under more complex genetic control than mRNA abundance (Brion et al., 2020). Finally, Ki67 showed similar expression for *in vivo* control PCLS and *in vitro* cultured PCLS and remained in accordance with previous published data (Akram et al., 2019a; Pieretti et al., 2014). However, measuring protein expression in the presented study would have been favorable in order to better compare generated and previously published data (Akram et al., 2019a; Pieretti et al., 2014).

To study features of progressive and chronic lung diseases, such as, chronic obstructive pulmonary disease (COPD) a progressive inflammatory disease of the airways and idiopathic pulmonary fibrosis (IPF), a chronic and progressive interstitial fibrosis, human and murine cultured PCLS have been shown to be useful (Rosales Gerpe et al., 2018). For example, PCLS from smoke-exposed mice showed increased expression of chemokines when stimulated with a viral mimic or influenza A virus (Bauer et al., 2010). In an *ex vivo* human PCLS model markers of early fibrosis where upregulated when PCLS were expose to a combination of profibrotic growth factors and signaling molecules such as TGF-β1, TNF-α, platelet-derived growth factor-AB, and lysophosphatidic acid (G. Liu et al., 2019). Hence PCLS represented a useful tool to study early-stage IPF and evaluate novel therapies using different treatments (Alsafadi et al., 2017). In terms of cellular composition, PCLS keep a close structural organization to the *in vivo* situation (Bai et al., 2016; Kretschmer et al., 2013). In principle, PCLS can provide the opportunity to correlate cell functions within organ physiology, as demonstrated by complex responses of PCLS to modulation (Temann et al., 2017). As previously mentioned, PCLS have been used as a model to perform toxicological studies, but also to evaluate different lung diseases (Alsafadi et al., 2017; Van Dijk et al., 2016). In asthma studies, comparison between PCLS from healthy and diseased lungs demonstrates an altered response in bronchoconstriction and hyperresponsiveness in PCLS. These responses are similar to those seen in patients and various animal models, suggesting a physiological mimicking in PCLS (Martin et al., 1996; Ressmeyer et al., 2006). Also, PCLS have been used to study innate responses to viral challenge. Use of the PCLS system has allowed a better understanding of which cells are infected in the healthy lung as compared with *in vitro* air liquid interface cell cultures (Goris et al., 2009). Other studies demonstrated that PCLS have been used to monitor effect of LPS on innate immune response, testing the effect of various immunomodulators on innate signaling (Seehase et al., 2012). During the present study, stereological parameters of 300-µm-thick P3 PCLS cultured for 72h have shown to mimic the structural changes expected for IPF because of a decreased surface density and an increased septal thickness (Schneider & Ochs, 2014). Also, stereological parameters of 1,000-µm-thick P4 PCLS cultured 96h might recreate as well features of IPF due to an increase in septal thickness (Mühlfeld & Ochs, 2013). Taken together the present study contributes to a better understanding of advantages and disadvantages of different visualization and embedding techniques using PCLS for different purposes. Accordingly, none of the studied approaches proved to be suitable to study structural changes of alveolarization. However, PCLS proved to be viable up to 72h and acceptable of proliferation and this can be used to study cellular functions. Due to the structural changes upon culture, diseases such as COPD or fibrosis can be mimicked in PCLS. Then, PCLS might represent a suitable tool to study features of pulmonary structural diseases (Jin et al., 2012).

Conclusion

In summary, the present study demonstrated convincing evidence that murine postnatal lung PCLS in culture mice represent a useful tool to study cellular functions up to 72h. Data collected suggest that PCLS can be used to study features of pulmonary diseases.

Stereological analyses demonstrate that alveolar septation, a key process of alveolization, did not take place in cultured PCLS. However, results from *in vitro* cultured PCLS suggested that fibroblasts might represent an active cell type in cultured PCLS. Additional modulation strategies could prove this hypothesis. Future studies on how PCLS can be used to mimic IPF or emphysema will be useful. Finally, the usage of human lung PCLS might contribute to translational medicine. Currently, conflicting outcomes between different studies, as discussed in the present study, lead to controversial conclusion. The present study aimed to contribute to a better understanding of the usage of different PCLS models. Finally, usage of GMA embedding of lung tissue has been identified in the present study to be most suitable to perform stereological analyses. Nevertheless, future identification of favorable medium composition and agarose concentration between rodent and human lung PCLS will support the use of novel approaches to study features of pulmonary structural diseases.

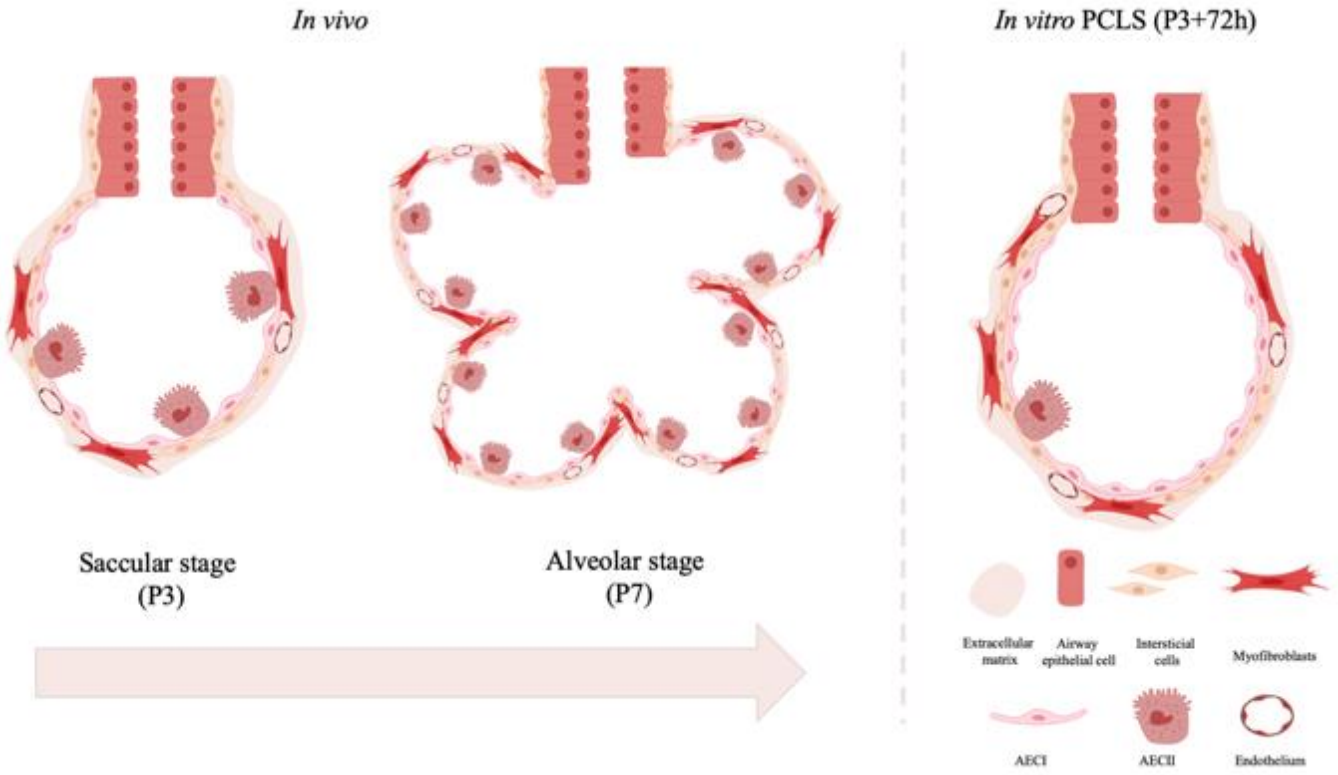

Figure 19. Alveolar structure and cell population during *in vitro* culture of PCLS. *In vivo*, lungs undergo alveolization. New alveoli are formed during the end of the saccular stage (P3) and further developed during the alveolar stage (P7). Alveoli are mainly composed by AECI and AECII combined with interstitial cells such as, myofibroblasts. However, *in vitro* PCLS did not show alveolarization, but an increase in AECI marker expression and decrease in AECII marker expression. Notably, interstitial cell marker expression increased. Figure composed by Bio Render.

7. References

Akram, K. M., Yates, L. L., Mongey, R., Rothery, S., Gaboriau, D. C. A., Sanderson, J., Hind, M., Griffiths, M., & Dean, C. H. (2019a). Live imaging of alveologenesis in precision-cut lung slices reveals dynamic epithelial cell behaviour. *Nature Communications*, *10*(1178). https://doi.org/10.1038/s41467-019-09067-3

Akram, K. M., Yates, L. L., Mongey, R., Rothery, S., Gaboriau, D. C. A., Sanderson, J., Hind, M., Griffiths, M., & Dean, C. H. (2019b). Time-lapse Imaging of Alveologenesis in Mouse Precision-cut Lung Slices. *Bio-Protocol*, *9*(20), e3403. https://doi.org/10.21769/BioProtoc.3403

Alsafadi, H. N., Staab-Weijnitz, C. A., Lehmann, M., Lindner, M., Peschel, B., Königshoff, M., & Wagner, D. E. (2017). An ex vivo model to induce early fibrosis-like changes in human precision-cut lung slices. *American Journal of Physiology-Lung Cellular and Molecular Physiology*, *312*(6), L896–L902. https://doi.org/10.1152/ajplung.00084.2017

Amador, C., Weber, C., & Varacallo, M. (2021). Anatomy, Thorax, Bronchial. *StatPearls*. https://www.statpearls.com/articlelibrary/viewarticle/30998/

Andrae, J., Gouveia, L., He, L., & Betsholtz, C. (2014). Characterization of platelet-derived growth factor-A expression in mouse tissues using a lacZ knock-in approach. *PloS One*, *9*(8), e105477. https://doi.org/10.1371/journal.pone.0105477

Appuhn, S. V., Siebert, S., Myti, D., Wrede, C., Surate Solaligue, D. E., Pérez-Bravo, D., Brandenberger, C., Schipke, J., Morty, R. E., Grothausmann, R., & Mühlfeld, C. (2021). Capillary Changes Precede Disordered Alveolarization in a Mouse Model of Bronchopulmonary Dysplasia. *American Journal of Respiratory Cell and Molecular Biology*, *65*(1), 81–91. https://doi.org/10.1165/rcmb.2021-0004OC

Arora, M. (2013). Cell Culture Media: A Review. *Materials and Methods*, *3*(175). https://.doi.org/10.13070/mm.en.3.175

Atkinson, J. J., Adair-Kirk, T. L., Kelley, D. G., deMello, D., & Senior, R. M. (2008). Clara cell adhesion and migration to extracellular matrix. *Respiratory Research*, *9*(1), 1. https://doi.org/10.1186/1465-9921-9-1

Bai, Y., Krishnamoorthy, N., Patel, K. R., Rosas, I., Sanderson, M. J., & Ai, X. (2016). Cryopreserved Human Precision-Cut Lung Slices as a Bioassay for Live Tissue Banking. A Viability Study of Bronchodilation with Bitter-Taste Receptor Agonists. *American Journal of Respiratory Cell and Molecular Biology*, *54*(5), 656–663. https://doi.org/10.1165/rcmb.2015-0290MA

Balharry, D., Sexton, K., & BéruBé, K. A. (2008). An in vitro approach to assess the toxicity of inhaled tobacco smoke components: Nicotine, cadmium, formaldehyde and urethane. *Toxicology*, *244*(1), 66–76. https://doi.org/10.1016/j.tox.2007.11.001

Bauer, C. M., Zavitz, C. C., Botelho, F. M., Lambert, K. N., Brown, E. G., Mossman, K. L., ... & Stämpfli, M. R. (2010). Treating viral exacerbations of chronic obstructive pulmonary disease: insights from a mouse model of cigarette smoke and H1N1 influenza infection. *PloS one*, *5*(10), e13251. https://doi.org/10.1371/journal.pone.0013251

Barkauskas, C. E., Cronce, M. J., Rackley, C. R., Bowie, E. J., Keene, D. R., Stripp, B. R., Randell, S. H., Noble, P. W., & Hogan, B. L. M. (2013). Type 2 alveolar cells are stem cells in adult lung. *The Journal of Clinical Investigation*, *123*(7), 3025–3036. https://doi.org/10.1172/JCI68782

Barth, K., Bläsche, R., & Kasper, M. (2010). T1alpha/podoplanin shows raft-associated distribution in mouse lung alveolar epithelial E10 cells. *Cellular Physiology and Biochemistry: International Journal of Experimental Cellular Physiology, Biochemistry, and Pharmacology*, *25*(1), 103–112. https://doi.org/10.1159/000272065

Bérubé, K., Prytherch, Z., Job, C., & Hughes, T. (2010). Human primary bronchial lung cell constructs: The new respiratory models. *Toxicology*, *278*(3), 311–318. https://doi.org/10.1016/j.tox.2010.04.004

Bhowmick, R., & Gappa-Fahlenkamp, H. (2016). Cells and Culture Systems Used to Model the Small Airway Epithelium. *Lung*, *194*(3), 419–428. https://doi.org/10.1007/s00408-016-9875-2

Bohn, D., Tamura, M., Perrin, D., Barker, G., & Rabinovitch, M. (1987). Ventilatory predictors of pulmonary hypoplasia in congenital diaphragmatic hernia, confirmed by morphologic assessment. *The Journal of Pediatrics*, *111*(3), 423–431. https://doi.org/10.1016/s0022-3476(87)80474-2

Boström, H., Gritli-Linde, A., & Betsholtz, C. (2002). PDGF-A/PDGF alpha-receptor signaling is required for lung growth and the formation of alveoli but not for early lung branching morphogenesis. *Developmental Dynamics: An Official Publication of the American Association of Anatomists*, *223*(1), 155–162. https://doi.org/10.1002/dvdy.1225

Boström, H., Willetts, K., Pekny, M., Levéen, P., Lindahl, P., Hedstrand, H., Pekna, M., Hellström, M., Gebre-Medhin, S., Schalling, M., Nilsson, M., Kurland, S., Törnell, J., Heath, J. K., & Betsholtz, C. (1996). PDGF-A signaling is a critical event in lung alveolar myofibroblast development and alveogenesis. *Cell*, *85*(6), 863–873. https://doi.org/10.1016/s0092-8674(00)81270-2

Bourbon, J., Boucherat, O., Chailley-Heu, B., & Delacourt, C. (2005). Control mechanisms of lung alveolar development and their disorders in bronchopulmonary dysplasia. *Pediatric Research*, *57*(5 Pt 2), 38R-46R. https://doi.org/10.1203/01.PDR.0000159630.35883.BE

Branchfield, K., Li, R., Lungova, V., Verheyden, J. M., McCulley, D., & Sun, X. (2016). A three-dimensional study of alveologenesis in mouse lung. *Developmental Biology*, *409*(2), 429–441. https://doi.org/10.1016/j.ydbio.2015.11.017

Brion, C., Lutz, S. M., & Albert, F. W. (2020). Simultaneous quantification of mRNA and protein in single cells reveals post-transcriptional effects of genetic variation. *Elife*, *9*, e60645. https://doi.org/10.7554/eLife.60645

Bruno, S., & Darzynkiewicz, Z. (1992). Cell cycle dependent expression and stability of the nuclear protein detected by Ki-67 antibody in HL-60 cells. *Cell Proliferation*, *25*(1), 31–40. https://doi.org/10.1111/j.1365-2184.1992.tb01435.x

Brusasco, V., & Dinh-Xuan, A. T. (2010). Stereology: a bridge to a better understanding of lung structure and function. *European Respiratory Journal*, *35*(3), 477–478. https://doi.org/10.1183/09031936.00005710

Bryson, K. J., Garrido, D., Esposito, M., McLachlan, G., Digard, P., Schouler, C., Guabiraba, R., Trapp, S., & Vervelde, L. (2020). Precision cut lung slices: A novel versatile tool to examine host–pathogen interaction in the chicken lung. *Veterinary Research*, *51*(2). https://doi.org/doi.org/10.1186/s13567-019-0733-0

Rosner, B. A., & Cristofalo, V. J. (1979). Hydrocortisone: a specific modulator of in vitro cell proliferation and aging. *Mechanisms of ageing and development*, *9*(5-6), 485-496. https://doi.org/10.1016/0047-6374(79)90089-7

Buck, S. B., Bradford, J., Gee, K. R., Agnew, B. J., Clarke, S. T., & Salic, A. (2008). Detection of S-phase cell cycle progression using 5-ethynyl-2'-deoxyuridine incorporation with click chemistry, an alternative to using 5-bromo-2'-deoxyuridine antibodies. *BioTechniques*, *44*(7), 927–929. https://doi.org/10.2144/000112812

Buffon, G. L. (1777). Essai d'Arithmétique Morale. *Supplement à l'Historie Naturelle*. vol, 4, 1777.

Burri, P. H. (1984). Fetal and postnatal development of the lung. *Annual Review of Physiology*, *46*, 617–628. https://doi.org/10.1146/annurev.ph.46.030184.003153

Burri, P. H., Dbaly, J., & Weibel, E. R. (1974). The postnatal growth of the rat lung. I. Morphometry. *The Anatomical Record*, *178*(4), 711-730. https://doi.org/10.1002/ar.1091780405

Caduff, J. H., Fischer, L. C., & Burri, P. H. (1986). Scanning electron microscope study of the developing microvasculature in the postnatal rat lung. *The Anatomical Record*, *216*(2), 154-164. https://doi.org/10.1002/ar.1092160207

Chao, C.-M., El Agha, E., Tiozzo, C., Minoo, P., & Bellusci, S. (2015). A breath of fresh air on the mesenchyme: Impact of impaired mesenchymal development on the pathogenesis of bronchopulmonary dysplasia. *Frontiers in Medicine*, *2*, 27. https://doi.org/10.3389/fmed.2015.00027

Chehrehasa, F., Meedeniya, A. C. B., Dwyer, P., Abrahamsen, G., & Mackay-Sim, A. (2009). EdU, a new thymidine analogue for labelling proliferating cells in the nervous system. *Journal of Neuroscience Methods*, *177*(1), 122–130. https://doi.org/10.1016/j.jneumeth.2008.10.006

Chepda, T., Cadau, M., Girin, P. H., Frey, J., & Chamson, A. (2001). Monitoring of ascorbate at a constant rate in cell culture: effect on cell growth. *In Vitro Cellular & Developmental Biology-Animal, 37*(1), 26-30. https://doi.org/10.1290/1071-2690(2001)037<0026:MOAAAC>2.0.CO;2

Chiarini-Garcia, H., Parreira, G. G., & Almeida, F. R. C. L. (2011). Glycol methacrylate embedding for improved morphological, morphometrical, and immunohistochemical investigations under light microscopy: Testes as a model. *Methods in Molecular Biology (Clifton, N.J.)*, *689*, 3–18. https://doi.org/10.1007/978-1-60761-950-5_1

Chu, A. C., Smith, N., & Macdonald, D. M. (1980). Evaluation of staining methods for resin embedded cutaneous tissue sections of mycosis fungoides. *British Journal of Dermatology*, *103*(6), 607–614. https://doi.org/10.1111/j.1365-2133.1980.tb01682.x

Desai, T. J., Brownfield, D. G., & Krasnow, M. A. (2014). Alveolar progenitor and stem cells in lung development, renewal and cancer. *Nature*, *507*(7491), 190–194. https://doi.org/10.1038/nature12930

Dewyse, L., Reynaert, H., & van Grunsven, L. A. (2021). Best Practices and Progress in Precision-Cut Liver Slice Cultures. *International Journal of Molecular Sciences*, *22*(13), 7137. https://doi.org/10.3390/ijms22137137

Dobbs, L. G., & Johnson, M. D. (2007). Alveolar epithelial transport in the adult lung. *Respiratory Physiology & Neurobiology*, *159*(3), 283–300. https://doi.org/10.1016/j.resp.2007.06.011

Dzhuraev, G., Rodríguez-Castillo, J. A., Ruiz-Camp, J., Salwig, I., Szibor, M., Vadasz, I., Herold, S., Braun, T., Ahlbrecht, K., & Atzberger, A. (2019). Estimation of absolute number of alveolar epithelial type 2 cells in mouse lungs: A comparison between stereology and flow cytometry. *Journal of Microscopy*, *275*(1), 36–50. https://doi.org/10.1111/jmi.12800

Fu, J., Gerhardt, H., McDaniel, J. M., Xia, B., Liu, X., Ivanciu, L., Ny, A., Hermans, K., Silasi-Mansat, R., McGee, S., Nye, E., Ju, T., Ramirez, M. I., Carmeliet, P., Cummings, R. D., Lupu, F., & Xia, L. (2008). Endothelial cell O-glycan deficiency causes blood/lymphatic misconnections and consequent fatty liver disease in mice. *The Journal of Clinical Investigation*, *118*(11), 3725–3737. https://doi.org/10.1172/JCI36077

Howe, K. L., Achuthan, P., Allen, J., Allen, J., Alvarez-Jarreta, J., Amode, M. R., ... & Flicek, P. (2021). Ensembl 2021. *Nucleic acids research*, *49*(D1), D884-D891. https://doi.org/10.1093/nar/gkaa942

Gerlier, D., & Thomasset, N. (1986). Use of MTT colorimetric assay to measure cell activation. *Journal of Immunological Methods*, *94*(1), 57–63. https://doi.org/10.1016/0022-1759(86)90215-2

Goris, K., Uhlenbruck, S., Schwegmann-Wessels, C., Köhl, W., Niedorf, F., Stern, M., Hewicker-Trautwein, M., Bals, R., Taylor, G., Braun, A., Bicker, G., Kietzmann, M., & Herrler, G. (2009). Differential sensitivity of differentiated epithelial cells to respiratory viruses reveals different viral strategies of host infection. *Journal of Virology*, *83*(4), 1962–1968. https://doi.org/10.1128/JVI.01271-08

Gouveia, L., Betsholtz, C., & Andrae, J. (2017). Expression analysis of platelet-derived growth factor receptor alpha and its ligands in the developing mouse lung. *Physiological Reports*, *5*(6), e13092. https://doi.org/10.14814/phy2.13092

Gross, I., Smith, G. J., Maniscalco, W. M., Czajka, M. R., Wilson, C. M., & Rooney, S. A. (1978). An organ culture model for study of biochemical development of fetal rat lung. *Journal of Applied Physiology: Respiratory, Environmental and Exercise Physiology*, *45*(3), 355–362. https://doi.org/10.1152/jappl.1978.45.3.355

Hachenberg, T., & Rettig, R. (1998). Stress failure of the blood-gas barrier. *Current Opinion in Anaesthesiology*, *11*(1), 37–44. https://doi.org/10.1097/00001503-199802000-00007

Hall, J. E., & Hall, Mi. E. (2021). *Guyton and Hall textbook of medical physiology.* (14th ed.). Elservier.

Hamilton, T. G., Klinghoffer, R. A., Corrin, P. D., & Soriano, P. (2003). Evolutionary divergence of platelet-derived growth factor alpha receptor signaling mechanisms. *Molecular and Cellular Biology*, *23*(11), 4013–4025. https://doi.org/10.1128/MCB.23.11.4013-4025.2003

Herring, M. J., Putney, L. F., Wyatt, G., Finkbeiner, W. E., & Hyde, D. M. (2014). Growth of alveoli during postnatal development in humans based on stereological estimation. *American Journal of Physiology-Lung Cellular and Molecular Physiology*, *307*(4), L338-L344. https://doi.org/10.1152/ajplung.00094.2014

Hirn, S., Haberl, N., Loza, K., Epple, M., Kreyling, W. G., Rothen-Rutishauser, B., Rehberg, M., & Krombach, F. (2014). Proinflammatory and cytotoxic response to nanoparticles in precision-cut lung slices. *Beilstein Journal of Nanotechnology*, *5*(1), 2440–2449. https://doi.org/10.3762/bjnano.5.253

Hoang, T.-V., Nardiello, C., Surate Solaligue, D. E., Rodríguez-Castillo, J. A., Rath, P., Mayer, K., Vadász, I., Herold, S., Ahlbrecht, K., Seeger, W., & Morty, R. E. (2018). Stereological analysis of individual lung lobes during normal and aberrant mouse lung alveolarization. *Journal of Anatomy*, *232*(3), 472–484. https://doi.org/10.1111/joa.12773

Hogan, B. L. M. (2018). Integrating Mechanical Force into Lung Development. *Developmental Cell*, *44*(3), 273–275. https://doi.org/10.1016/j.devcel.2018.01.015

Hogan, B. L. M., Barkauskas, C. E., Chapman, H. A., Epstein, J. A., Jain, R., Hsia, C. C. W., Niklason, L., Calle, E., Le, A., Randell, S. H., Rock, J., Snitow, M., Krummel, M., Stripp, B. R., Vu, T.,

White, E. S., Whitsett, J. A., & Morrisey, E. E. (2014). Repair and regeneration of the respiratory system: Complexity, plasticity, and mechanisms of lung stem cell function. *Cell Stem Cell*, *15*(2), 123–138. https://doi.org/10.1016/j.stem.2014.07.012

Horsfield, K., Gordon, W. I., Kemp, W., & Phillips, S. (1987). Growth of the bronchial tree in man. *Thorax*, *42*(5), 383–388. https://doi.org/10.1136/thx.42.5.383

Hsia, C. C. W., Hyde, D. M., Ochs, M., & Weibel, E. R. (2010). An Official Research Policy Statement of the American Thoracic Society/European Respiratory Society: Standards for Quantitative Assessment of Lung Structure. *American Journal of Respiratory and Critical Care Medicine*, *181*(4), 394–418. https://doi.org/10.1164/rccm.200809-1522ST

Huang, S., Wiszniewski, L., Constant, S., & Roggen, E. (2013). Potential of in vitro reconstituted 3D human airway epithelia (MucilAir™) to assess respiratory sensitizers. *Toxicology in Vitro: An International Journal Published in Association with BIBRA*, *27*(3), 1151–1156. https://doi.org/10.1016/j.tiv.2012.10.010

Irvin, C. G., & Bates, J. H. (2003). Measuring the lung function in the mouse: The challenge of size. *Respiratory Research*, *4*(1), 1. https://doi.org/10.1186/rr199

Jansing, N. L., Patel, N., McClendon, J., Redente, E. F., Henson, P. M., Tuder, R. M., Hyde, D. M., Nyengaard, J. R., & Zemans, R. L. (2018). Flow Cytometry Underestimates and Planimetry Overestimates Alveolar Epithelial Type 2 Cell Expansion after Lung Injury. *American Journal of Respiratory and Critical Care Medicine*, *198*(3), 390–392. https://doi.org/10.1164/rccm.201709-1838LE

Jin, G. Y., Bok, S. M., Han, Y. M., Chung, M. J., Yoon, K.-H., Kim, S. R., & Lee, Y. C. (2012). Effectiveness of rosiglitazone on bleomycin-induced lung fibrosis: Assessed by micro-computed tomography and pathologic scores. *European Journal of Radiology*, *81*(8), 1901–1906. https://doi.org/10.1016/j.ejrad.2010.12.061

Jonkman, J., & Brown, C. M. (2015). Any Way You Slice It—A Comparison of Confocal Microscopy Techniques. *Journal of Biomolecular Techniques : JBT*, *26*(2), 54–65. https://doi.org/10.7171/jbt.15-2602-003

Keller, A., Eistetter, H. R., Voss, T., & Schäfer, K. P. (1991). The pulmonary surfactant protein C (SP-C) precursor is a type II transmembrane protein. *Biochemical Journal*, *277*(Pt 2), 493–499.

Klouda, T., Condon, D., Hao, Y., Tian, W., Lvova, M., Chakraborty, A., Nicolls, M. R., Zhou, X., Raby, B. A., & Yuan, K. (2020). From 2D to 3D: Promising Advances in Imaging Lung Structure. *Frontiers in Medicine*, *0*. https://doi.org/10.3389/fmed.2020.00343

Knudsen, L., Brandenberger, C., & Ochs, M. (2021). Stereology as the 3D tool to quantitate lung architecture. *Histochemistry and Cell Biology*, *155*(2), 163–181. https://doi.org/10.1007/s00418-020-01927-0

Knust, J., Ochs, M., Gundersen, H. J. G., & Nyengaard, J. R. (2009). Stereological estimates of alveolar number and size and capillary length and surface area in mice lungs. *Anatomical Record (Hoboken, N.J.: 2007)*, *292*(1), 113–122. https://doi.org/10.1002/ar.20747

Kotton, D. N., & Morrisey, E. E. (2014). Lung regeneration: Mechanisms, applications and emerging stem cell populations. *Nature Medicine*, *20*(8), 822–832. https://doi.org/10.1038/nm.3642

Kreiger, P. A., Ruchelli, E. D., Mahboubi, S., Hedrick, H., Scott Adzick, N., & Russo, P. A. (2006). Fetal pulmonary malformations: Defining histopathology. *The American Journal of Surgical Pathology*, *30*(5), 643–649. https://doi.org/10.1097/01.pas.0000202160.03611.5b

Kretschmer, S., Dethlefsen, I., Hagner-Benes, S., Marsh, L. M., Garn, H., & König, P. (2013). Visualization of Intrapulmonary Lymph Vessels in Healthy and Inflamed Murine Lung Using CD90/Thy-1 as a Marker. *PLoS ONE*, *8*(2), e55201. https://doi.org/10.1371/journal.pone.0055201

Lambermont, V. A., Schlepütz, M., Dassow, C., König, P., Zimmermann, L. J., Uhlig, S., Kramer, B. W., & Martin, C. (2014). Comparison of Airway Responses in Sheep of Different Age in Precision-Cut Lung Slices (PCLS). *PLOS ONE*, *9*(9), e97610. https://doi.org/10.1371/journal.pone.0097610

Lei, H., & Kazlauskas, A. (2009). Growth Factors Outside of the Platelet-derived Growth Factor (PDGF) Family Employ Reactive Oxygen Species/Src Family Kinases to Activate PDGF Receptor α and Thereby Promote Proliferation and Survival of Cells. *The Journal of Biological Chemistry*, *284*(10), 6329–6336. https://doi.org/10.1074/jbc.M808426200

Li, J., Wang, Z., Chu, Q., Jiang, K., Li, J., & Tang, N. (2018). The Strength of Mechanical Forces Determines the Differentiation of Alveolar Epithelial Cells. *Developmental Cell*, *44*, 297–312. https://doi.org/10.1016/j.devcel.2018.01.008

Lignelli, E., Palumbo, F., Myti, D., & Morty, R. E. (2019). Recent advances in our understanding of the mechanisms of lung alveolarization and bronchopulmonary dysplasia. *American Journal of Physiology. Lung Cellular and Molecular Physiology*, *317*(6), L832–L887. https://doi.org/10.1152/ajplung.00369.2019

Lindahl, P., Karlsson, L., Hellström, M., Gebre-Medhin, S., Willetts, K., Heath, J. K., & Betsholtz, C. (1997). Alveogenesis failure in PDGF-A-deficient mice is coupled to lack of distal spreading of alveolar smooth muscle cell progenitors during lung development. *Development (Cambridge, England)*, *124*(20), 3943–3953.

Liu, G., Betts, C., Cunoosamy, D. M., Åberg, P. M., Hornberg, J. J., Sivars, K. B., & Cohen, T. S. (2019). Use of precision cut lung slices as a translational model for the study of lung biology. *Respiratory Research*, *20*(1), 162. https://doi.org/10.1186/s12931-019-1131-x

Liu, X., & Engelhardt, J. F. (2008). The Glandular Stem/Progenitor Cell Niche in Airway Development and Repair. *Proceedings of the American Thoracic Society*, *5*(6), 682–688. https://doi.org/10.1513/pats.200801-003AW

Liu, Y., Peterson, D. A., Kimura, H., & Schubert, D. (1997). Mechanism of cellular 3-(4,5-dimethylthiazol-2-yl)-2,5-diphenyltetrazolium bromide (MTT) reduction. *Journal of Neurochemistry*, *69*(2), 581–593. https://doi.org/10.1046/j.1471-4159.1997.69020581.x

Madurga, A., Mižíková, I., Ruiz-Camp, J., Vadász, I., Herold, S., Mayer, K., Fehrenbach, H., Seeger, W., & Morty, R. E. (2014). Systemic hydrogen sulfide administration partially restores normal alveolarization in an experimental animal model of bronchopulmonary dysplasia. *American Journal of Physiology-Lung Cellular and Molecular Physiology*, *306*(7), L684–L697. https://doi.org/10.1152/ajplung.00361.2013

Martin, C., Uhlig, S., & Ullrich, V. (1996). Videomicroscopy of methacholine-induced contraction of individual airways in precision-cut lung slices. *European Respiratory Journal*, *9*(12), 2479–2487. https://doi.org/10.1183/09031936.96.09122479

McGowan, S. E., Grossmann, R. E., Kimani, P. W., & Holmes, A. J. (2008). Platelet-Derived Growth Factor Receptor-Alpha-Expressing Cells Localize to the Alveolar Entry Ring and Have Characteristics of Myofibroblasts During Pulmonary Alveolar Septal Formation. *The Anatomical Record*, *291*(12), 1649–1661. https://doi.org/10.1002/ar.20764

McGowan, S. E., Harvey, C. S., & Jackson, S. K. (1995). Retinoids, retinoic acid receptors, and cytoplasmic retinoid binding proteins in perinatal rat lung fibroblasts. *The American Journal of Physiology*, *269*(4 Pt 1), L463-472. https://doi.org/10.1152/ajplung.1995.269.4.L463

Meng, F., Wu, N. H., Nerlich, A., Herrler, G., Valentin-Weigand, P., & Seitz, M. (2015). Dynamic Virus-Bacterium Interactions in a Porcine Precision-Cut Lung Slice Coinfection Model: Swine Influenza Virus Paves the Way for Streptococcus suis Infection in a Two-Step Process. *Infection and Immunity*, *83*(7), 2806–2815. https://doi.org/10.1128/IAI.00171-15

Mindt, B. C., Fritz, J. H., & Duerr, C. U. (2018). Group 2 Innate Lymphoid Cells in Pulmonary Immunity and Tissue Homeostasis. *Frontiers in Immunology*, *9*(840). https://doi.org/10.3389/fimmu.2018.00840

Minoo, P., Su, G., Drum, H., Bringas, P., & Kimura, S. (1999). Defects in tracheoesophageal and lung morphogenesis in Nkx2.1(-/-) mouse embryos. *Developmental Biology*, *209*(1), 60–71. https://doi.org/10.1006/dbio.1999.9234

Mižíková, I., & Morty, R. E. (2015). The Extracellular Matrix in Bronchopulmonary Dysplasia: Target and Source. *Frontiers in Medicine*, *2*(91). https://doi.org/10.3389/fmed.2015.00091

Mižíková, I., Ruiz-Camp, J., Steenbock, H., Madurga, A., Vadász, I., Herold, S., Mayer, K., Seeger, W., Brinckmann, J., & Morty, R. E. (2015). Collagen and elastin cross-linking is altered during aberrant late lung development associated with hyperoxia. *American Journal of Physiology-Lung Cellular and Molecular Physiology*, *308*(11), L1145–L1158. https://doi.org/10.1152/ajplung.00039.2015

Molina-Torres, C. A., Flores-Castillo, O. N., Carranza-Torres, I. E., Guzmán-Delgado, N. E., Viveros-Valdez, E., Vera-Cabrera, L., Ocampo-Candiani, J., Verde-Star, J., Castro-Garza, J., & Carranza-Rosales, P. (2020). Ex vivo infection of murine precision-cut lung tissue slices with Mycobacterium abscessus: A model to study antimycobacterial agents. *Annals of Clinical Microbiology and Antimicrobials*, *19*(1), 52. https://doi.org/10.1186/s12941-020-00399-3

Morrisey, E. E., & Hogan, B. L. M. (2010). Preparing for the first breath: Genetic and cellular mechanisms in lung development. *Developmental Cell*, *18*(1), 8–23. https://doi.org/10.1016/j.devcel.2009.12.010

Mosmann, T. (1983). Rapid colorimetric assay for cellular growth and survival: Application to proliferation and cytotoxicity assays. *Journal of Immunological Methods*, *65*(1), 55–63. https://doi.org/10.1016/0022-1759(83)90303-4

Mühlfeld, C., Hegermann, J., Wrede, C., & Ochs, M. (2015). A review of recent developments and applications of morphometry/stereology in lung research. *American Journal of Physiology-Lung Cellular and Molecular Physiology*, *309*(6), L526–L536. https://doi.org/10.1152/ajplung.00047.2015

Mühlfeld, C., & Ochs, M. (2013). Quantitative microscopy of the lung: A problem-based approach. Part 2: stereological parameters and study designs in various diseases of the respiratory tract. *American Journal of Physiology-Lung Cellular and Molecular Physiology*, *305*(3), L205–L221. https://doi.org/10.1152/ajplung.00427.2012

Mühlfeld, C., Weibel, E. R., Hahn, U., Kummer, W., Nyengaard, J. R., & Ochs, M. (2010). Is length an appropriate estimator to characterize pulmonary alveolar capillaries? A critical evaluation in the human lung. *Anatomical Record*, *293*(7), 1270–1275. https://doi.org/10.1002/ar.21158

Mund, S. I., Stampanoni, M., & Schittny, J. C. (2008). Developmental alveolarization of the mouse lung. *Developmental dynamics: an official publication of the American Association of Anatomists, 237*(8), 2108-2116. https://doi.org/10.1002/dvdy.21633

Muzumdar, M. D., Tasic, B., Miyamichi, K., Li, L., & Luo, L. (2007). A global double-fluorescent Cre reporter mouse. *Genesis*, *45*(9), 593–605. https://doi.org/10.1002/dvg.20335

Netter, F. H. (2008). *Atlas of Human Anatomy*, (4th ed). Saunders/Elservier. https://pubs.rsna.org/doi/10.1148/radiol.2482082518

Neuhaus, V., Schaudien, D., Golovina, T., Temann, U.-A., Thompson, C., Lippmann, T., Bersch, C., Pfennig, O., Jonigk, D., Braubach, P., Fieguth, H.-G., Warnecke, G., Yusibov, V., Sewald, K., & Braun, A. (2017). Assessment of long-term cultivated human precision-cut lung slices as an ex vivo system for evaluation of chronic cytotoxicity and functionality. *Journal of Occupational Medicine and Toxicology*, *12*(1), 13. https://doi.org/10.1186/s12995-017-0158-5

Nogee, L. M. (2017). Interstitial lung disease in newborns. *Seminars in Fetal & Neonatal Medicine*, *22*(4), 227–233. https://doi.org/10.1016/j.siny.2017.03.003

Ntokou, A., Klein, F., Dontireddy, D., Becker, S., Bellusci, S., Richardson, W. D., Szibor, M., Braun, T., Morty, R. E., Seeger, W., Voswinckel, R., & Ahlbrecht, K. (2015). Characterization of the platelet-derived growth factor receptor-α-positive cell lineage during murine late lung development. *American Journal of Physiology. Lung Cellular and Molecular Physiology*, *309*(9), L942-958. https://doi.org/10.1152/ajplung.00272.2014

Ochs, M., Nyengaard, J. R., Jung, A., Knudsen, L., Voigt, M., Wahlers, T., ... & Gundersen, H. J. G. (2004). The number of alveoli in the human lung. *American journal of respiratory and critical care medicine*, *169*(1), 120-124. https://doi.org/10.1164/rccm.200308-1107OC

Ochs, M. (2006). A brief update on lung stereology. *Journal of Microscopy*, *222*(Pt 3), 188–200. https://doi.org/10.1111/j.1365-2818.2006.01587.x

Parrish, A. R., Gandolfi, A. J., & Brendel, K. (1995). Precision-cut tissue slices: Applications in pharmacology and toxicology. *Life Sciences*, *57*(21), 1887–1901. https://doi.org/10.1016/0024-3205(95)02176-j

Pederiva, F., Martinez, L., & Tovar, J. A. (2012). Retinoic acid rescues deficient airway innervation and peristalsis of hypoplastic rat lung explants. *Neonatology*, *101*(2), 132–139. https://doi.org/10.1159/000329613

Pérez-Bravo, D., Myti, D., Mižíková, I., Pfeffer, T., Surate Solaligue, D. E., Nardiello, C., Vadász, I., Herold, S., Seeger, W., Ahlbrecht, K., & Morty, R. E. (2021). A comparison of airway pressures for inflation fixation of developing mouse lungs for stereological analyses. *Histochemistry and Cell Biology*, *155*(2), 203–214. https://doi.org/10.1007/s00418-020-01951-0

Pérez-Gil, J. (2008). Structure of pulmonary surfactant membranes and films: The role of proteins and lipid–protein interactions. *Biochimica et Biophysica Acta (BBA) - Biomembranes*, *1778*(7), 1676–1695. https://doi.org/10.1016/j.bbamem.2008.05.003

Pieretti, A. C., Ahmed, A. M., Roberts, J. D., & Kelleher, C. M. (2014). A novel in vitro model to study alveologenesis. *American Journal of Respiratory Cell and Molecular Biology*, *50*(2), 459–469. https://doi.org/10.1165/rcmb.2013-0056OC

Placke, M. E., & Fisher, G. L. (1987). Adult peripheral lung organ culture—A model for respiratory tract toxicology. *Toxicology and Applied Pharmacology*, *90*(2), 284–298. https://doi.org/10.1016/0041-008x(87)90336-x

Pozarska, A., Rodríguez-Castillo, J. A., Surate Solaligue, D. E., Ntokou, A., Rath, P., Mižíková, I., Madurga, A., Mayer, K., Vadász, I., Herold, S., Ahlbrecht, K., Seeger, W., & Morty, R. E. (2017). Stereological monitoring of mouse lung alveolarization from the early postnatal period to adulthood. *American Journal of Physiology-Lung Cellular and Molecular Physiology*, *312*(6), L882–L895. https://doi.org/10.1152/ajplung.00492.2016

Que, J., Choi, M., Ziel, J. W., Klingensmith, J., & Hogan, B. L. M. (2006). Morphogenesis of the trachea and esophagus: Current players and new roles for noggin and Bmps. *Differentiation; Research in Biological Diversity*, *74*(7), 422–437. https://doi.org/10.1111/j.1432-0436.2006.00096.x

Rackley, C. R., & Stripp, B. R. (2012). Building and maintaining the epithelium of the lung. *The Journal of Clinical Investigation*, *122*(8), 2724–2730. https://doi.org/10.1172/JCI60519

Rawlins, E. L. (2011). The building blocks of mammalian lung development. *Developmental Dynamics: An Official Publication of the American Association of Anatomists*, *240*(3), 463–476. https://doi.org/10.1002/dvdy.22482

Rawlins, E. L., Okubo, T., Xue, Y., Brass, D. M., Auten, R. L., Hasegawa, H., Wang, F., & Hogan, B. L. M. (2009). The role of Scgb1a1+ Clara cells in the long-term maintenance and repair of lung airway, but not alveolar, epithelium. *Cell Stem Cell*, *4*(6), 525–534. https://doi.org/10.1016/j.stem.2009.04.002

Rawlins, E. L., Ostrowski, L. E., Randell, S. H., & Hogan, B. L. M. (2007). Lung development and repair: Contribution of the ciliated lineage. *Proceedings of the National Academy of Sciences of the United States of America*, *104*(2), 410–417. https://doi.org/10.1073/pnas.0610770104

Rawlins, E. L., & Perl, A.-K. (2012). The a"MAZE"ing world of lung-specific transgenic mice. *American Journal of Respiratory Cell and Molecular Biology*, *46*(3), 269–282. https://doi.org/10.1165/rcmb.2011-0372PS

Ressmeyer, A. R., Larsson, A. K., Vollmer, E., Dahlèn, S. E., Uhlig, S., & Martin, C. (2006). Characterisation of guinea pig precision-cut lung slices: Comparison with human tissues. *European Respiratory Journal*, *28*(3), 603–611. https://doi.org/10.1183/09031936.06.00004206

Richard L. Drake, Wayne, Mi., & Adam, W. M. (2014). *Gray's Anatomy for Students* (3rd Edition). Elservier. https://www.elsevier.com/books/grays-anatomy-for-students/drake/978-0-323-39304-1

Rinkevich, Y., Mori, T., Sahoo, D., Xu, P.-X., Bermingham, J. R., & Weissman, I. L. (2012). Identification and prospective isolation of a mesothelial precursor lineage giving rise to smooth muscle cells and fibroblasts for mammalian internal organs, and their vasculature. *Nature Cell Biology*, *14*(12), 1251–1260. https://doi.org/10.1038/ncb2610

Rock, J. R., & Hogan, B. L. M. (2011). Epithelial progenitor cells in lung development, maintenance, repair, and disease. *Annual Review of Cell and Developmental Biology*, *27*, 493–512. https://doi.org/10.1146/annurev-cellbio-100109-104040

Rock, J. R., Randell, S. H., & Hogan, B. L. M. (2010). Airway basal stem cells: A perspective on their roles in epithelial homeostasis and remodeling. *Disease Models & Mechanisms*, *3*(9-10), 545–556. https://doi.org/10.1242/dmm.006031

Rodríguez-Castillo, J. A., Perez-Bravo, D., Ntokou, A., Seeger, W., Morty, R. E., & Ahlbrecht, K. (2018). Understanding alveolarization to induce lung regeneration. *Respiratory Research*, *19*(148). https://doi.org/doi.org/10.1186/s12931-018-0837-5

Romar, G. A., Kupper, T. S., & Divito, S. J. (2016). Research Techniques Made Simple: Techniques to Assess Cell Proliferation. *Journal of Investigative Dermatology*, *136*(1), e1–e7. https://doi.org/10.1016/j.jid.2015.11.020

Rosales Gerpe, M. C., van Vloten, J. P., Santry, L. A., de Jong, J., Mould, R. C., Pelin, A., Bell, J. C., Bridle, B. W., & Wootton, S. K. (2018). Use of Precision-Cut Lung Slices as an Ex Vivo Tool for Evaluating Viruses and Viral Vectors for Gene and Oncolytic Therapy. *Molecular Therapy Methods & Clinical Development*, *10*, 245–256. https://doi.org/10.1016/j.omtm.2018.07.010

Rubin, B. K. (2014). Secretion properties, clearance, and therapy in airway disease. *Translational Respiratory Medicine*, *2*(6). https://doi.org/doi.org/10.1186/2213-0802-2-6

Rubins, J. B. (2003). Alveolar Macrophages. *American Journal of Respiratory and Critical Care Medicine*, *167*(2), 103–104. https://doi.org/10.1164/rccm.2210007

Ruiz-Camp, J., & Morty, R. E. (2015). Divergent fibroblast growth factor signaling pathways in lung fibroblast subsets: Where do we go from here? *American Journal of Physiology. Lung Cellular and Molecular Physiology*, *309*(8), L751-755. https://doi.org/10.1152/ajplung.00298.2015

Rydell-Törmänen, K., & Johnson, J. R. (2018). The Applicability of Mouse Models to the Study of Human Disease. *Mouse Cell Culture*, *1940*, 3–22. https://doi.org/10.1007/978-1-4939-9086-3_1

Salic, A., & Mitchison, T. J. (2008). A chemical method for fast and sensitive detection of DNA synthesis in vivo. *Proceedings of the National Academy of Sciences*, *105*(7), 2415–2420. https://doi.org/10.1073/pnas.0712168105

Schittny, J.C. (2017). Development of the lung. *Cell Tissue Research, 367*, 427–444. https://doi.org/10.1007/s00441-016-2545-0

Schneider, J. P., & Ochs, M. (2014). Alterations of mouse lung tissue dimensions during processing for morphometry: A comparison of methods. *American Journal of Physiology-Lung Cellular and Molecular Physiology*, *306*(4), L341–L350. https://doi.org/10.1152/ajplung.00329.2013

Seehase, S., Lauenstein, H.-D., Schlumbohm, C., Switalla, S., Neuhaus, V., Förster, C., Fieguth, H.-G., Pfennig, O., Fuchs, E., Kaup, F.-J., Bleyer, M., Hohlfeld, J. M., Braun, A., Sewald, K., & Knauf, S. (2012). LPS-induced lung inflammation in marmoset monkeys—An acute model for anti-inflammatory drug testing. *PloS One*, *7*(8), e43709. https://doi.org/10.1371/journal.pone.0043709

Shihan, M. H., Novo, S. G., Le Marchand, S. J., Wang, Y., & Duncan, M. K. (2021). A simple method for quantitating confocal fluorescent images. *Biochemistry and Biophysics Reports*, *25*, 100916. https://doi.org/10.1016/j.bbrep.2021.100916

Siminski, J. T., Kavanagh, T. J., Chi, E., & Raghu, G. (1992). Long-term maintenance of mature pulmonary parenchyma cultured in serum-free conditions. *The American Journal of Physiology*, *262*(1 Pt 1), L105-110. https://doi.org/10.1152/ajplung.1992.262.1.L105

Sobecki, M., Mrouj, K., Camasses, A., Parisis, N., Nicolas, E., Llères, D., Gerbe, F., Prieto, S., Krasinska, L., David, A., Eguren, M., Birling, M. C., Urbach, S., Hem, S., Déjardin, J., Malumbres, M., Jay, P., Dulic, V., Lafontaine, D., Feil, R., Fisher, D. (2016). The cell proliferation antigen Ki-67 organises heterochromatin. *eLife*, *5*, e13722. https://doi.org/10.7554/eLife.13722

Sorokin, S. P., Hoyt, R. F., & Shaffer, M. J. (1997). Ontogeny of neuroepithelial bodies: Correlations with mitogenesis and innervation. *Microscopy Research and Technique*, *37*(1), 43–61. https://doi.org/10.1002/(SICI)1097-0029(19970401)37:1<43::AID-JEMT5>3.0.CO;2-X

Stone, K. C., Mercer, R. R., Gehr, P., Stockstill, B., & Crapo, J. D. (1992). Allometric Relationships of Cell Numbers and Size in the Mammalian Lung. *American Journal of Respiratory Cell and Molecular Biology*, *6*(2), 235–243. https://doi.org/10.1165/ajrcmb/6.2.235

Suarez, C. J., Dintzis, S. M., & Frevert, C. W. (2012). Respiratory. In P. M. Treuting & S. M. Dintzis (Eds.), *Comparative Anatomy and Histology* (1st ed., pp. 121–134). Academic Press. https://doi.org/10.1016/B978-0-12-381361-9.00009-3

Tang, Z., Hu, Y., Wang, Z., Jiang, K., Zhan, C., Marshall, W. F., & Tang, N. (2018). Mechanical Forces Program the Orientation of Cell Division during Airway Tube Morphogenesis. *Developmental Cell*, *44*(3), 313-325.e5. https://doi.org/10.1016/j.devcel.2017.12.013

Temann, A., Golovina, T., Neuhaus, V., Thompson, C., Chichester, J. A., Braun, A., & Yusibov, V. (2017). Evaluation of inflammatory and immune responses in long-term cultured human precision-cut lung slices. *Human Vaccines & Immunotherapeutics*, *13*(2), 351–358. https://doi.org/10.1080/21645515.2017.1264794

Thurlbeck W. M. (1982). Postnatal human lung growth. *Thorax*, *37*(8), 564–571. https://doi.org/10.1136/thx.37.8.564

Titford, M. (2005). The long history of hematoxylin. *Biotechnic & Histochemistry*, *80*(2), 73–78. https://doi.org/10.1080/10520290500138372

Tomashefski, J. F., & Farver, C. F. (2008). Anatomy and Histology of the Lung. In J. F. Tomashefski, P. T. Cagle, C. F. Farver, & A. E. Fraire (Eds.), *Dail and Hammar's Pulmonary Pathology: Volume I: Nonneoplastic Lung Disease* (pp. 20–48). Springer. https://doi.org/10.1007/978-0-387-68792-6_2

Tomkeieff, S. I. (1945). Linear Intercepts, Areas and Volumes. *Nature*, *155*(3923), 24–24. https://doi.org/10.1038/155024a0

Torday, J. S., & Rehan, V. K. (2002). Stretch-stimulated surfactant synthesis is coordinated by the paracrine actions of PTHrP and leptin. *American Journal of Physiology. Lung Cellular and Molecular Physiology*, *283*(1), L130-135. https://doi.org/10.1152/ajplung.00380.2001

Travaglini, K. J., Nabhan, A. N., Penland, L., Sinha, R., Gillich, A., Sit, R. V., Chang, S., Conley, S. D., Mori, Y., Seita, J., Berry, G. J., Shrager, J. B., Metzger, R. J., Kuo, C. S., Neff, N., Weissman, I. L., Quake, S. R., & Krasnow, M. A. (2020). A molecular cell atlas of the human lung from single cell RNA sequencing. *Nature*, *587*(7835), 619–625. https://doi.org/10.1038/s41586-020-2922-4

Tschanz, S. A., Salm, L. A., Roth-Kleiner, M., Barré, S. F., Burri, P. H., & Schittny, J. C. (2014). Rat lungs show a biphasic formation of new alveoli during postnatal development. *Journal of Applied Physiology*, *117*(1), 89–95. https://doi.org/10.1152/japplphysiol.01355.2013

Van de Velde, S. (1980). Glycol methacrylate embedding and staining. *Micron*, *11*(2), 203–205. https://doi.org/10.1016/0047-7206(80)90159-4

Van Dijk, E. M., Culha, S., Menzen, M. H., Bidan, C. M., & Gosens, R. (2016). Elastase-Induced Parenchymal Disruption and Airway Hyper Responsiveness in Mouse Precision Cut Lung Slices: Toward an Ex vivo COPD Model. *Frontiers in Physiology*, *7*, 657. https://doi.org/10.3389/fphys.2016.00657

Van Lommel, A. (2001). Pulmonary neuroendocrine cells (PNEC) and neuroepithelial bodies (NEB): Chemoreceptors and regulators of lung development. *Paediatric Respiratory Reviews*, *2*(2), 171–176. https://doi.org/10.1053/prrv.2000.0126

Van Lommel, A., Lauweryns, J. M., & Berthound, H. R. (1998). Pulmonary neuroepithelial bodies are innervated by vagal afferent nerves: An investigation with in vivo anterograde DiI tracing and confocal microscopy. *Anatomy and Embryology*, *197*(4), 325–330. https://doi.org/10.1007/s004290050142

van Tuyl, M., Groenman, F., Wang, J., Kuliszewski, M., Liu, J., Tibboel, D., & Post, M. (2007). Angiogenic factors stimulate tubular branching morphogenesis of sonic hedgehog-deficient lungs. *Developmental Biology*, *303*(2), 514–526. https://doi.org/10.1016/j.ydbio.2006.11.029

Warburg, O., & Minami, S. (1923). Versuche an Überlebendem Carcinom-gewebe. *Klinische Wochenschrift*, *2*(17), 776–777. https://doi.org/10.1007/BF01712130

Weibel, E. R., Hsia, C. C., & Ochs, M. (2007). How much is there really? Why stereology is essential in lung morphometry. *Journal of applied physiology*, *102*(1), 459-467. https://doi.org/10.1152/japplphysiol.00808.2006

Whitsett, J. A., Wert, S. E., & Weaver, T. E. (2010). Alveolar surfactant homeostasis and the pathogenesis of pulmonary disease. *Annual Review of Medicine*, *61*, 105–119. https://doi.org/10.1146/annurev.med.60.041807.123500

Willführ, A., Brandenberger, C., Piatkowski, T., Grothausmann, R., Nyengaard, J. R., Ochs, M., & Mühlfeld, C. (2015). Estimation of the number of alveolar capillaries by the Euler number (Euler-Poincaré characteristic). *American Journal of Physiology. Lung Cellular and Molecular Physiology*, *309*(11), L1286-1293. https://doi.org/10.1152/ajplung.00410.2014

Wohlsen, A., Martin, C., Vollmer, E., Branscheid, D., Magnussen, H., Becker, W.-M., Lepp, U., & Uhlig, S. (2003). The early allergic response in small airways of human precision-cut lung slices. *European Respiratory Journal*, *21*(6), 1024–1032. https://doi.org/10.1183/09031936.03.00027502

Wongtrakool, C., Malpel, S., Gorenstein, J., Sedita, J., Ramirez, M. I., Underhill, T. M., & Cardoso, W. V. (2003). Down-regulation of retinoic acid receptor alpha signaling is required for sacculation and type I cell formation in the developing lung. *The Journal of Biological Chemistry*, *278*(47), 46911–46918. https://doi.org/10.1074/jbc.M307977200

Wu, S., & Savani, R. C. (2019). Chapter 1—Molecular Bases for Lung Development, Injury, and Repair. In E. Bancalari (Ed.), *The Newborn Lung (Third Edition)* (pp. 3–29). Elsevier. https://doi.org/10.1016/B978-0-323-54605-8.00001-5

Wu, W., Booth, J. L., Duggan, E. S., Wu, S., Patel, K. B., Coggeshall, K. M., & Metcalf, J. P. (2010). Innate immune response to H3N2 and H1N1 influenza virus infection in a human lung organ culture model. *Virology*, *396*(2), 178–188. https://doi.org/10.1016/j.virol.2009.10.016

Yamamoto, H., Yun, E. J., Gerber, H.-P., Ferrara, N., Whitsett, J. A., & Vu, T. H. (2007). Epithelial-vascular cross talk mediated by VEGF-A and HGF signaling directs primary septae formation during distal lung morphogenesis. *Developmental Biology*, *308*(1), 44–53. https://doi.org/10.1016/j.ydbio.2007.04.042

Zeltner, T. B., & Burri, P. H. (1987). The postnatal development and growth of the human lung. II. Morphology. *Respiration Physiology*, *67*(3), 269–282. https://doi.org/10.1016/0034-5687(87)90058-2

8. List of abbreviations

5

5-Ethinyl-2′-deoxyuridin: (EdU)

A

Acinar epithelium into the alveolar epithelial type I cells: (AECI)
Actin beta: (ACTB)
Air liquid interface: (ALI)
Alpha-smooth muscle actin: (ACTA2)

Ch

Chronic obstructive pulmonary disease: (COPD)

C

Coefficient of error: (CE)
Coefficient of variation: (CV)
Confocal laser scanning microscopy (CLSM)

D

Distilled water: (ddH_2O)

E

Embryonic day: (E)
Epithelial-to-mesenchymal transition: (EMT)
Extracellular matrix: (ECM)

F

Fibroblast growth factor: (FGF)

G

Glycol methacrylate: (GMA)
Green fluorescent protein: (GFP)

H

Hematoxylin and eosin: (H&E)
Hours: (h)

I

Idiopathic pulmonary fibrosis: (IPF)

M

Mean Linear Intercept: (MLI)
Membrane tandemTomato: (mtdTomato)
Minutes: (min)

O

Optical Density: (OD)
Osmium tetroxide: (OsO4)

P

Paraformaldehyde: (PFA)
Penicillin streptomycin: (PS)
Phosphate-buffered saline: PBS
Platelet-derived growth factor receptor α: (PDGFR α)
Polymerase chain reaction: (qPCR)
Post-natal day: (P)
Precision Cut Lung Slice imaging: (PCLSi)
Precision-cut lung slices: (PCLS)

R

Room temperature: (RT)

S

Seconds: (sec)
Surface density: (SV)
Surfactant-producing type II cells: (AECII)

T

Thyroid transcription factor 1: (TTF-1)
Tris(hydroxymethyl)aminomethane: (TRIS)

V

Vimentin: (VIM)

A

α-Smooth muscle actin: (αSMA)+

B

β-Actin promoter: (ACTB)

10. List of figures

Figure 1. Lower respiratory tract. 7
Figure 2. Phases of human and mouse lung development. 8
Figure 3. Anatomy of the airways. 11
Figure 4. Alveolar epithelial cells during alveolarization. 13
Figure 5. Cell proliferation of entire lung culture vs PCLS culture. 36
Figure 6. Quantification of cell proliferation in PCLS. 38
Figure 7. Viability assay performed in PCLS. 39
Figure 8. Confocal laser scanning imaging and stereological analysis of mTmG PCLS. 40
Figure 9. Stereological analysis of 300-µm-thick PCLS in paraffin. 42
Figure 10. Stereological analysis of 1,000-µm thick PCLS in paraffin. 43
Figure 11. Comparison between in vitro 300-µm- and 1,000-µm-thick PCLS embedded in paraffin. 44
Figure 12. Stereological analysis of 300-µm-thick PCLS embedded in GMA. 45
Figure 13. **Stereological analysis of 1000µm thickness PCLS embedded in GMA**.. 46
Figure 14. Comparison between in vitro P3 PCLS 300-µm- and 1,000-µm-thick P4 PCLS embedded in GMA. 47
Figure 15. Comparison of stereological parameters using paraffin- and GMA-embedded PCLS from different aged mice. 48
Figure 16. Mesenchymal gene marker expression in cultured P3 PCLS and in vivo control PCLS. 49
Figure 17. Expression of epithelial and one marker for proliferation in murine P3 cultured PCLS and in vivo control PCLS. 50
Figure 18. Visualization of Podoplanin and Platelet-derived growth factor receptor α in murine postnatal P3 PCLS cultured for 72h and in vivo control P3 and P7 PCLS.. 51
Figure 19. Alveolar structure and cell population during *in vitro* culture of PCLS.. 59

11. List of tables

Table 1. Master mix for genotyping of transgenic mice. 26
Table 2. Cycling parameters used for genotyping of transgenic mice. 26
Table 3. Cocktail solution for EdU detection 29
Table 4. Master mix used to prepare cDNA for gene expression analysis. 32
Table 5. Cycling conditions used for qPCR gene expression. 33

Table S 1. P values obtained from Student's T-test for the quantification of cell proliferation in PCLS. 81
Table S 2. P values obtained from Student's T-test for the quantification of cell viability in PCLS 81
Table S 3. Structural parameters of in vivo and in vitro PCLS of mTmG P3 and P7 mice using confocal imaging. 83
Table S 4. Structural parameters of in vivo and in vitro PCLS from mTmG P7 and P14 mice using confocal imaging 83
Table S 5. Structural parameters of in vivo and in vitro 300-µm-thick PCLS in embedded in paraffin. 84
Table S 6. Structural parameters of in vivo and in vitro 1,000-µm-thick PCLS in embedded in paraffin 84
Table S 7. Structural parameters of in vivo and in vitro 300-µm-thick PCLS in embedded in GMA. 85
Table S 8. Structural parameters of in vivo and in vitro 1,000-µm-thick PCLS in embedded in GMA 85
Table S 9. Compared structural parameters between 300- µm- and 1,000-µm-thick in vitro PCLS in embedded in paraffin. 86
Table S 10. Compared structural parameters between 300- µm- and 1,000-µm-thick in vitro PCLS in embedded in GMA 86
Table S 11. Compared structural parameters between GMA- and paraffin-embedded in vivo and in vitro PCLS. 87
Table S 12. Compared values for measured mesenchymal, epithelial and proliferation gene expressed markers in PCL 87

12. Summary

Precision-cut lung slices (PCLS) are *ex-vivo* lung explants, three-dimensional lung tissue slices, that contain nearly all cells that are usually found in the lung. As lung PCLS maintains the 3-dimensional (3D) architecture, this model was popularized as a model of the microenvironment of the respiratory tract. Different approaches have been performed and suggested that alveolarization, cell proliferation and differentiation take place in cultured PCLS from postnatal mice.

The present study aimed to validate the *in vitro* system of cultured postnatal PCLS as a tool to study alveolarization using stereological approaches. *In vitro* cultured PCLS from mice presented abundant cell proliferation compared to the culture of the entire lung. Analyzing an organ with a heterogeneous structure such as the lung, requires a reliable method of quantification such as stereology. A comparison between paraffin and Glycol methacrylate embedding techniques using stereology demonstrated that sample processing and different embedding methodology significantly altered morphological parameters of PCLS.

Analyses of cellular marker expression demonstrated expression of both epithelial and mesenchymal markers, demonstrating cells are functional. During the present study, P3 PCLS cultured for 72h and 300-µm-thick PCLS have showed an increase in septum thickness, mimicking structural composition of IPF. Also, 1,000-µm-thick P4 PCLS culture for 96h demonstrated the same pattern. Taken together, the present study contributed to a better understanding of different visualization and embedding techniques used in stereology in postnatal cultured PCLS.

Evidence was given, that alveolarization could not be detected in cultured postnatal PCLS. However, the system could be used to study cellular functions such proliferation and marker expression upon modulation.

13. Zusammenfassung

Precision Cut Lung Slices (PCLS) sind *ex-vivo* dreidimensionale (3D) Lungengewebeschnitte, die nahezu alle Zellarten enthalten, die normalerweise in der Lunge vorkommen. Daher wurde dieses Modell als Modell für die Mikroumgebung der Atemwege vierfach genutzt in verschiedenen Ansätzen wurde gezeigt, dass während der Alveolarisierung, Zellproliferation und Differenzierung in kultivierten PCLS von postnatalen Mäusen stattfindet.

Ziel der vorliegenden Arbeit war es, dass *in-vitro*-PCLS-System als Werkzeug zur Analyse der Alveolarisierung in der Lunge von postnatalen Mäusen zu validieren. Kultivierung von *in-vitro*-PCLS von postnatalen Mäusen zeigte im Vergleich zur Kultivierung der gesamten Lunge eine verstärkte Zellproliferation. Analyse von Organen mit einer heterogenen Struktur, wie der Lunge bedarf einer zuverlässigen Quantifizierungsmethode. Ein Vergleich zwischen Paraffin und Glycol Methacrylate eingebetteten Schnitten analysiert mittels Stereologie zeigte, dass die Handhabung der Proben und die Art der Einbettung die morphologischen Parameter der PCLS signifikant verändern konnte.

Analyse der zellspezifischen Gene Expression zeigte eine Expression sowohl epithelialer als auch mesenchymaler Marker, was darauf hindeutet, dass diese Zellarten in Kultur aktiv sein können. Die vorliegende Arbeit zeigte, dass P3 PCLS kultiviert für 72h, eine vermeinte Septumdicke zeigten, ähnlich wie bei fibrotischen Prozessen der Lunge. Gleiches war zu beobachten bei P4 PCLS kultiviert für 96h. Zusammenfassend trägt die vorliegende Arbeit zu einem besseren Verständnis verschiedener Visualisierungs- und Einbettungsmethoden im Rahmen stereologischier Analysen in postnatalen PCLS bei.

Es wurde gezeigt, dass der Prozess der Alveolisierung in kultivierten postnatalen PCLS nicht stattfindet. Dennoch wurde gezeigt, dass das System genutzt werden kann, um zelluläre Funktionen wie Proliferation oder Expression Zelltyp spezifischer Gene unter Modulation zu Analysieren.

14. Appendix

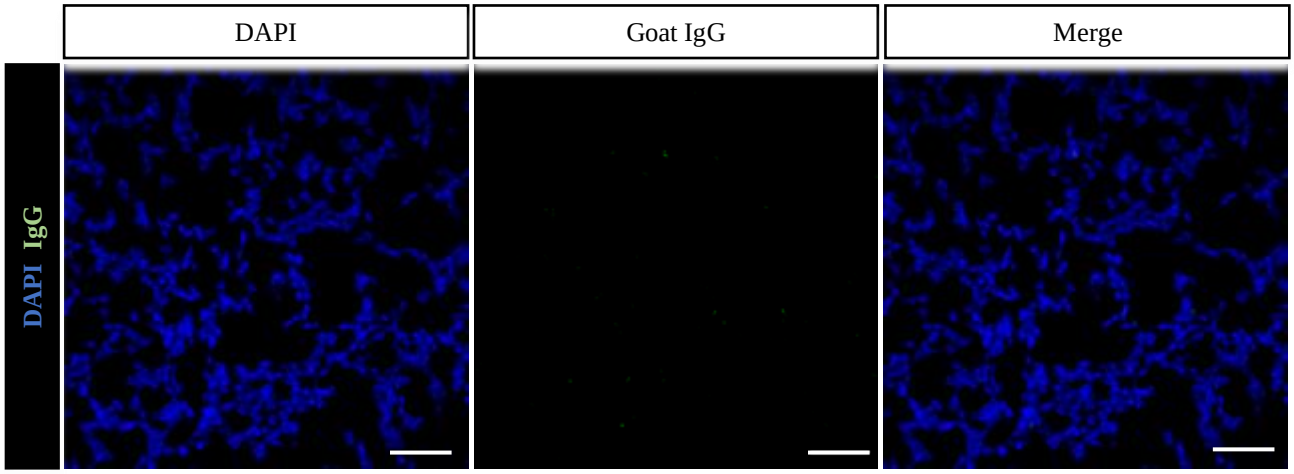

Figure S 1. Control stainings for the Podoplanin stainings in Figure 19. Control staining images were taken from samples incubated with isotype control antibodies as a replacement for primary anti-podoplanin antibody (green). DAPI (blue) staining was employed to visualize the nuclei of all cells present in the section.

Table S 1. *P* values obtained from Student's T-test for the quantification of cell proliferation in PCLS.

Comparsion between time-points	*P* values
P3+24h vs. P3+72h	<0.0001
P7+24h vs. P7+72h	<0.0001
P3+24h vs. P7+24h	0.6808
P3+72h vs. P7+72h	<0.0001

Table S 2. *P* values obtained from Student's T-test for the quantification of cell viability in PCLS.

Comparsion between time-points	*P* values
Mock vs. P3	<0.0001
Mock vs. P3+24h	<0.0001
Mock vs. P3+72h	0.0002
P3 vs. P3+24h	<0.0001
P3 vs. P3+72h	<0.0001
P3+24h vs. P3+72h	0.2689

Mock vs. P7	<0.0001
Mock vs. P7+24h	<0.0001
Mock vs. P7+72h	0.0005
P7 vs. P7+24h	0.6198
P7 vs. P7+72h	<0.0001
P7+24h vs. P7+72h	0.0022

Table S 3. Structural parameters of *in vivo* and *in vitro* PCLS of mTmG P3 and P7 mice using confocal imaging.

			P3			**P3+24h**				**P3+72h**					**P7**				
			mean ± S.D.			mean ± S.D.			P3	mean ± S.D.			P3	P3+24h	mean ± S.D.			P3	P3+24h	P3+72h
***Sv* [cm^{-1}]**			321.36 ± 39.77			313.25 ± 23.42			0.9992	355.15 ± 45.68			0.5499	0.5057	493.32 ± 58.58			<0.0001	<0.0001	<0.0001
CE	**CV**	**CE^2/CV^2**	0.055	0.124	0.200	0.033	0.075	0.200		0.058	0.129	0.200			0.053	0.119	0.200			
***τ* (sep) [µm]**			24.33 ± 3.24			28.32 ± 2.89			0.2375	24.91 ± 5.04			0.9917	0.3987	19.76 ± 3.467			0.0932	0.001	0.063
CE	**CV**	**CE^2/CV^2**	0.059	0.133	0.200	0.046	0.102	0.200		0.090	0.202	0.200			0.090	0.202	0.200			
MLI [µm]			73.93 ± 15.65			69.54 ± 6.06			0.5414	64.33 ± 10.40			0.1407	0.8256	42.48 ± 4.79			<0.0001	0.0003	0.0032
CE	**CV**	**CE^2/CV^2**	0.059	0.133	0.200	0.046	0.102	0.200		0.090	0.202	0.200			0.078	0.175	0.200			

Abbreviations: *CE*, coefficient of error; *CV*, coefficient of variation; *h*, hours in medium culture; *P*, Post-natal day; *MLI*, mean linear intercept; *SV*, surface density; τ, arithmetic mean septal thickness; Values are presented as mean ± S.D., standard deviation. *N* = 5 lungs per group. One-way ANOVA with Tukey's *post hoc* analysis was used to determine *P* values.

Table S 4. Structural parameters of *in vivo* and *in vitro* PCLS from mTmG P7 and P14 mice using confocal imaging

			P7			**P7+24h**				**P7+72h**					**P14**				
			mean ± S.D.			mean ± S.D.			P3	mean ± S.D.			P3	P3+24h	mean ± S.D.			P3	P3+24h	P3+72h
***Sv* [cm^{-1}]**			493.32 ± 58.58			429.61 ± 273.46			0.3251	460.24 ± 106.16			0.8421	0.8723	703.46 ± 563.95			<0.0001	<0.0001	<0.0001
CE	**CV**	**CE^2/CV^2**	0.053	0.119	0.200	0.076	0.171	0.200		0.103	0.231	0.200			0.041	0.091	0.200			
***τ* (sep) [µm]**			19.76 ± 3.467			27.04 ± 2.91			0.0038	24.62 ± 5.59			0.0939	0.6775	11.69 ± 2.10			0.0008	<0.0001	<0.0001
CE	**CV**	**CE^2/CV^2**	0.090	0.202	0.200	0.048	0.108	0.200		0.101	0.227	0.200			0.080	0.180	0.200			
MLI [µm]			42.48 ± 4.79			41.23 ± 7.62			0.9856	41.70 ± 11.90			0.997	0.9995	33.86 ± 2.44			0.0866	0.2407	0,2327
CE	**CV**	**CE^2/CV^2**	0.078	0.175	0.200	0.083	0.185	0.200		0.128	0.285	0.200			0.032	0.072	0.200			

Abbreviations: *CE*, coefficient of error; *CV*, coefficient of variation; *h*, hours in medium culture; *P*, Post-natal day; *MLI*, mean linear intercept; *SV*, surface density; τ, arithmetic mean septal thickness; Values are presented as mean ± S.D., standard deviation. *N* = 5 lungs per group. One-way ANOVA with Tukey's *post hoc* analysis was used to determine *P* values

Table S 5. Structural parameters of *in vivo* and *in vitro* 300-µm-thick PCLS in embedded in paraffin.

			P3			P3+72h				P7					P14				
			mean ± S.D.			mean ± S.D.			P3	mean ± S.D.			P3	P3+72h	mean ± S.D.			P3	P3+72h	P7
S_V [cm^{-1}]			630.31 ± 18.78			522.88 ± 76.17			0.0074	713.65 ± 16.40			0.0412	<0.0001	910.94 ± 38.67			<0.0001	<0.0001	<0.0001
CE	**CV**	**CE^2/CV^2**	0.013	0.030	0.200	0.065	0.146	0.200		0.010	0.023	0.200			0.019	0.042	0.200			
τ (sep) [µm]			8.75 ± 0.94			21.71 ± 4.19			<0.0001	8.91 ± 1.39			0.9995	<0.0001	6.416 ± 0.977			0.9998	<0.0001	0.9976
CE	**CV**	**CE^2/CV^2**	0.048	0.107	0.200	0.086	0.193	0.200		0.070	0.156	0.200			0.036	0.081	0.200			
MLI [µm]			46.01 ± 2.06			34.40 ± 4.04			<0.0001	38.26± 1.93			0.0009	0.1172	26.70 ± 1.22			<0.0001	0.001	<0.0001
CE	**CV**	**CE^2/CV^2**	0.020	0.045	0.200	0.052	0.117	0.200		0.023	0.050	0.200			0.020	0.046	0.200			

Abbreviations: *CE*, coefficient of error; *CV*, coefficient of variation; *h*, hours in medium culture; *P*, Post-natal day; *MLI*, mean linear intercept; *SV*, surface density; τ, arithmetic mean septal thickness; Values are presented as mean ± S.D., standard deviation. *N* = 5 lungs per group. One-way ANOVA with Tukey's *post hoc* analysis was used to determine *P* values

Table S 6. Structural parameters of *in vivo* and *in vitro* 1,000-µm-thick PCLS in embedded in paraffin

			P4			P4+96h				P8					P12				
			mean ± S.D.			mean ± S.D.			P4	mean ± S.D.			P4	P4+96h	mean ± S.D.			P4	P4+96h	P8
S_V [cm^{-1}]			645.31 ± 30.62			501.63 ± 57.38			<0.0001	713.11 ± 17.75			0.034	<0.0001	879.44 ± 19.51			<0.0001	<0.0001	<0.0001
CE	**CV**	**CE^2/CV^2**	0.021	0.047	0.200	0.051	0.114	0.200		0.011	0.025	0.200			0.010	0.022	0.200			
τ (sep) [µm]			7.84 ± 1.12			15.15 ± 2.16			<0.0001	8.48 ± 0.99			0.6824	<0.0001	7.73 ± 4.04			0.9994	<0.0001	0.6121
CE	**CV**	**CE^2/CV^2**	0.064	0.143	0.200	0.064	0.142	0.200		0.052	0.116	0.200			0.233	0.522	0.200			
MLI [µm]			46.44 ± 3.59			50.19 ± 7.72			0.5421	39.00 ± 1.23			0.0493	0.0032	30.03 ± 1.64			0.0001	<0.0001	0.0329
CE	**CV**	**CE^2/CV^2**	0.035	0.077	0.200	0.069	0.154	0.200		0.014	0.032	0.200			0.024	0.055	0.200			

Abbreviations: *CE*, coefficient of error; *CV*, coefficient of variation; *h*, hours in medium culture; *P*, Post-natal day; *MLI*, mean linear intercept; *SV*, surface density; τ, arithmetic mean septal thickness; Values are presented as mean ± S.D., standard deviation. *N* = 5 lungs per group. One-way ANOVA with Tukey's *post hoc* analysis was used to determine *P* values

Table S 7. Structural parameters of *in vivo* and *in vitro* 300-µm-thick PCLS in embedded in GMA.

			P3			P3+72h				P7				P14				
			mean ± S.D.			mean ± S.D.			P3	mean ± S.D.			P3	P3+72h	mean ± S.D.			P3	P3+72h	P7
S_V [cm^{-1}]			470.01 ± 19.43			364.53 ± 35.60			0.0018	605.37 ± 39.39			0.0001	<0.0001	851.10 ± 47.71			<0.0001	<0.0001	<0.0001
CE	**CV**	**CE²/CV²**	0.018	0.041	0.200	0.044	0.098	0.200		0.029	0.065	0.200			0.025	0.056	0.200			
τ (sep) [µm]			16.14 ± 0.89			32.16. ± 5.24			<0.0001	11.27 ± 1.43			0.0664	<0.0001	6.49 ± 1.42			0.0003	<0.0001	0.0733
CE	**CV**	**CE²/CV²**	0.025	0.055	0.200	0.073	0.163	0.200		0.057	0.127	0.200			0.098	0.219	0.200			
MLI [µm]			52.94 ± 3.13			46.23 ± 3.59			0.0125	43.78 ± 13.05			0.0009	0.5762	34.14 ± 1.88			<0.0001	<0.0001	0.0005
CE	**CV**	**CE²/CV²**	0.026	0.059	0.200	0.035	0.078	0.200		0.031	0.070	0.200			0.025	0.055	0.200			

Abbreviations: *CE*. coefficient of error; *CV*, coefficient of variation; *GMA*, Glycidyl methacrylate; *h*, hours in medium culture; *P*, Post-natal day; *MLI*, mean linear intercept; *SV*, surface density; τ, arithmetic mean septal thickness; Values are presented as mean ± S.D., standard deviation. *N* = 5 lungs per group. One-way ANOVA with Tukey's *post hoc* analysis was used to determine *P* values

Table S 8. Structural parameters of *in vivo* and *in vitro* 1,000-µm-thick PCLS in embedded in GMA

			P4			P4+96h				P8				P12				
			mean ± S.D.			mean ± S.D.			P4	mean ± S.D.			P4	P4+96h	mean ± S.D.			P4	P4+72h	P8
S_V [cm^{-1}]			491.21 ± 12.89			440.59 ± 29.97			0.017	602.99 ± 26.63			<0.0001	<0.0001	732.57 ± 20.81			<0.0001	<0.0001	<0.0001
CE	**CV**	**CE²/CV²**	0.012	0.026	0.200	0.030	0.068	0.200		0.020	0.044	0.200			0.013	0.028	0.200			
τ (sep) [µm]			13.24 ± 1.11			13.15 ± 1.75			0.878	11.54 ± 1.86			0.5121	0.0026	9.19 ± 3.59			0.1791	0.0006	0.0449
CE	**CV**	**CE²/CV²**	0.038	0.084	0.200	0.056	0.125	0.200		0.072	0.161	0.200			0.175	0.391	0.200			
MLI [µm]			54.99 ± 1.81			63.27 ± 73.47			0.0005	42.32 ± 2.19			<0.0001	<0.0001	36.27 ± 2.05			<0.0001	<0.0001	0.0054
CE	**CV**	**CE²/CV²**	0.015	0.033	0.200	0.025	0.055	0.200		0.023	0.052	0.200			0.025	0.057	0,200			

Abbreviations: *CE*. coefficient of error; *CV*, coefficient of variation; *GMA*, Glycidyl methacrylate; *h*, hours in medium culture; *P*, Post-natal day; *MLI*, mean linear intercept; *SV*, surface density; τ, arithmetic mean septal thickness; Values are presented as mean ± S.D., standard deviation. *N* = 5 lungs per group. One-way ANOVA with Tukey's *post hoc* analysis was used to determine *P* values

Table S 9. Compared structural parameters between 300- µm- and 1,000-µm-thick *in vitro* PCLS in embedded in paraffin.

			P3+72h			P4+96h			
			mean ± S.D.			mean ± S.D.			P3+72h
	S_V [cm^{-1}]			522.88 ± 76.17			501.63 ± 57.38		0.6317
CE	**CV**	**CE²/CV²**	0.065	0.146	0.200	0.051	0.114	0.200	
	τ (sep) [µm]			21.71 ± 4.19			15.15 ± 2.16		0.0145
CE	**CV**	**CE²/CV²**	0.086	0.193	0.200	0.064	0.142	0.200	
	MLI [µm]			34.40 ± 4.04			50.19 ± 7.72		0.0037
CE	**CV**	**CE²/CV²**	0.052	0.117	0.200	0.069	0.154	0.200	

Abbreviations: *CE*, coefficient of error; *CV*, coefficient of variation; *h*, hours in medium culture; *P*, Post-natal day; *MLI*, mean linear intercept; *SV*, surface density; τ, arithmetic mean septal thickness; Values are presented as mean ± S.D., standard deviation. *N* = 5 lungs per group. Students' t-test analysis was used to determine *P* values

Table S 10. Compared structural parameters between 300- µm- and 1,000-µm-thick *in vitro* PCLS in embedded in GMA

			P3+72h			P4+96h			
			mean ± S.D.			mean ± S.D.			P3+72h
	S_V [cm^{-1}]			364.53 ± 35.60			440.59 ± 29.97		0.0064
CE	**CV**	**CE²/CV²**	0.044	0.098	0.200	0.030	0.068	0.200	
	τ (sep) [µm]			32.16. ± 5.24			13.15 ± 1.75		<0.0001
CE	**CV**	**CE²/CV²**	0.073	0.163	0.200	0.056	0.125	0.200	
	MLI [µm]			46.23 ± 3.59			50.19 ± 7.72		<0.0001
CE	**CV**	**CE²/CV²**	0.035	0.078	0.200	0.025	0.055	0.200	

Abbreviations: *CE*, coefficient of error; *CV*, coefficient of variation; *GMA*, Glycidyl methacrylate; *h*, hours in medium culture; *P*, Post-natal day; *MLI*, mean linear intercept; *SV*, surface density; τ, arithmetic mean septal thickness; Values are presented as mean ± S.D., standard deviation. *N* = 5 lungs per group. Students' t-test analysis was used to determine *P* values

Table S 11. Compared structural parameters between GMA- and paraffin-embedded *in vivo* and *in vitro* PCLS.

	S_V [cm^{-1}]			τ (sep) [µm]			MLI [µm]		
	Paraffin	GMA	*P* value	Paraffin	GMA	*P* value	Paraffin	GMA	*P* value
	mean ± S.D.	mean ± S.D.		mean ± S.D.	mean ± S.D.		mean ± S.D.	mean ± S.D.	
P3	630.31 ± 18.78	470.01 ± 19.43	<0.0001	8.75 ± 0.94	16.14 ± 0.89	<0.0001	46.01 ± 2.06	52.94 ± 3.13	0.0084
P3+72h	522.88 ± 76.17	364.53 ± 35.60	<0.0001	21.71 ± 4.19	32.16. ± 5.24	<0.0001	34.40 ± 4.04	46.23 ± 3.59	<0.0001
P4	645.31 ± 30.62	491.21 ± 12.89	<0.0001	7.84 ± 1.12	13.24 ± 1.11	0.0009	46.44 ± 3.59	54.99 ± 1.81	0.0006
P4+96h	501.63 ± 57.38	440.59 ± 29.97	0.0697	15.15 ± 2.16	13.15 ± 1.75	>0.9999	50.19 ± 7.72	63.27 ± 73.47	<0.0001
P7	713.65 ± 16.40	605.37 ± 39.39	<0.0001	8.91 ± 1.39	11.27 ± 1.43	0.6243	38.26± 1.93	43.78 ± 13.05	0.0623
P8	713.11 ± 17.75	602.99 ± 26.63	<0.0001	8.48 ± 0.99	11.54 ± 1.86	0.1662	39.00 ± 1.23	42.32 ± 2.19	0.3237
P12	879.44 ± 19.51	732.57 ± 20.81	<0.0001	7.73 ± 4.04	9.19 ± 3.59	>0.9999	30.03 ± 1.64	36.27 ± 2.05	0.0234
P14	910.94 ± 38.67	851.10 ± 47.71	0.0799	6.416 ± 0.977	6.49 ± 1.42	0.861	26.70 ± 1.22	34.14 ± 1.88	0.0037

Abbreviations: *CE.* coefficient of error; *CV*, coefficient of variation; *GMA*, Glycidyl methacrylate; *h*, hours in medium culture; *P*, Post-natal day; *MLI*, mean linear intercept; *SV*, surface density; τ, arithmetic mean septal thickness; Values are presented as mean ± S.D., standard deviation. *N* = 5 lungs per group. Students' t-test analysis was used to determine *P* values.

Table S 12. Compared values for measured mesenchymal, epithelial and proliferation gene expressed markers in PCL

	PDGFRα	**ACTA2**	**COL1A1**	**VIM**	**PDPN**	**STFPC**	**MKI67**
P3 vs. P3+72h	<0.0001	0.1314	<0.0001	0.8727	0.0275	<0.0001	0.9898
P3 vs. P7	<0.0001	0.8475	0.4328	0.0271	0.0114	<0.0001	0.5148
P3 vs. P14	<0.0001	0.7279	0.9958	0.0032	0.9448	<0.0001	0.7141
P3+72h vs. P7	<0.0001	0.381	<0.0001	0.078	0.0002	<0.0001	0.3675
P3+72h vs. P14	0.0002	0.0302	<0.0001	0.008	0.0131	<0.0001	0.5467
P7 vs. P14	0.2402	0.3156	0.5477	0.3976	0.0237	0.1401	0.9829

N = 5 lungs per group. Students' t-test analysis was used to determine *P* values.

15. Declaration

I declare that I have completed this dissertation single-handedly without the unauthorized help of a second party and only with the assistance acknowledged therein. I have appropriately acknowledged and referenced all text passages that are derived literally from or are based on the content of published or unpublished work of others, and all information that relates to verbal communications. I have abided by the principles of good scientific conduct laid down in the charter of the Justus Liebig University of Giessen in carrying out the investigations described in the dissertation.

Giessen, 7th of October 2022

David Pérez Bravo

16. Acknowledgement

Hereby I would to thank several persons without whom, this project would have never been achievable. In 2016, when I decided to come to Germany in order to continue my scientific career, I never thought that I would be that lucky by sharing my doctoral experiences with such extraordinary scientists.

First, and foremost, I would like to thank Prof. Dr. Wegner Seeger, for the opportunity to be part of this outstanding project and to attend to the international graduate program Molecular Biology and Medicine of the Lung (MBML). To the Max Planck Institute in Bad Nauheim to offer me the opportunity to work with inspiring, and amazing young scientists. Secondly, my direct supervisor, Dr. Katrin Ahlbrecht, for the passionate dedication invested towards the completion of this work.

A further thanks goes to Prof. Dr. Rory Morty, his enthusiastic and extremely professional help in designing and executing the experiments with the PCLS, from lab inception all the way to statistical analysis and writing.

To all my lab mates, whose daily support has made this journey extremely pleasant. Without them, countless studying hours and laboratory work would have been terribly lonely. I am confident that our friendship will continue in our future scientific career. Ettore Lignelli for your curiosity and insights into science-fiction and scientific work, passions that sharing with you made me feel home. Misa Gunjak, for hours exchanging with me lab-troubleshooting tips while casually going over to plant/cat-loving conversations. Despoina Mitty, to be there for me at any situation and being part of our Pérez-Carrau family. Francisco Casado, from Murcia to Bad Nauheim, our paths are so randomly connected that I am sure that we will work together again. Dr. Alberto Rodríguez and Dr. Ivonne Vázquez for your kindness and lovely friendship. Dr. Claudio Nardiello and Claudia García, for all your support during the PhD, lovely dinner nights and stimulating conversations. Solmaz Khaghani for all your help sharing experiments and calculations. Franchesco Palumbo for share your knowledge of the stimulating world of antibodies and Reshma Jamal for show us that it is possible to do a PhD during holidays.

I would not like to forget my first professional mentors, Prof. Dr. Guillermo Ramis and Dr. Laura Martínez. For all your trust in me, thank you.

To my family. For having contributed to making me who I am today, all their trust and passion grew in the fertile land of the support and understanding. I miss you very much and hope we can be together soon. And to my second family, the wonderful Carrau Garreta family.

For her support when I most needed it, I want to deeply and truly my wife, for her endless supply of patience, faith in me and for his emotional support even in my darkest hour.

Der Lebenslauf wurde aus der elektronischen Version der Arbeit entfernt.

The curriculum vitae was removed from the electronic version of the paper.